PREDICTION OF TURBULENCE STATISTICS IN A MODEL DUMP COMBUSTOR USING ARTIFICAL NEURAL NETWORKS

A THESIS IN MECHANICAL ENGINEERING

Master of Science in Mechanical Engineering (MSME)

Presented to the faculty of the American University of Sharjah
College of Engineering in partial fulfillment of
the requirements for the degree

MASTER OF SCIENCE

By
AMIN MOH'D ALSHARIF
B.S. 2008

Sharjah, UAE
May 2011

We approve the thesis of Amin Moh'd AlSharif | Date of signature

_____ _____

Dr. Saad Ahmed
Professor, Department of Mechanical Engineering
Thesis Advisor

_____ _____

Dr. Hany El Kadi
Associate Professor, Department of Mechanical Engineering
Thesis Co-Advisor

_____ _____

Dr. Ghassan Qadah
Associate Professor, Department of Computer Science & Engineering
Graduate Committee

_____ _____

Dr. Mamoun Abdel-Hafez
Assistant Professor, Department of Mechanical Engineering
Graduate Committee

_____ _____

Dr. Mohammad Ameen Al-Jarrah
Department Head,
Department of Mechanical Engineering

_____ _____

Dr. Hany El Kadi
Associate Dean,
College of Engineering

_____ _____

Dr. Yousef Al-Assaf
Dean,
College of Engineering

_____ _____

Dr. Gautam Sen
Vice-Provost, Research & Graduate Studies

PREDICTION OF TURBULENCE STATISTICS IN A MODEL DUMP COMBUSTOR

USING ARTIFICIAL NEURAL NETWORKS

Amin Moh'd AlSharif, Candidate for the Master of Science in Mechanical Engineering

American University of Sharjah, 2011

ABSTRACT

The flowfield characteristics downstream of an axisymmetric sudden-expansion dump combustor model are important to designers of gas turbines and liquid-fuel ramjets ducted rockets. Many experimental techniques such as Laser Doppler Velocimetry (LDV) measurements provide only limited discrete information at given points; especially, for the cases of complex flows such as swirling flows of a dump combustor. For these types of flows, usual numerical interpolating schemes appear to be unsuitable. Artificial Neural Networks (ANN) methods are thus proposed as an alternative and the flow predictions obtained are tested and presented in this thesis.

To predict the velocity components and the turbulence statistics obtained experimentally under a variety of swirl numbers, the use of a variety of ANN architectures is investigated. In each case, the predictions obtained are compared with published experimental data to determine the ANN structure that predicts the flow parameters most accurately. Moreover, the generated data is used to provide contour and surface plots to show the detailed flow characteristics throughout the model.

The examined turbulence statistics are fluid flow velocity components in axial, radial, and tangential directions, in addition to Reynolds shear and normal stresses. Also triple velocity correlations are scrutinized.

The investigation of ANN architecture variation shows that generalized feedforward network (GFF) with one hidden layer is the most efficient network, in which most turbulence statistics are predicted accurately. Moreover, the study shows that GFF network performs better when its built architecture uses Levenberg-Marquardt learning rule and Tanhaxon transfer function for weights update.

The obtained results look promising, thus, ANN is utilized to enhance the understanding of the behavior of swirling, recalculating, axisymmetric, and turbulent flow inside dump combustors. ANN is employed to compute kinetic energy terms (production, diffusion, convection, and viscous dissipation as well as estimating stream function to recognize the recirculation regions at combustor's corners and centerline.

KEYWORDS

Swirl flow, dump combustor, artificial neural network, fuzzy logic and radial basis function.

CONTENTS

ABSTRACT iii

KEYWORDS iv

CONTENTS v

LIST OF ILLUSTRATOINS vii

LIST OF TABLES xii

ACKNOWLEDGEMENTS xiii

NOMENCLATURE xv

1 INTRODUCTION 1

1.1 Review of Literature 2

1.1.1 Historical Background 2

1.1.2 Recent Development in the Primary Field under Study 4

1.2 Methodology and Objectives 9

2 FLUID FLOW CHARACTETRISTICS 11

3 EXPERIMENTAL SETUP 14

4 ARTIFICIAL NEURAL NETWORKS 17

4.1 Training and Testing 21

4.2 Neural Network Configuration 21

4.3 Neural Network Selection 23

4.3.1 Selection of Learning Rule 23

4.3.2 Selection of Transfer Function 24

4.3.3 Generalized Feedforward Network Configuration 25

4.3.4 Radial Basis Function Network Configuration 27

4.3.5 CANFIS Network Configuration 32

5 RECONSTRUCTION AND PRODUCTION OF TURBULENCE STATISTICS 44

6 CALCULATION OF STREAM FUNCTION AND TKE EQUATION 92
6.1 Stream Function 92
6.2 Turbulent Kinetic Energy Equation 96
7 PREDICTION OF DATA FOR A DIFFERENT SWIRL NUMBER 106
8 CONCLUSIONS AND RECOMMENDATIONS 114
8.1 Conclusions 114
8.2 Recommendations 115
REFERENCE LIST 116
A. APPENDIX A: ARTIFICIAL NEURAL NETWORKS 122
B. APPENDIX B: ADDITIONAL RESULTS USING ANN 130
VITA 133

LIST OF ILLUSTRATOINS

Figure 3.1 Schematic of the experimental setup (A) Dump combustor model (B) Section A-A (C) Assembly for measurement in the horizontal $U-V$ plane (D) Assembly for measurement in the vertical $(U-W)$ plane....15

Figure 4.1 Multilayered neural network....19

Figure 4.2 Average CC of testing U at x/H=3, 6, 10 for 0.5 swirler as a function of learning rule....24

Figure 4.3 Average CC of testing U at x/H=3, 6, 10 for 0.5 swirlers as a function of transfer function....25

Figure 4.4 Average CC of testing $U, V,$ and W at x/H=3, 6, 10 for 0.5 swirlers as a function of number of neurons....27

Figure 4.5 RBF network [42]....28

Figure 4.6 Average CC of testing U at x/H=3, 6, 10 for 0.5 swirlers as a function of competitive rule and cluster size....31

Figure 4.7 Average CC of testing U at x/H=3, 6, 10 for 0.5 swirlers as a function of metric type and cluster size....32

Figure 4.8 CANFIS network structure [37]....34

Figure 4.9 Average CC of testing W at x/H=3, 6, 10 for 0.5 swirlers as a function of membership function and number of membership functions....37

Figure 4.10 Average CC of testing GFF network for U, W, u'_{RMS}, and w'_{RMS} at x/H=3, 6, 10 as a function of number of neurons....38

Figure 4.11 Average CC of testing Bell CANFIS network for U, W, u'_{RMS}, and w'_{RMS} at x/H=3, 6, 10 as a function of number of membership functions....38

Figure 4.12 Average CC of testing Gaussian CANFIS network for U, W, u'_{RMS}, and w'_{RMS} at x/H=3, 6, 10 as a function of number of membership functions....39

Figure 4.13 Average CC of testing RBF network forU, W, u'_{RMS}, and w'_{RMS} at x/H=3, 6, 10 as a function of number of cluster size....40

Figure 4.14 Average CC of testing GFF network for $V, v'_{RMS}, \overline{u'v'}$, and $\overline{u'w'}$ at x/H=3, 6, 10 as a function of number of neurons....41

Figure 4.15 Average CC of testing Bell CANFIS network for $V, v'_{RMS}, \overline{u'v'}$, and $\overline{u'w'}$ at x/H=3, 6, 10 as a function of number of membership functions....41

Figure 4.16 Average CC of testing Gaussian CANFIS network for $V, v'_{RMS}, \overline{u'v'}$, and $\overline{u'w'}$ at x/H=3, 6, 10 as a function of number of membership functions 42
Figure 4.17 Average CC of testing RBF network for $V, v'_{RMS}, \overline{u'v'}$, and $\overline{u'w'}$ at x/H=3, 6, 10 as a function of number of cluster size 43
Figure 5.1 Evolution of U/U_o profiles at x/H=1, 3, 5, and 8 for experimental and neural networks predictions 45
Figure 5.2 Evolution of W/U_o at x/H=1, 3, 5, and 8 profiles for experimental and neural networks predictions 45
Figure 5.3 Evolution of u'_{RMS}/U_o profiles for experimental and neural networks predictions.....46
Figure 5.4 Evolution of w'_{RMS}/U_o profiles for experimental and neural networks predictions.....46
Figure 5.5 Evolution of U/U_o at 0.5 swirler, Zeros indicate the origin for each profile, and the Scale is given by number at the end right. (a)Experimental (b)ANN 49
Figure 5.6 Evolution of W/U_o at 0.5 swirler, Zeros indicate the origin for each profile, and the Scale is given by number at the end right. (a)Experimental (b)ANN 51
Figure 5.7 Evolution of V/U_o at 0.5 swirler, Zeros indicate the origin for each profile, and the Scale is given by number at the end right. (a)Experimental (b)ANN 52
Figure 5.8 Evolution of u'_{RMS}/U_o at 0.5 swirler, Zeros indicate the origin for each profile, and the Scale is given by number at the end right. (a)Experimental (b)ANN 53
Figure 5.9 Evolution of w'_{RMS}/U_o at 0.5 swirler, Zeros indicate the origin for each profile, and the Scale is given by number at the end right. (a)Experimental (b)ANN 54
Figure 5.10 Evolution of v'_{RMS}/U_o at 0.5 swirler, Zeros indicate the origin for each profile, and the Scale is given by number at the end right. (a)Experimental (b)ANN 55
Figure 5.11 Evolution of $\overline{u'v'}/\mathrm{U}_o^2$ at 0.5 swirler, Zeros indicate the origin for each profile, and the Scale is given by number at the end right. (a)Experimental (b)ANN 56
Figure 5.12 Evolution of $\overline{u'w'}/\mathrm{U}_o^2$ at 0.5 swirler, Zeros indicate the origin for each profile, and the Scale is given by number at the end right. (a)Experimental (b)ANN 57
Figure 5.13 Evolution of $\overline{u'^3}/\mathrm{U}_o^3$ at 0.5 swirler, Zeros indicate the origin for each profile, and the Scale is given by number at the end right. (a)Experimental (b)ANN 58

Figure 5.14 Evolution of $\overline{v'^3}/U_o^3$ at 0.5 swirler, Zeros indicate the origin for each profile, and the Scale is given by number at the end right. (a)Experimental (b)ANN 59
Figure 5.15 Evolution of $\overline{w'^3}/U_o^3$ at 0.5 swirler, Zeros indicate the origin for each profile, and the Scale is given by number at the end right. (a)Experimental (b)ANN 60
Figure 5.16 Evolution of $\overline{u'^2v'}/U_o^3$ at 0.5 swirler, Zeros indicate the origin for each profile, and the Scale is given by number at the end right. (a)Experimental (b)ANN 61
Figure 5.17 Evolution of $\overline{u'v'^2}/U_o^3$ at 0.5 swirler, Zeros indicate the origin for each profile, and the Scale is given by number at the end right. (a)Experimental (b)ANN 62
Figure 5.18 Evolution of $\overline{u'^2w'}/U_o^3$ at 0.5 swirler, Zeros indicate the origin for each profile, and the Scale is given by number at the end right. (a)Experimental (b)ANN 63
Figure 5.19 Evolution of $\overline{u'w'^2}/U_o^3$ at 0.5 swirler, Zeros indicate the origin for each profile, and the Scale is given by number at the end right. (a)Experimental (b)ANN 64
Figure 5.20 Experimental U/U_o distribution.....66
Figure 5.21 ANN U/U_o distribution.....66
Figure 5.22 Experimental V/U_odistribution 68
Figure 5.23 ANN V/U_o distribution.....68
Figure 5.24 Experimental W/U_odistribution.....70
Figure 5.25 ANN W/U_o distribution.....70
Figure 5.26 Experimental ${u'}_{RMS}/U_o$distribution 72
Figure 5.27 ANN ${u'}_{RMS}/U_o$distribution 72
Figure 5.28 Experimental ${v'}_{RMS}/U_o$ distribution 74
Figure 5.29 ANN ${v'}_{RMS}/U_o$ distribution 74
Figure 5.30 Experimental ${w'}_{RMS}/U_o$ distribution 76
Figure 5.31 ANN ${w'}_{RMS}/U_o$ distribution 76
Figure 5.32 Experimental $100\overline{u'v'}/U_o^2$ distribution 78
Figure 5.33 ANN $100\overline{u'v'}/U_o^2$ distribution 78
Figure 5.34 Experimental $100u'w'/U_o^2$ distribution.....80
Figure 5.35 ANN $100\overline{u'w'}/U_o^2$ distribution.....80
Figure 5.36 Experimental $100\overline{u'^3}/U_o^3$ distribution.....82
Figure 5.37 ANN $100\overline{u'^3}/U_o^3$ distribution.....82

Figure 5.38 Experimental $100\overline{v'^3}/\mathrm{U}_o^3$ distribution 84
Figure 5.39 ANN $100\overline{v'^3}/\mathrm{U}_o^3$ distribution 84
Figure 5.40 Experimental $100\overline{w'^3}/\mathrm{U}_o^3$ distribution 86
Figure 5.41 ANN $100\overline{w'^3}/\mathrm{U}_o^3$ distribution 86
Figure 5.42 Experimental $100\overline{u'^2\mathrm{v}'}/\mathrm{U}_o^3$ distribution 88
Figure 5.43 ANN $100\overline{u'^2\mathrm{v}'}/\mathrm{U}_o^3$ distribution 88
Figure 5.44 Experimental $100\overline{\mathrm{u}'v'^2}/\mathrm{U}_o^3$distribution 90
Figure 5.45 ANN $100\overline{\mathrm{u}'v'^2}/\mathrm{U}_o^3$ distribution 90
Figure 6.1 Non-dimensional stream function contours at Sn =0 (a) Experimental (b) ANN 93
Figure 6.2 Non-dimensional stream function contours at Sn =0.3 (a) Experimental (b) ANN 94
Figure 6.3 Non-dimensional stream function contours at Sn =0.4 (a) Experimental (b) ANN 95
Figure 6.4 Non-dimensional stream function contours at Sn =0.5 (a) Experimental (b) ANN 96
Figure 6.5 Experimental distribution of normalized production term of turbulent kinetic energy 99
Figure 6.6 ANN distribution of normalized production term of turbulent kinetic energy 99
Figure 6.7 Experimental distribution of normalized convection term of turbulent kinetic energy 101
Figure 6.8 ANN distribution of normalized convection term of turbulent kinetic energy 101
Figure 6.9 Experimental distribution of normalized diffusion term of turbulent kinetic energy 103
Figure 6.10 ANN distribution of normalized diffusion term of turbulent kinetic energy 103
Figure 6.11 Experimental distribution of normalized viscous dissipation term of turbulent kinetic energy 105
Figure 6.12 ANN distribution of normalized viscous dissipation term of turbulent kinetic energy 105
Figure 7.1 Distribution of U/U_o at 0.35 swirler 107

Figure 7.2 Distribution of V/U_o at 0.35 swirler 108
Figure 7.3 Distribution of W/U_o at 0.35 swirler 109
Figure 7.4 Distribution of u'_{RMS}/U_o at 0.35 swirler 110
Figure 7.5 Distribution of v'_{RMS}/U_o at 0.35 swirler.....111
Figure 7.6 Distribution of w'_{RMS}/U_o at 0.35 swirler.....112

LIST OF TABLES

Table 1.1 Overview of previous studies in axisymmetric sudden expansion flows and ANN 7

Table 5.1 Best network and CC values of turbulence statistics at x/H=6 for 0.5 swirler ..47

Table 7.1 NMSE and CC values of testing 0.4 swirler for each component 106

ACKNOWLEDGEMENTS

In the name of Allah, most Gracious, most Merciful.

First of all, all praise and glory be to Allah, the Almighty, for enlightening my way and directing me to accomplish this small objective successfully, and our beloved prophet Mohammad –Sallah Allah Alaihi w Sallam- the perfect example to be followed, all my wishes and prays go towards meeting you in paradise enshalla.

I would like to express my sincere gratitude and deep appreciation to my advisor Dr. Saad Ahmed, my co-advisor Dr. Hany El Kadi and my committee members Dr. Mamoun Abdel-Hafez and Dr. Ghassan Qadah, for the invaluable guidance, patience, and encouragement and valuable countless hours of attention they dedicated throughout this work. They provided me with important suggestions, significant ideas, and helpful materials to develop this thesis. May Allah reward them in this world and the hereafter.

To my favorite professor, Dr. Mohammad Al-Nimr, I hope you are proud of me as much as I am proud, thankful, and respectful to you, special applause to him for his continuous support and guidance, thanks a lot.

I will not also forget Dr. Khaled Assaleh for his efforts in guiding me in places where I get stuck; I wish him all the best in his life.

Special thanks go to all faculty members of the Department of Mechanical Engineering in the American University of Sharjah for their valuable advice and guidance.

My deepest gratitude goes to my family for their unlimited encouragement, endless support, and continuous love and prayers. I owe my parents, brothers and sister everything that I have learned or earned in my life. I know I can never come close to returning their favor upon me. May Allah reward them in this world and the hereafter.

To my favorite person in this living world, my lovely sweet wife, I do not have enough words to thank her for everything, especially her time, warm

feelings, continuous support, and everything she provided me with. May Allah let us meet in heaven enshalla.

I will always be thankful to my friends and colleagues for their unlimited support. Many friends have helped me along the way by listening, offering advice and ideas. Special thanks go to my best friend, Jamil Fayyad for supporting me during my ups and downs throughout this research. I would like also to thank my friends, Mohammad Jaghoub, Ahmed Abu Hatab, Mohammad Suleiman, Ahmed Al-Nabulsi, and Qasem Hassan for supporting me whenever I doubted myself. All efforts that have been made to keep my life in the university as an enjoyable and friendly place to work in, are appreciated and will be a memorable experience.

NOMENCLATURE

ANN: Artificial neural network

CC: Correlation coefficient

CFD: Computational fluid dynamics

CG: Conjugate gradient learning rule

GFF: Generalized feedforward

G_θ: Angular momentum

G_x: Axial momentum

H: Step height

L: Traveled length of the fluid or fluid hydraulic radius

LDV: Laser doppler velocimetry

LM: Levenberg-Marquardt learning rule

MLP: Multi layer perceptron

MSE: Mean squared error

$NMSE$: Normalized mean squared error

p: Pressure denoted by the fluid

p_∞: Ambient Pressure

PE: Processing element

PIV: Particle image velocimetry

PVC: Precessing vortex core

o: Output of neuron

RBF: Radial basis function

Re: Reynolds number

S_n: Swirl number

TKE: Turbulent kinetic energy

$u'_{RMS}, v'_{RMS}, w'_{RMS}$: RMS of velocity fluctuations in $x, r,$ and θ directions, respectively

$\overline{\rho u'^2}, \overline{\rho v'^2}, \overline{\rho w'^2}$: Reynolds normal stresses

$\overline{\rho u'v'}, \overline{\rho u'w'}, \overline{\rho v'w'}$: Reynolds shear stresses

U, V, W: Velocity components in $x, r,$ and θ directions, respectively

w: Weight between neurons (interconnections)

x, r, θ: Axial, radial, and azimuthal coordinates, respectively

Greek Letters:

α: Momentum of first or second order learning rule

η: Learning rate

μ: Dynamic viscosity of the fluid

ρ: Fluid density

Ψ: Normalized stream function

Subscripts:

i, j: i^{th} and j^{th} element

c: Combustor

CHAPTER 1

INTRODUCTION

Swirl is a three-dimensional phenomenon in fluid flow where some of the particles follow a spiraling trajectory around the longitudinal axis of the vessel (mostly combustors) as they move along in the flow. Combustion systems that operate based on the principles of swirling fluid motion to facilitate the combustion process have increasingly been in extensive use.

In view of the fact that many practical combustion processes involve swirl, many studies devoted attention to mixing and combustion phenomena encountered in swirl flows. Swirl flow fills this gap and is a valuable occupation for combustion scientists and engineers. This thesis provides a general description of swirl flow phenomena. However, swirl flow is particularly relevant to the field of combustion. There are several applications where swirl is employed, such as swirlstabilized combustion, cyclone combustion chambers, hazardous-waste incinerators, tangentially fired furnaces, gas turbine combustors, gasoline engines, diesel engines, and fire whirl. Moreover, several devices exploit swirl where combustion process is not involved, such as cyclone separators, and Hilsch tubes **[**1**]**. Swirl flows are also now utilized in modern combustion machinery such as refinery or power station burners.

In this study, the main apprehension is to improve combustor performance by investigating the fluid flow characteristics inside the chamber. The motion of fluid substances inside the combustor is very complicated, since it is subjected to turbulent flow laws. From there, many models have been proposed to illustrate this motion. One of the most famous models is the Navier-Stokes equations, which arise from applying Newton's second law to fluid motion, where the fluid stress is the sum of a diffusing viscous term in addition to pressure term **[**2**]**.

1.1 Review of Literature

1.1.1 Historical Background

Dellenback et al. and Hallett and Günther **[**3**,**4**]**, respectively, are probably the most complete and most widely referenced experimental studies of turbulent swirling flows in a sudden expansion. Dellenback used laser Doppler anemometry (LDA) to characterize the turbulent swirling flow in a 1:1.94 sudden expansion for a range of swirl intensities. Precession frequency data were combined with flow visualization in order to identify various flow regimes in relation to PVC and vortex breakdown. Within the range of swirl numbers they experimented with, they distinguished between seven flow regimes: for Re=30000 and low swirl numbers (S_n<0.18) the vortex precession took place in a direction opposite to the mean swirl, at S_n=0.18 the precession frequency became zero, for 0.18<S_n<0.37 the vortex precessed in the same direction as the mean swirl and at S_n=0.37 the PVC vanishes. Above this swirl number, the bubble-type vortex breakdown appeared which for S_n =0.50 underwent a transition from a recirculating bubble to a strong on-axis recirculation. The S ranges were Re dependent. The non-dimensional precessing frequency (Strouhal number) was found to follow similar trends in relation to swirl and Re as those found in other geometries and to be independent of Re for Re>10^5. The experimental data of Dellenback also showed that the reattachment length depends significantly on the swirl number. As the swirl number increased, the reattachment length became shorter. Hallett and Günther also reported flow precession in swirl numbers below the critical one for onset of vortex breakdown, unlike previous studies which associated flow asymmetries with vortex breakdown.

However, a recent study in a model vortex combustor done by Fernandes et al. **[**5**]** showed that the precession regime is a result of a vortex breakdown effect and its frequency evolution with swirl follows a parabolic shape with a minimum Strouhal value of about 0.55–0.6 at S_n=0.88. This trend is similar to

that reported by Dellenback for much lower swirl numbers, well below the critical one for onset of vortex breakdown.

The structure of swirling flows, and in particular the onset of vortex breakdown, is very sensitive to the way the swirl is introduced, i.e., the inlet conditions. The effects of inlet or initial swirl profile and expansion angle on the characteristics of the swirling flow were investigated by Ahmed and Nejad, Chowdhury and Mayeed, and Hallet and Toews **[**6**,**7**]** and **[**8**]**, respectively. Hallet and Toews showed that a lower velocity near the axis or a reduced radius of the solid body vortex core in the inlet will reduce the critical number required for central recirculation. An increase in the expansion ratio up to 1.5 will also reduce the critical swirl number. For expansion ratios greater than 1.5, either a reduction or an increase of the critical swirl number is reported, depending on inlet conditions. Ahmed and Nejad introduced swirl by three different types of swirlers: free vortex, forced vortex and constant angle, respectively. They showed that there are significant differences in the flow field and turbulence characteristics when a different swirler is employed. In their study, for the same swirl number, a central recirculation was only observed in the case of free vortex type of swirling flow after the expansion. However, the centerline turbulence levels were the greatest for constant-angle swirling flow due to the large motion of the vortex centre precession.

Downstream conditions can also influence the development of swirling flows particularly for swirl numbers above the critical, i.e., after the onset of vortex breakdown. Vortex breakdown marks the transition of a swirling flow from a supercritical to a subcritical flow state and this happens roughly when the maximum swirl velocity exceeds the bulk axial velocity. In a subcritical flow, inertial disturbances propagate upstream from far downstream whereas in a supercritical one they are swept away **[**9**,**10**]**. Escudier et al. **[**10**]** studied systematically the influence of outlet conditions on turbulent swirling flow downstream of an orifice by experimenting with five different outlet geometries

(fully open, concentric central contraction, concentric annular contraction, eccentric contraction and fully open double elbow). Their results showed profound effects of outlet geometry throughout the flow field for a high 'subcritical' swirl (S_n=0.6) but negligible. As shown, it is not straight forward to calculate the swirl number, since calculating both momentums need to ensure the velocities and their derivatives along the cross sectional area in infinitesimal element manner, which means huge amount of data is required to attain an accurate swirl number, since those values are changing nonlinearly with high differences.

1.1.2 Recent Development in the Primary Field under Study

Previously, many studies in this field concerned on using computational fluid dynamics (CFD), Large Eddy Simulations (LES) and nonlinear equations such as Navier-Stokes equation to describe the motion of fluid substances.

Computations of flow past a circular cylinder have also been performed to evaluate the numerical as well as physical modeling aspects. Breuer **[**11**]** was among the first to perform LES calculations of flow past a circular cylinder at Re=1.4X10^5. This study focused on the performance of the subgrid scale closures: dynamic and constant Smagorinsky subgrid scale models were employed. This study also examined the effects of grid resolution and spanwise extent of the calculation domain (1D−πD). Breuer concluded that the dynamic subgrid model gave the best results but was not decisively better than the constant Smagorinsky model for this flow. Surprisingly, grid refinement did not automatically lead to improvements in the accuracy of the results. Breuer concluded that in LES because the cut-off length-scale is dependent on the grid resolution, it is still a critical issue to distinguish between numerical effects and physical effects on a given grid.

Lakshmipathy and Girimaji **[**12**]** evaluated the capability of the partially averaged Navier– Stokes (PANS) method in a moderately high Reynolds number (Re= 1.4 X 10^5) turbulent flow past a circular cylinder. The reason

behind using PANS is to simplify Navier-Stokes equation that contains several nonlinear terms. The purported PANS capability of reducing the closure cut-off length-scale by decreasing the f_k value is examined by performing simulations with f_k values of 1.0, 0.7, 0.6, and 0.5. Simulations of the system were attained at different resolutions. Lakshmipathy concluded that when the f_k value is reduced, the unresolved kinetic energy progressively decreases and also the unresolved eddy viscosity leading to more realistic and accurate depiction of flow physics. By decreasing the f_k value, more and more unsteady and three-dimensional scales of motion are captured, as indicated in the instantaneous vorticity contour plots. The vorticity structures get sharper and more complex, yielding an improved characterization of the complex wake structure.

Spentzos et al. [13] used CFD and ANN to simulate three-dimensional Dynamic stall. CFD was used to generate more data and add it to the available experimental data, while ANN was used to training and prediction, they used ANN because CFD computations were too slow comparing to the time needed by ANN to get the same results.

ANN technique was developed after the introduction of simplified neurons by Mcclouch and Pitss [14]. Many models in many fields were done and simulated using ANN architecture. In the last decade, especially with the huge computer technology improvement, a tendency in simulating and generating data using computers were achieved in fluid mechanics and aerodynamics fields using CFD. Turbulent flow has to be modeled and experimental data are needed for these models. ANN is similar to this but totally based on experimental data. Recently, several researchers showed the success of applying ANN as a simulation tool for several applications in thermofluids.

Panigrahi et al. [15] showed the results can be obtained by applying ANN and fuzzy logic to predict turbulence statistics behind a square cylinder. For ANN, the number of nodes in each layer, the initial assignment of weights and biases, the learning rate, and the momentum factor were decided on the

basis of numerical experimentation. For v_{RMS} and u_{RMS}, 2-5-1 configuration was used, while v_{RMS} and $\overline{u'v'}$ were analyzed with 2-8-6-1. For fuzzy model, the membership function was observed to influence the correlation coefficient depending on the type of turbulent statistics being modeled. The largest correlation coefficient was obtained by using 12 membership functions. 50 % of the data were used for training and the rest for testing. However, the architecture of ANN and fuzzy models were not mentioned. Moreover, the obtained predictions were accurate and both methods can be used to simulate such a system, and ended with a conclusion that fuzzy logic model is more efficient.

Pruvsot et al. **[**16**]** showed that radial basis function algorithm can be used successfully to interpolate a three-dimensional swirl flow that creates a spatial dependent velocity-field, even the flow is nonlinear. They used radial basis function as ANN model for generating more data, since discrete data is only available and was obtained using PIV technique. The inputs of the network were $x, r,$ and ξ, which are the axial, radial, and circumferential positions with respect to the tangential inlet axis. The obtained outputs from the network were velocity components and turbulent inteinsities in the axial, radial, and circumferential directions. They also showed how error can be affected by changing the size of the learning step, and surface plots for mean velocity components (axial, radial and circumferential). However, they did not discuss the algorithm itself and the effect of changing its parameters, such as learning method, number of neurons, and number of hidden layers… etc.

Ahmed and El Kad **[**17**]** i proposed ANN to predict swirl flow velocity in a dump combustor. The experimental data used in predicting was obtained using LDV. They showed the results of tangential velocity profiles of a free vortex flow obtained from ANN by using axial and radial positions as inputs to the network with one hidden layer and compared them with experimental data, also correlation coefficient factor (CC) and normalized mean square errors were reported in this study as a function of displacements. Nevertheless, the used

ANN algorithm, and the effect of changing some parameters on the ANN efficiency were not mentioned.

Ayhan-Sarac et al. [18] used ANN to enhance a data of heat transfer in a tube with axial swirling-flow, and predict many parameters such as Reynolds number, Nusselt number, friction factor and Irreversible factor for several swirling angle. The predictions achieved by ANN were supported. They concluded that ANN can be useful to produce new values for any flow geometry, which makes ANN be useful to predict heat transfer and fluidflow characteristics. Nevertheless, a brief parametric study was done to show the effect of changing number of neurons on the estimated error. The used algorithm was multi-layer feed-forward network with back-propagation. Table 1.1 summarizes previous studies done in axisymmetric sudden expansion flows and ANN.

Table 1.1 Overview of previous studies in axisymmetric sudden expansion flows and ANN

Author	Re	Swirling method	Swirl number	Experimental technique	Reported results
Yang & Yu [29]	64000	-	0	LDA	Axial and radial velocities, turbulent kinetic energy
Hallett & Gunther [21]	67000	Swirl chamber	1.1-2.06	HWA, smoke visualization, infrared gas analyzer	Axial, radial and tangential velocities, static pressure, frequency spectrum, concentration fluctuations
Khezzar et. al.[25]	120, 1000, >2000	-	0	LDA	Axial, radial and tangential velocities, wall static pressure
Hallet & Toews [8]	1×10^6 - 1.6×10^6	Axial-tangential swirler (4 tangential inlets)	0.3-0.66	5 hole pivot tube, smoke visualization	Axial and tangential velocities, critical swirl numbers
Durrett et. al. [56]	8.4×10^4	-	0	LDA	Axial and radial velocities, Reynolds stresses, turbulent kinetic energy
Dellenback et. al. [3]	30000, 60000,	Tangential entry	0-1.23	LDA	Axial and tangential

	100000				velocities and turbulence intensities, precession frequencies
Sommerfeld & Qiu [57]	52400	Radial swirler (vanes)	0.47	PDPA	Axial, radial and tangential velocities for single particulate flows, particle size distribution and mass fluxes for sizes 30, 45, 60 μm
Nejad & Ahmed [6]	-	Constant angle free and forced vortex swirlers (guide vanes)	0-0.5	LDA	Axial, radial and tangential velocities, axial and angular momentum, swirl strength, wall static pressure
Devenport & Sutton [58]	88000	-	0	PWA, HWA	Axial velocity, axial turbulence intensity, surface pressure
Ahmed [30]	1.5×10^5	Free vortex (vanes)	0, 0.4	LDA	Axial, radial and tangential velocities, Reynolds stresses, triple velocity correlations and turbulent kinetic energy terms
Cole & Glauser [26]	41000	-	0	HWA	Axial, radial and tangential velocities, turbulent kinetic energy terms, correlations
Khezzar [59]	15000	Radial swirler	1.5	LDA	Axial, radial and tangential velocities
Hammad et al. [63]	20, 110, 210	-	0	PIV	Velocity vectors, steam function
Zhou et al.[60]	Up to 47600	Tangential entry	1, 1.5, 2.1	PDPA	Axial, radial and tangential velocities, particle densities for sizes 45, 90 and 35 μm
Furuichi et al. [61]	500-15000	-	0	UVP	Steamwise velocity, spectra, Eigen values, entropy
Wang et. al. [20]	10000-20000	Guide vanes	0, 0.33,	LDV	Axial, radial and tangential

			0.43		velocities
Tinney et. al.[62]	54000	-	0	FHWA	Radial and azimuthal correlations, POD and Fourier azimuthal decomposition
Fernandes et. al. [5]	3.5×10^6-8×10^6	Swirl generator (variable angle blades)	0.5-1.5	LDV, flow visualization, pressure measurements	Precession frequencies, axial and radial velocities, flow structure evolution, helical mode identification
Dwivedi et. al.[15]	8543	-	-	Constant temperature anemometer, X-wire probe	U, V, U'_{rms}, V'_{rms}
Spentzos et. Al. [13]	$1.5X10^6$	-	-	Surface pressure	DSV
Ayan-Sarac et. Al. [69]	4000-32000	-	-	Inclined manometer, thermocouples	Nu, Friction factor, irreversible, logarithmic temperature difference, pressure drop
Pruvost et. Al. [16]	3000	-	-	PIV, laser generator	Velocity components, turbulent intensity
Abdel Gawad A. [32]	1500-170000	-	-	Numerical	Drag coefficient
Zhao et. Al. [33]	-	-	-	Thermocouples, piezo capacitive transducer, venture meter	Nu
Ihme et. Al. [31]	-	-	-	LES (Theoretical)	Velocity Components, mean mixture fraction and mass fraction

1.2 Methodology and Objectives

The main objective of this study is to enhance the knowledge of flowfield characteristics in a sudden expansion model dump combustor; therefore, ANN is utilized to:

1. Predict the behavior of fluid velocities and higher order terms in a model dump combustor.
2. Generate extra profiles with least amount of errors.

3. Compare several networks in order to recommend the best architecture that can be used in implementing such a model.
4. Perform a study to show the effect of changing ANN configuration on implementing the system.
5. Enhance the experimental data with extra data to help in better combustor design.
6. Predict a complete data set for a new swirler for which no experimental data exists.

CHAPTER 2

FLUID FLOW CHARACTETRISTICS

A fluid flow is described as swirl flow when a spiral shape is formed along its axial axis causing a complex three dimensional flow, Swirling flow is used for the stabilization and control of the flame and to achieve a high intensity of combustion. Swirling flow induces a highly turbulent recirculation zone, which stabilizes the flame resulting in better mixing and combustion, swirl in the oxidizer stream also has an effect on pollutant formation during the reaction process by increasing the residence times for the fuel stream. Because of the performance requirements on the design of gas turbine engines, there is considerable interest in identifying optimal swirl conditions to achieve specific practical goals in actual flight regimes, such as reduced emissions, improved efficiency and stability **[**17**]**.

One of the main features that is usually observed in swirling flows is the formation of centretoroidal recirculation zone around the axis of the jet. Earlier studies have shown that swirl of sufficient strength produces an adverse pressure gradient along the axis, which can promote flow reversal or vortex breakdown **[**19**]**. Many factors such as inlet conditions, geometry, tangential velocity profile and axial velocity affect the process of vortex evolution and breakdown process.

Formation of toroidal vortex facilitates the stabilization of the combustion process in a compact region within the combustion chamber. It was found that, the velocity field is sensitive to flow parameter variation for intermediate and low swirl intensity. Also, it was found to be easier to obtain axisymmetry for the flows with high swirl number rather than the flows with intermediate and low swirl numbers **[**20**]**.

The main advantage of the reverse-flow is that both the entering inlet charge end the exiting exhaust gas cause a tendency to swirl in the same

direction in the combustion chamber. In a crossflow head the inlet and exhaust gases promote swirl in opposite directions so that during overlap the swirl changes directions. The constant swirl during overlap which results in a reverse-flow cylinder head promotes better mixing and hence better scavenging of the end gas. The fact that the inlet charge must change direction before going out the exhaust makes it less likely that fresh mixture will make it out the exhaust before mixing during overlap. Overall this improves volumetric efficiency and reduces emissions **[**21**]**.

The swirl number is used to characterize the combustor recirculation and the intensity of swirl in enclosed and fully separated flows. A combustor with a swirl number greater than 0.6 is considered to have good recirculation and a swirl number less than 0.4 is considered to have poor recirculation.

The swirl number is usually defined as the fluxes of angular and linear momentum and it is used for characterizing the intensity of swirl in enclosed and fully separated flows, swirl number is defined as:

$$S_n = \frac{G_\theta}{G_x L} \tag{2.1}$$

Where G_θ is the angular momentum G_x is the axial momentum and L is a characteristic length associated with the flow:

$$G_\theta = \int_{r_i}^{r_o} \left(\rho\, U\, W + \rho\, \overline{u'w'}\right) r^2\, dr \tag{2.2}$$

$$G_x = \int_{r_i}^{r_o} \left(\rho\, \overline{U^2} + \rho\, \overline{u'^2} + (p - p_\infty)\right) dr \tag{2.3}$$

Here, u'_{RMS} and w'_{RMS} are the fluctuating components of velocity in the axial and angular directions, p is the pressure denoted by the fluid and p_∞ is the ambient pressure, both in (Pa) **[**16**]**.

The swirl number should, if possible, be determined from measured values of velocity and static pressure profiles. However, this is frequently not possible due to the lack of detailed experimental results. Therefore, it has been

shown **[**22**]** that the swirl number may be satisfactorily calculated from geometry of most swirl generator. If a perfect mixing and conservation of momentum is assumed, then the swirl number can be defined in term of the geometry of the combustor **[**23**]**.

Characterizing turbulent swirling flows remains thus a challenge in fluid mechanics and a large body of related literature has been published dealing with various flow configurations (confined and unconfined, reacting and non-reacting) and/or specific phenomena such as flow structure and instabilities, flow precession and vortex breakdown **[**24**]**.

A flow geometry which is relevant to many swirling applications, particularly swirl burners and combustors, is that of an axisymmetric sudden expansion. Sudden expansion flows combine geometric simplicity with complex flow features such as separation and reattachment. They share many similarities with the flow past a backward facing step, i.e., the existence of three distinct flow regions: recirculation, reattachment and redevelopment. The reattachment length is an important parameter in sudden expansion flows as it defines the extent of the recirculation and depends on a number of parameters such as Reynolds number, expansion ratio, free stream turbulence [**25**,**26**,**27**], initial **[**28**]** and downstream conditions **[**29**]**.

Imparting swirl to the flow past a sudden expansion alters its character. The exact resulting flow topology depends on the strength of the swirl motion (normally expressed by means of a swirl number), the method of swirl generation and the boundary conditions. Generally, the rate of entrainment of the ensuing jet increases with swirl, the reattachment length decreases, on-axis flow reversal (vortex breakdown) and flow instabilities associated with the precessing jet are established for certain swirl conditions. The confinement and the separating nature of the expansion flow are known to exacerbate the precession and flow instabilities.

CHAPTER 3

EXPERIMENTAL SETUP

This study is aimed to enhance the understanding of the flow features in a confined isothermal swirling flow field by utilizing ANN to predict additional data at different locations. The measurements were made in the horizontal and vertical planes. The results presented here are only for the lateral half section of the combustor since the flow is almost axisymmetric. All the measurements are non-dimensional. For example the axial velocity component is divided by the inlet upstream mean velocity U_o, which equals 16±0.4 m/s, and the axial coordinate is divided by the step height H that equals 25.4 mm.

Upstream of the swirler, the axial turbulence intensity is 5% at the center and increases to 9.5% near the wall with a fully developed pipe flow, while the swirl turbulence intensity increases from 4% at the center to 8% at the wall.

The model where data is captured consists of two major parts; an inlet assembly and a combustion chamber. The inlet assembly contains a settling chamber of 300 mm diameter, a Plexiglas inlet pipe with 2850 mm length and 101.6 mm inner diameter, and a cylindrical Teflon swirler housing that has 104.5 mm inner diameter, 152.4 mm outer diameter, and 154 mm in length. A distinctive property in this model is its capability of dump plane (swirler housing) positioning with respect to station measurement of the combustion chamber. It is accomplished by supporting the entire inlet assembly on a traversing mechanism controlled by a stepper motor. The inlet average velocity is monitored with a flow meter located far upstream of the swirler housing, and maintained at an average velocity $U_o = 16 \pm 0.4$ m/s, corresponding to Reynolds number of 1.5 X 10^5. This velocity is enough to ensure a turbulent flow in the combustor.

The combustion chamber itself contains a Plexiglas tube with 152.4 mm inner diameter and 1850 mm in length, terminating into a larger pipe (exhauster). The measurement station is designed to accept different window assemblies. One is designed to provide optical access for traversing in the horizontal plane.

The swirler type is constant angle, similar to the one used by Ahmed and Nejad **[6]**. The current facility employed a swirler that has 12 curved vanes. Swirler dimensions are 19 mm inner diameter (central hub) and 101.6 mm outer diameter. Figure 3.1 shows a schematic of the setup.

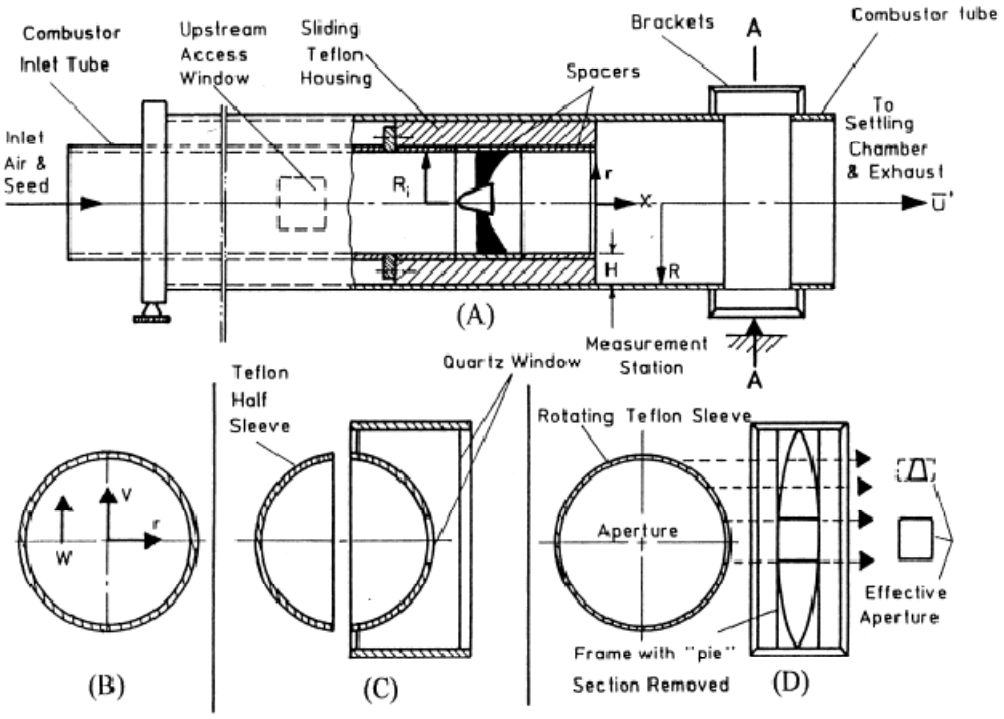

Figure 3.1 Schematic of the experimental setup (A) Dump combustor model (B) Section A-A (C) Assembly for measurement in the horizontal $(U-V)$ plane (D) Assembly for measurement in the vertical $(U-W)$ plane

The measurements of velocity are performed using a TSI Inc. 9100-7 four-beam, two-color, back scatter fiber-optic LDV system. It is occupied with two TSI 9180-3A frequency shifter to provide directional sensitivity. The entire optics are mounted on a three-axis traversing table with a resolution of ±2.5 µm. The system is configured so that the fringe inclinations are at 45.67º and 134.17º

to the combustor centerline. The approximate measurement volume dimensions based on $1/e^2$ intensity points are 390 μm length and 60 μm.

The photomultipliers signals are processed by two TSI burst counters – models 1990 B\C with low pass filters, set at 20 MHz, and a high pass filter set at 100 MHz on each processor. Calculations of statistical moments from standard formulae are done at each measurement location using double precision data (48 bit) **[**6**]**.

The captured data is validated and published by Ahmed **[**30**]**, it consists of four swirl numbers, which are: 0, 0.3, 0.4 and 0.5, each swirl number has profiles at x/H=0.38, 1, 2, 3, 4, 5, 6, 8, 10, 12, 15, and 18. The first seven profiles are called near field profiles (i.e. for x/H=0.38, 1, 2, 3, 4, 5, and 6), while the last five profiles are called far field profiles (i.e. x/H= 8, 10, 12, 15, and 18). At each profile r changes from -3 to 0 for swirl number 0, from 0 to 3 for swirl number 0.3, from 3 to 6 for 0.4 and from 6 to 9 for swirl number 0.5.

The measured turbulence statistics are velocity components in axial (x), radial (r), and tangential (θ) directions $(U, V, and\, W$, respectively), fluctuating velocity components, in x, r, and θ directions, respectively $(u'_{RMS}, v'_{RMS}, and\, w'_{RMS}$, respectively), note that Reynolds normal stresses are calculated by raising these components to the power squared (i.e. $(\overline{u'^2}, \overline{v'^2}, and\, \overline{w'^2}$, respectively), and multiplying them by the density of the fluid, Reynolds shear stresses $(\overline{u'v'}, \overline{u'w'})$, skewness terms S_U, S_V, S_W, and triple velocity product correlations $\overline{u'^2v'}$, $\overline{u'v'^2}$, $\overline{u'w'^2}$, and $\overline{u'^2w'}$.

CHAPTER 4

ARTIFICIAL NEURAL NETWORKS

Since studying fluid flow characteristics is very important and substantial for efficient combustors design; most studying methods are based on experimental mechanisms using several kinds of sensors and actuators to measure velocities, forces and pressures at several coordinate. Particle Image velocity (PIV) and Laser Doppler Anemometry (Velocimetry) (LDV) are some of the techniques used for measuring swirl flow velocity field. However, because of the limited (discrete) data can be provided by these techniques, a new methodology is considered here to provide additional set of information. ANN is suggested to provide useful results that can be used to enlarge the set of data, therefore, enhancing dump combustors design [13].

ANN has become one of the most popular tools in data classification and prediction. Recently, many researchers [31,32,33] have used ANN to produce vast amount of data by training the network and produce new set of data.

ANN is a computational model of the brain; its structure consists of interconnected units (artificial neurons) with each unit has an input and output characteristic and implements a local computation or function. The output of any unit is determined by its input and output characteristic, its interconnection to other units and any external inputs if they exist.

Many engineering applications [34,35,36] have used ANN, and good success has been observed in image processing and computer vision, signal processing, pattern recognition, medicine, like electrocardiographic signal analysis, military systems, such as undersea min detectors, financial systems, stock market analysis is an example, power systems, human interfacing and artificial intelligence [37].

From above, it can be noticed that ANN can be used whenever a set of data is available, to train the network and making it familiar with the way how such an application works, like training a newborn child how to walk.

Any ANN consists of group of interconnected elements called processing elements (PEs) or artificial neurons, or simply neurons or nodes; each neuron carries out a specific weight from each input of the network. If the network is linear, then the output of each neuron is simply the summation of all input weights feeding that neuron. However, if the network is nonlinear, then each node can be represented by a transfer function, and the output of that neuron is the weighted sum of inputs.

All ANN consist of three types of layers: input, hidden and output layers. The input layer is the layer contains neurons that represent the number of inputs of the system. The hidden layer is the one holds the processing elements that carry the weights and their updates to the next layer. The output layer is the last layer in the architecture of the ANN which consists of the neurons that obtain the total weights of the previous layers, the number of neurons in the output layer equals the number of outputs of the modeled system. Each layer contains number of neurons that are fed from the previous layer and feed the next neurons layer. At least ANN should have 2 layers: input and output, then it is called single layer ANN. If the network contains at least one hidden layer, the network is then called multilayered NN. Figure 4.1 shows a simple schematic of multilayered NN, note the interconnections between neurons are represented as arrows, no connection should be between neurons in the same layer.

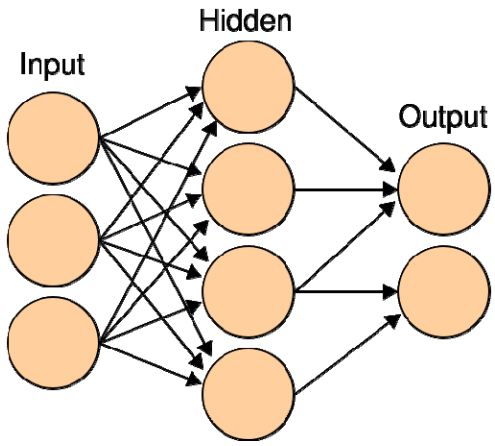

Figure 4.1 Multilayered neural network

If the interconnections or arrows are going in one direction, (i.e. with no feedback), hence the network is called feedforward network. Many types of feedforward networks, such as: Multi-Layer Perceptron network (MLP), Learning Vector Quantization network (LVQ), Cerebellar Model Articulation Control network (CMAC), Radial Basis Function network (RBF) and Group Method of Data Handling network (GMDH).

When the output of a neuron or some neurons is feedback to a neuron in a previous layer, the network is called recurrent network. Examples of such networks are: Hopfield network, Elman network, Jordan network and Classification and Regression Trees (CART) and the Neuro-Fuzzy Inference System (NFIS) Network (CANFIS).

There are various ways to configure ANN to let the desired output(s) meet(s) the application requirement. One way by setting the weights individually, this way can be used if the user is familiar with the input data and has enough information (well experienced) with the problem. Another way, which is the common one, is to train the network with a set of data; hence, the network can adjust its weights using one of the learning rules.

ANN can work by teaching it, this step is called learning; there are mainly two learning algorithms:

1. Supervised learning: from its name, supervised leaning needs supervision, which means to provide the network with outputs, from these outputs, the network adjusts weights of neuron connections based on the difference between the actual and desired outputs. Generalized delta rule or backpropagation algorithm (BP) and LVQ algorithm are examples of this learning type.
2. Unsupervised (self-organized) learning: this type of learning does not need information from the desired output, the only considered factor here is input weights and the network changes these weights automatically to divide inputs into groups with similar features. Examples of this algorithm are Kohonen algorithm and Carpenter-Grossberg Adaptive Resonance Theory algorithm (ART).

Some of the advantages of ANN are **[**38**]**:

- Inherently massive parallel
- Can be fault tolerant because of parallelism
- Can be designed to be adaptive and optimum
- Little need for extensive characterization of problem

Nevertheless, some disadvantages can make the method difficult to implement in some applications; these disadvantages can be summarized in the following:

- No clear rules or design guidelines for arbitrary application
- No general way to access the internal operation of the network
- Training may be difficult or impossible
- Difficult to predict future network performance (generalization)

From last point, it can be concluded that ANN can implement a model perfectly and generates good data in interpolation schemes. However, it was shown that ANN cannot give good approximations for extrapolation [39], unless the nature of the implemented function or formula in the extrapolated region behaves in a similar way as in the region used for training the network.

4.1 Training and Testing

In general, the more training and testing data, the more successive implementation can be achieved by ANN. One important thing is also to provide some noise in the data, to help the network in recognizing such randomness can be added to the data, this gives more sufficient representation of the model.

First step should be taken before start training is to choose the number of neurons in hidden layers, of course there is no need to think about number of neurons in input and output layers, since they equal the inputs and outputs of the model, respectively. Mostly, as number of neurons increase in hidden layers, a better prediction should be expected from the network, this means, a few numbers of neurons often cannot manage to solve the problem, but this should not be generalized.

Another factor that effects on the speed of network learning is the initial weights of neurons interconnection, a good guess yields to a quick learning, this can be achieved by having initial values close to global minimum error. However, there is no recommendation for choosing those values. The only way is by trial and error. In order to construct any ANN, there are several parameters that should be optimized; these parameters can be tested as follow:

4.2 Neural Network Configuration

The first step in constructing any ANN is to identify the inputs and outputs (also called desired) data of the model. The data is then divided into 2 sets; training set and testing set. There are 2 methods of choosing training and testing data, one method is to choose random testing set points all over the data,

in this case, if testing results give appropriate values of correlation and NMSE, and this guarantees a successful implementation of the model over the whole range. The other method is by removing a specific profile, i.e. a complete profile is selected to compare the generated profile from ANN with that profile generated from experiments, this way is more useful when the plotted data is predicted by the designer and helps in easy comparison the results obtained from the network. The second method is the one that is used here.

Once ANN is constructed, it is trained on all the data but one profile, which is chosen as testing data, then the correlation coefficient (CC) and normalized mean squared error (NMSE) can be calculated. The correlation coefficient is defined as:

$$CC = \frac{\frac{\sum_i (x_i - \bar{x})(d_i - \bar{d})}{N}}{\sqrt{\frac{\sum_i (d_i - \bar{d})^2}{N}} \sqrt{\frac{\sum_i (x_i - \bar{x})^2}{N}}} \tag{4.1}$$

Where x is the network output, d is the desired output, $\bar{x}$ is the mean network output, $\bar{d}$ is the mean desired output, and N is the number of exemplars. The NMSE is defined as:

$$NMSE = \frac{P\ N\ MSE}{\sum_{j=0}^{P} \frac{N \sum_{i=0}^{N} d_{ij}^2 - \left(\sum_{i=0}^{N} d_{ij}\right)^2}{N}} \tag{4.2}$$

Where P is the number of output processing elements, N is the number of exemplars, MSE is the mean squared error, and d_{ij} is the desired output for exemplar i at processing element j. MSE is defined as:

$$MSE = \frac{\sum_{j=0}^{P} \sum_{i=0}^{N} \left(d_{ij} - y_{ij}\right)^2}{N\ P} \tag{4.3}$$

Where y_{ij} is the network output for exemplar i at processing element j.

4.3 Neural Network Selection

As mentioned before, the first step is to find the most accurate ANN with the best configurations that predict the turbulence statistics precisely. The comparison between the used ANN is done for three turbulence statistics $(U, V, and\ W)$ at two swirl numbers (0 and 0.5), and then the network with highest average correlation coefficient and least NMSE is selected.

4.3.1 Selection of Learning Rule

Learning is the process of modifying network parameters to improve the performance of the network, there are many algorithms that can be utilized to train the network and obtain results, such as step rule, momentum rule, Hebbian learning algorithm, Levenberg–Marquardt algorithm (LM), perceptron learning rule and delta bar delta rule. The selection of learning rule is done by comparing the network outputs with the desired ones. The compared learning rules are: Levenberg-Marquardt, Conjugate Gradient (CG), Step, and Momentum learning rules. Appendix A contains a brief description of learning rules.

The comparison is made by training the network on the whole data except one profile, the first training is done by excluding profile x/H=3, then profile x/H=6 is excluded at the second time, and similarly for the third time, where profile x/H=10 is the excluded one. For all velocity components, Levenberg-Marquardt learning rule gives the best predictions. Figure 4.2 shows the average correlation coefficient of predicting axial velocity component for x/H=3, 6, 10 at 0.5 swirler as a function of learning rule, the correlation coefficient of predicting U is 0.98693, while for V and W, the values of CC are 0.97658 and 0.992712, respectively.

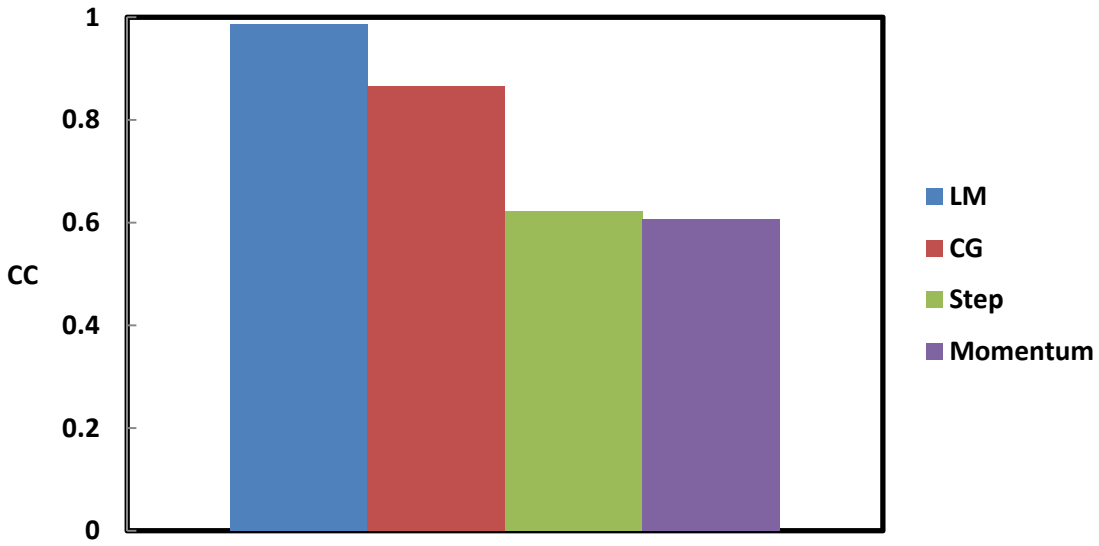

Figure 4.2 Average CC of testing U at x/H=3, 6, 10 for 0.5 swirler as a function of learning rule

4.3.2 Selection of Transfer Function

The same procedure is followed to choose the transfer function, the compared transfer functions are Tanh Axon, Sigmoid Axon, Linear Tanh Axon, Soft Max Axon, Bias Axon, and Axon.[1]

After training and testing the networks on the velocity components, the best predictions are for TanhAxon networks. The values of average CC for $U, V,$ and W are 0.986938, 0.974824, and 0.9903571, respectively. Figure 4.3 shows the average correlation coefficient of predicting axial velocity component for x/H=3, 6, 10 at 0 and 0.5 swirlers as a function of transfer function.

From this comparison, Levenberg-Marquardt learning rule and TanhAxon transfer function are used to construct GFF, RBF, and CANFIS networks.

[1] Refer to Appendix A for description about Transfer function

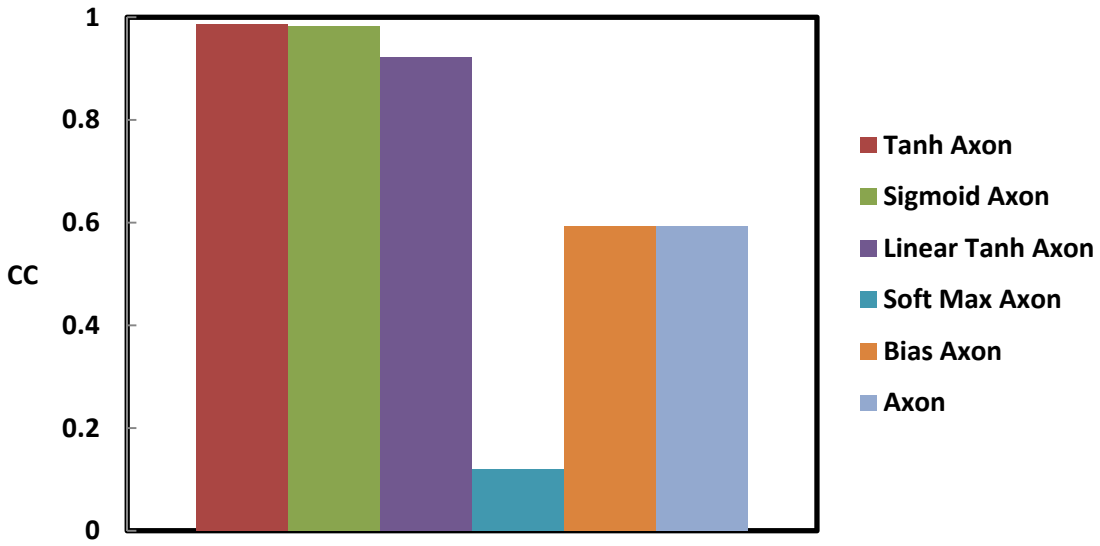

Figure 4.3 Average CC of testing U at x/H=3, 6, 10 for 0.5 swirlers as a function of transfer function

4.3.3 Generalized Feedforward Network Configuration

Generalized feedforward networks are a special case of multilayer perceptrons such that connections can jump over one or more layers. In theory, a MLP can solve any problem that a generalized feedforward network can solve. In practice, however, the generalized feedforward networks often solve the problem much more efficiently. The advantage of the generalized FF network is in its ability to project activities forward by bypassing layers. The result is that the training of the layers closer to the input becomes much more efficient.

If one hidden layer is considered, the output of that layer can always be written as $y = xw$, where x is the input, and w is the weight vector. Using ridge regression; which establishes a solution for second order learning methods, it gives:

$$w_K = (x^T x + K)^{-1} x^T y \tag{4.4}$$

Where $K = \gamma I$, I is the identity matrix, γ>0, and $\gamma \in R$. $w_K = w_\gamma = (x^T x + \gamma I)^{-1} x^T y$. This gives the ordinary ridge estimator. When K is a

diagonal matrix of biasing factors γ_i, it becomes the generalized ridge estimator. In either case, the estimators are the minima of the form:

$$C(w) = (y - xw)^T(y - xw) + \frac{1}{2}w^T K w \tag{4.5}$$

Equation (4.4) is indeed a mean square error term together with a weight decaying term. Previous study showed that $E(w_K - w^*)^T(w_K - w^*) < E(w_o - w^*)^T(w_o - w^*)$ for some $0 < k < k_{max}$. w^* and w_o are optimal weight vector and the solution of the ordinary least square error method, respectively [**40**].

4.3.3.1 Selection of Number of Processing Elements

To accurately configure GFF network, a comparison is done for generalized feedforward networks with different configurations, in other words, to calculate the average correlation coefficient as a function of number of neurons.

The investigated parameter is the number of neurons. The network is trained on the whole profiles but one, the excluded profiles are at x/H=3, 6, and 10, at every training, one of the profiles is excluded, then the correlation coefficient is calculated after testing the network on the excluded profile. After that, the correlation coefficient is calculated, and the average value is taken for the three trainings. This process is done for 0.5 swirler. Figure 4.4 shows that the best predictions are obtained at 19 neurons with CC= 0.996731, therefore, this network is selected to predict the rest of data for the axial velocity component.

Similarly, the best obtained networks for radial and tangential velocity components are at 11 and 18 processing elements, respectively, with CC of 0.981133 and 0.997103, respectively, as shown below. Note that this comparison cannot give a final decision on the used number of neurons, since many other parameters affect on the networks.

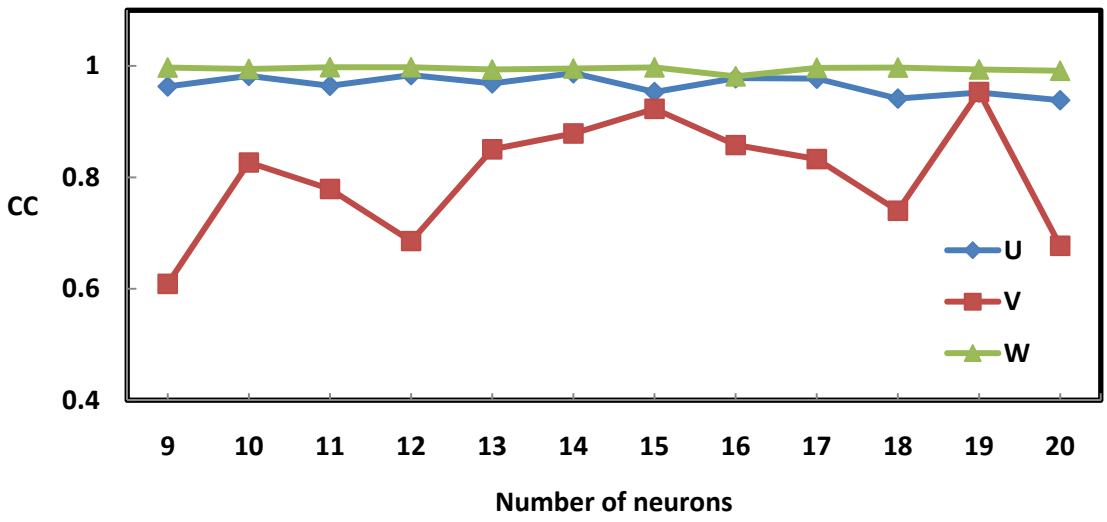

Figure 4.4 Average CC of testing U, V, and W at x/H=3, 6, 10 for 0.5 swirlers as a function of number of neurons

4.3.4 Radial Basis Function Network Configuration

The RBF network is a feedforward structure with modified hidden layers and training algorithm. A single hidden layer consists of locally tuned units, where the response is localized and decreases as a function of inputs distances from the unit's center. The output layer consists of linear units in most cases [41].

RBF networks may require more neurons than generalized feedforward MLP networks, but they can be designed in less time.

RBF network are recommended to be used when the system model has a radial tendency, in other words, the model behaves always towards the center of the system.

Many fields were RBF has been used, such as control, speech processing, vision and image processing and pattern recognition. Figure 4.5 illustrates an example of RBF network, note the interconnection relationships.

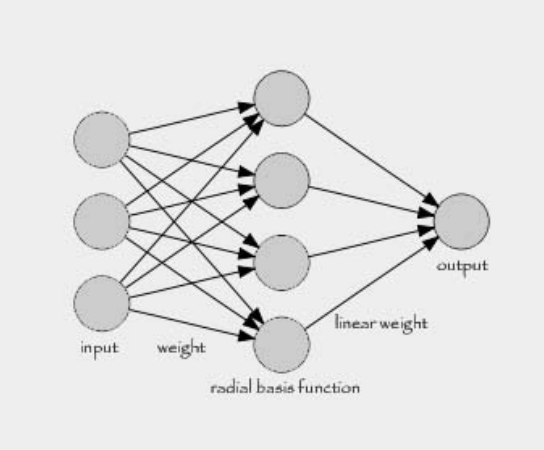

Figure 4.5 RBF network [42]

The goal of competitive networks is to cluster or categorize the input data. The user defines the number of categories, but their coordinates are determined without supervision. There are an enormous number of applications for such networks. Data encoding and compression through vector quantization comprise one important class of applications. Radial Basis Function network is one type of competitive networks.

Radial basis functions networks have a very strong mathematical foundation rooted in regularization theory for solving ill-conditioned problems. Suppose that we want to find the map that transforms input samples into a desired classification. Due to the fact that we only have a few samples, and that they can be noisy, the problem of finding this map may be very difficult (mathematicians call it ill-posed). We want to solve the mapping by decreasing the error between the network output and the desired response, but we want to also include an added constraint relevant to our problem. Normally this constraint is smoothness. Bring every input component (p) to a layer of hidden nodes. Each node in the hidden layer is a p multivariate Gaussian function:

$$G(x; x_i) = e^{\frac{-1}{2\sigma_i^2}\sum_{k=1}^{p}(x_k - x_{ik})^2} \tag{4.6}$$

Of mean x_i (each data point) and variance σ_i. These functions are called radial basis functions. Finally, linearly weight the output of the hidden nodes to obtain:

$$F(x) = \sum_{i=1}^{N} w(G(x; x_i)) \tag{4.7}$$

One disadvantage gained from this solution, which it may lead to a very large hidden layer (the number of samples of training set). Thus an approximation is proposed to simplify the solution by reducing the number of PEs in the hidden layer, but cleverly position them over the input space regions, i.e. where we have more input samples. This means that an estimation of the positions of each radial basis function and its variance (width) is needed, as well as compute the linear weights.

The most widely used method of estimating the centers and widths is to use an unsupervised technique called the k-nearest neighbor rule **[**41**]**. The input space is first discretized into k clusters and the size of each is obtained from the structure of the input data. The centers of the clusters give the centers of the RBFs, while the distance between the clusters provide the width of the Gaussians. The definition of the width is nontrivial. Conscience can be used to make sure that all the RBF centers are brought into the data clusters. However, conscience also brings the problem of confining the centers too close together. Scheduling of the conscience may be necessary for a good coverage of the data clusters.

The output weights in turn are obtained through supervised learning. This problem is easier because the output unit is normally linear, so convergence is faster. In practical cases, an MLP can be superior to the linear network, because it may take advantage of nonlinearly separable data clusters produced by too few RBFs.

4.3.4.1 Selection of Competitive Rule

Competitive learning weight updates are applied on a winner take all basis. In other words, only the weights that feed the most active output are adjusted. Like all components in the unsupervised family. Competitive components are defined through their weight update function. However, this function is now only applied to the winning index. The StandardFull is a component that implements competitive learning, where the weights of a single winning neuron will be moved towards the input. The ConscienceFull is a special type of competitive learning that keeps track of how often the outputs win the competition with the goal of equilibrating the winnings (i.e., each unit in a set of N will win the competition 1/N on average). This implements a second level of competition among the elements to determine which PE is going to be updated. It avoids the common occurrence in competitive learning that one element (or a subset) may always win the competition.

In order to select the appropriate competitive rule, a comparison between these two rules is establish by finding the average correlation coefficient after training the network with all profiles except one profile. Again the excluded profiles are at x/H=3, 6, and 10. Figure 4.6 shows the average correlation coefficient of testing axial velocity component for x/H=3, 6, 10 at 0.5 swirlers as a function of competitive rule and cluster size. In general, CF competitive rule gives better predictions. The highest average CC is 0.899411, which is obtained by using CF rule with cluster size of 19.

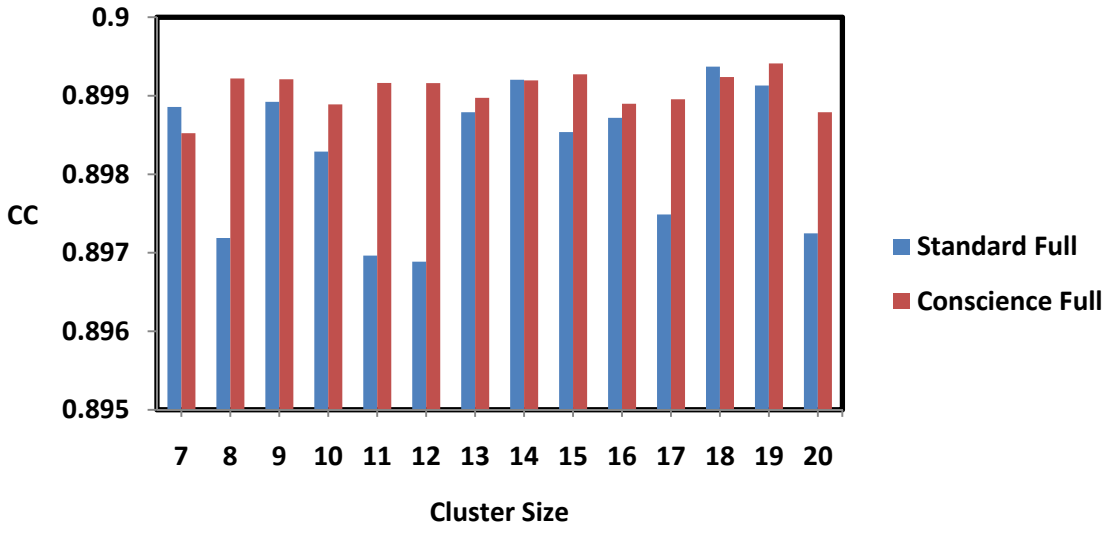

Figure 4.6 Average CC of testing U at x/H=3, 6, 10 for 0.5 swirlers as a function of competitive rule and cluster size

4.3.4.2 Selection of Metric Type

As mentioned before, the Competitive family consists of two components, StandardFull and ConscienceFull. The first component implements the standard competitive rule summarized above. With this rule, there are cases when one PE will win the competition too much, causing the output to be skewed. The second component implements the "competitive with a conscience" learning rule. This rule adds a bias term to balance the competition, which reduces this problem.

The components of the Competitive family are often used in conjunction with a WinnerTakeAllAxon [38]. This component will extract the winning PE of the competition. For the Dot Product metric, the winning PE is the one with the maximum value. For the other two metrics, the winning PE is the one with the minimum value. Equation (4.7) defines the formulae of the compared metric types.

$$y_i = \begin{cases} \sum_j x_j w_{ij} & Dot\ Product \\ \sqrt{\sum_j (x_j - w_{ij})^2} & Euclidean \\ \sum_j |x_j - w_{ij}| & Box\ Car \end{cases} \quad (4.8)$$

Figure 4.7 shows the Average CC of predicting axial velocity component for x/H=3, 6, 10 at 0 and 0.5 swirlers as a function of metric type and cluster size. The highest average CC for all metric types are obtained by using Euclidean type for all cluster sizes. The highest CC value for U is 0.899131, at cluster size of 19.

As a conclusion, Standard Full competitive rule with Euclidean metric type are used to construct RBF networks.

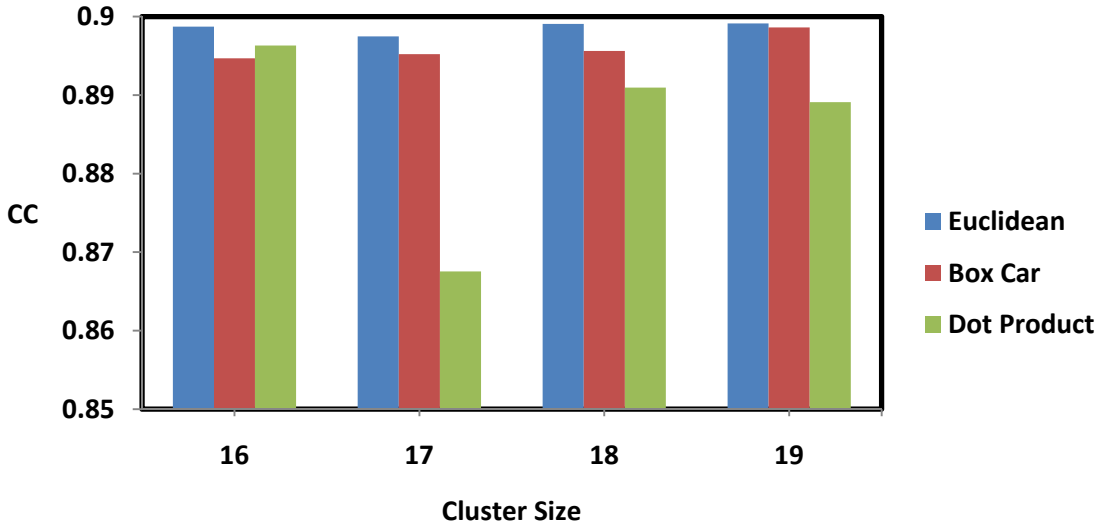

Figure 4.7 Average CC of testing U at x/H=3, 6, 10 for 0.5 swirlers as a function of metric type and cluster size

4.3.5 CANFIS Network Configuration

CANFIS is a combination between Classification and Regression Trees (CART) and the Neuro-Fuzzy Inference System (NFIS) in a two step procedure. CART is a tree-based algorithm used to optimize the process of selecting

suitable predictors from a large set of predictors. Using the selected predictors, NFIS builds a model for continuous output of the predictand [37].

CANFIS powerful capability comes from pattern-dependent weights between consequent layer and fuzzy association layer. Membership values correspond to those dynamically changeable weights that depend on input patterns.

The fundamental component for CANFIS is a fuzzy neuron that applies membership functions (MFs) to the inputs. Two membership functions commonly used are general Bell and Gaussian. The network also contains a normalization axon to expand the output into a range of 0 to 1. The second major component in this type of CANFIS is a modular network that applies functional rules to the inputs. The number of modular networks matches the number of network outputs, and the number of processing elements in each network corresponds to the number of MFs. CANFIS also has a combiner axon that applies the MFs outputs to the modular network outputs. Finally, the combined outputs are channeled through a final output layer and the error is back-propagated to both the MFs and the modular networks.

The function of each layer is described as follows:

1. Each node in Layer 1 is the membership grade of a fuzzy set (A, B, C, or D) and specifies the degree to which the given input belongs to one of the fuzzy sets.
2. The fuzzy sets are defined by three membership functions.
3. Layer 2 receives input in the form of the product of all output pairs from the first layer.
4. The third layer has two components; the upper component applies the membership functions to each of the inputs, while the lower component is a representation of the modular network that computes, for each output, the sum of all the firing strengths.

5. The fourth layer calculates the weight normalization of the output of the two components from the third layer and produces the final output of the network. The architecture of CANFIS network is presented in figure 4.8.

One disadvantage of CANFIS, like any ANN, is that it should not be used to extrapolate values outside the extreme contained in the learning database. This limitation becomes less relevant with increased database size.

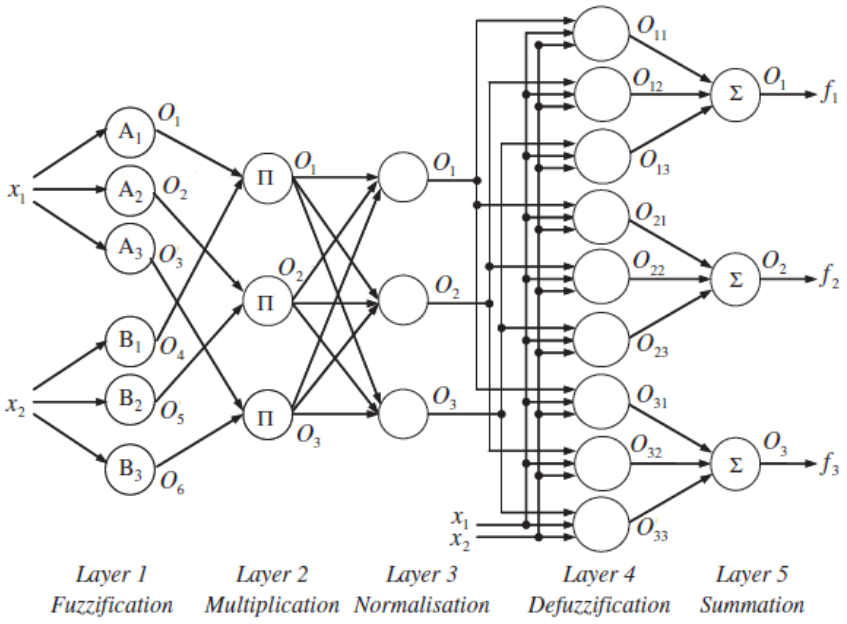

Figure 4.8 CANFIS network structure [37]

The CANFIS neuro-fuzzy modular network computes a weighted sum of the outputs of a certain number of MLPs, this leads to optimize all the parameters by minimizing the sum over all data of squared errors.

The CANFIS model integrates adaptable fuzzy inputs with a modular neural network to rapidly and accurately approximate complex functions. Fuzzy inference systems are also valuable, as they combine the explanatory nature of rules (MFs) with the power of neural networks. These kinds of networks solve problems more efficiently than neural networks when the underlying function to model is highly variable or locally extreme **[**43**]**. The fundamental component of

CANFIS is a fuzzy axon, which applies membership functions to the inputs. The output of a fuzzy axon is computed using the following formula:

$$f_j(x, w) = min\forall_i(MF(x_i, w_i)) \tag{4.9}$$

This system can be viewed as a special three-layer feed forward neural network. The first layer represents input variables, the middle (hidden) layer represents fuzzy rules and the third layer represents output variables.

To illustrate the architecture of any CANFIS network, consider a CANFIS structure with *n* inputs and one output. For model initialize, a common rule set with *n* inputs and *m* IF-THEN rules.

Layers in CANFIS structure can be adaptive or fixed and their functions are:

Layer 1 (Premise Parameters): Every node in this layer is a complex-valued membership function μ_{ij} with a node function:

$$o_{1,ij} = \left|\mu A_{ij}(z_i)\right| \llcorner\, \mu A_{ij}(z_i) \text{ for } 1 \le i \le n, 1 \le j \le m \tag{4.10}$$

Each node in layer 1 is the membership grade of a fuzzy set A_{ij} and specifies the degree to which the given input belongs to one of the fuzzy sets.

Layer 2 (Firing Strength): Every node in this layer is product of all the incoming signals. This layer receives input in the form of the product of all the output pairs from the first layer:

$$o_{2,ij} = w_j = \mu A_{i1}(z_1)\mu A_{i2}(z_2), \dots, \mu A_{in}(z_n) \text{ for } 1 \le i \le m \tag{4.11}$$

Layer 3 (Normalized Firing Strength): Every node in this layer calculates rational firing strength:

$$o_{3,j} = \overline{w}_j = \frac{w_j}{\sum_{j=1}^{m} w_j} \text{ for } 1 \le j \le m \tag{4.12}$$

Layer 4 (Consequence Parameters): Every node in this layer is multiplication of Normalized Firing Strength from the third layer and output of neural network:

$$o_{4,j} = \overline{w}_j u_j = \overline{w}_j (P_{J1} Z_1 + P_{J2} Z_2 + \cdots + P_{Jn} Z_{2n} + q_j \text{ for } 1 \leq j \leq m \qquad (4.13)$$

Layer 5 (Overall Output): The node here computes the output of CANFIS network:

$$o_{5,1} = \sum \overline{w}_j \, u_j \qquad (4.14)$$

4.3.5.1 Selection of Fuzzy Model

There are two fuzzy structures to choose from, the Tsukamoto model and the TSK model. The Tsukamoto is the less complex of the two structures. Tsukamoto model gives higher prediction than TSK. The highest obtained average CC value of predicting U is 0.99497 when Gaussian function is used with 6 membership functions.

4.3.5.2 Selection of Membership Function

There are two types of membership functions, the Bell and Gaussian. The Bell model is a type of fuzzy model that uses a bell-shaped curve as its membership function. Each membership function takes 3 parameters, which are stored in the weight vector of the BellFuzzyAxon. Equation (4.15) defines Bell membership function as:

$$MF(x_j, w_i) = \frac{1}{1 + \left| \frac{x_j - w_{i+1}}{w_{i-1}} \right|^{2w_i}} \qquad (4.15)$$

The Gaussian model is a type of fuzzy model that uses a gaussian-shaped curve as its membership function. Each membership function takes 2 parameters, which are stored in the weight vector of the GaussianFuzzyAxon. Equation (4.16) defines Gaussian membership function as:

$$MF(x_j, w_i) = e^{-\frac{1}{2}\left(\frac{x_j - w_{i-1}}{w_i}\right)^2} \qquad (4.16)$$

Figure 4.9 shows that the highest Average correlation coefficient of predicting tangential velocity component for x/H=3, 6, 10 at 0.5 swirler is 0.995634 by using Gaussian model with 4 membership. Since neither Bell nor Gaussian functions give an absolute indication results, both are used in constructing CANFIS networks.

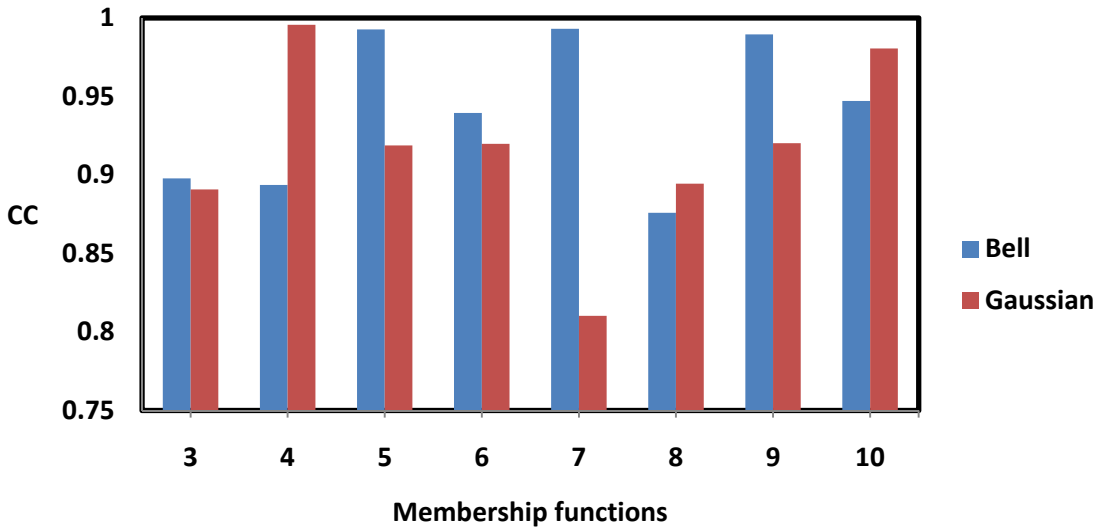

Figure 4.9 Average *CC* of testing *W* at x/H=3, 6, 10 for 0.5 swirlers as a function of membership function and number of membership functions

For all three networks, the used learning rule is Levenberg-Marquardt, the transfer function is TanhAxon. For RBF network, the competitive rule is Standard Full with Euclidean metric type, and for CANFIS network, TSK model is used. After finding the common used structure for GFF, RBF, and CANFIS networks, the remaining parameters investigation of choosing the best ANN is first done on all of the profiles, and then only the near field profiles are presented in this study, since they are the region of interest, where significant changes occur.

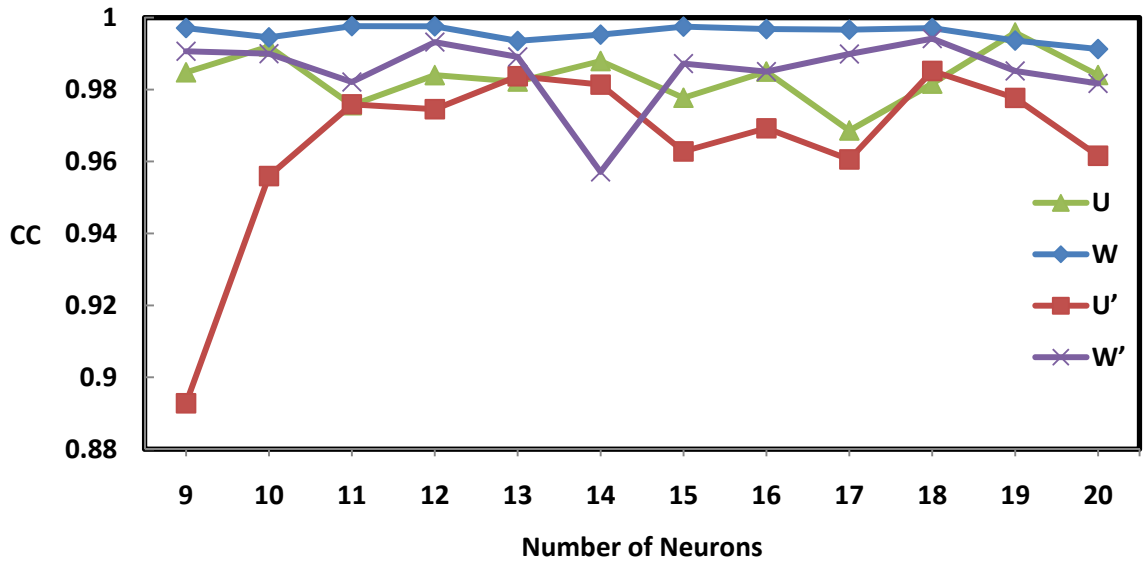

Figure 4.10 Average CC of testing GFF network for U, W, u'_{RMS}, and w'_{RMS} at x/H=3, 6, 10 as a function of number of neurons

The comparison is made between GFF, RBF, and CANFIS networks, as a function of processing elements for GFF network, cluster size for RBF network, and membership function and number of it for CANFIS network.

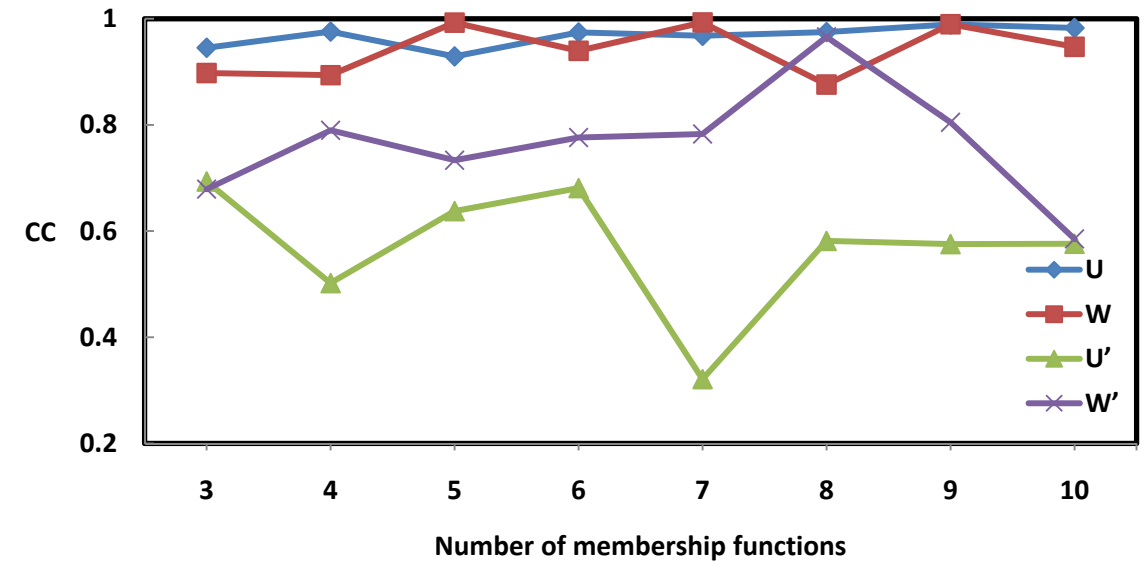

Figure 4.11 Average CC of testing Bell CANFIS network for U, W, u'_{RMS}, and w'_{RMS} at x/H=3, 6, 10 as a function of number of membership functions

Figure 4.10 shows the average correlation coefficient of testing U, W, u'_{RMS}, and w'_{RMS} respectively, as a function of number of neurons for GFF network, while figure 4.11 and 4.12 show the average correlation coefficient of testing U, W, u', and w', respectively, as a function of number of membership function for Gaussian and Bell fuzzy CANFIS networks, and figure 4.13 shows the average correlation coefficient of testing U, W, u'_{RMS}, and w'_{RMS}, respectively, as a function of cluster size for RBF network.

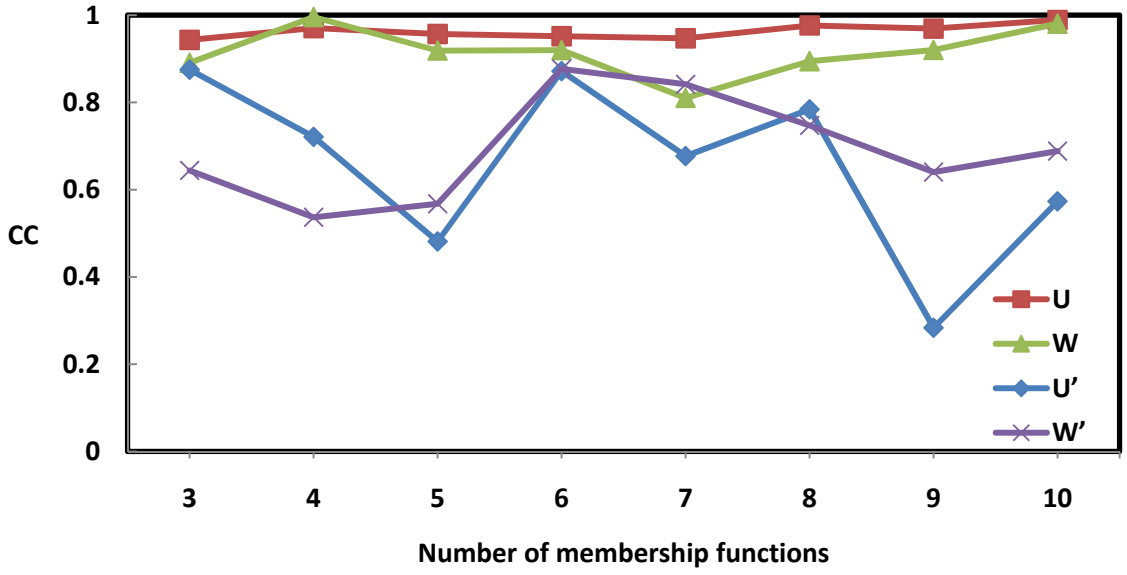

Figure 4.12 Average CC of testing Gaussian CANFIS network for U, W, u'_{RMS}, and w'_{RMS} at x/H=3, 6, 10 as a function of number of membership functions

Figure 4.14 is similar to figure 4.10, but for $V, v'_{RMS}, \overline{u'v'}$, and $\overline{u'w'}$, while figure 4.15 and figure 4.16 are similar to figure 4.11 and figure 4.12, respectively, but for testing $V, v'_{RMS}, \overline{u'v'}$, and $\overline{u'w'}$, also figure 4.17 is the same as figure 4.13, except it includes $V, v'_{RMS}, \overline{u'v'}$, and $\overline{u'w'}$ instead of U, W, u'_{RMS}, and w'_{RMS}. The figures show that testing results achieved by GFF network are the most efficient ones, since their correlation coefficient values are the highest.

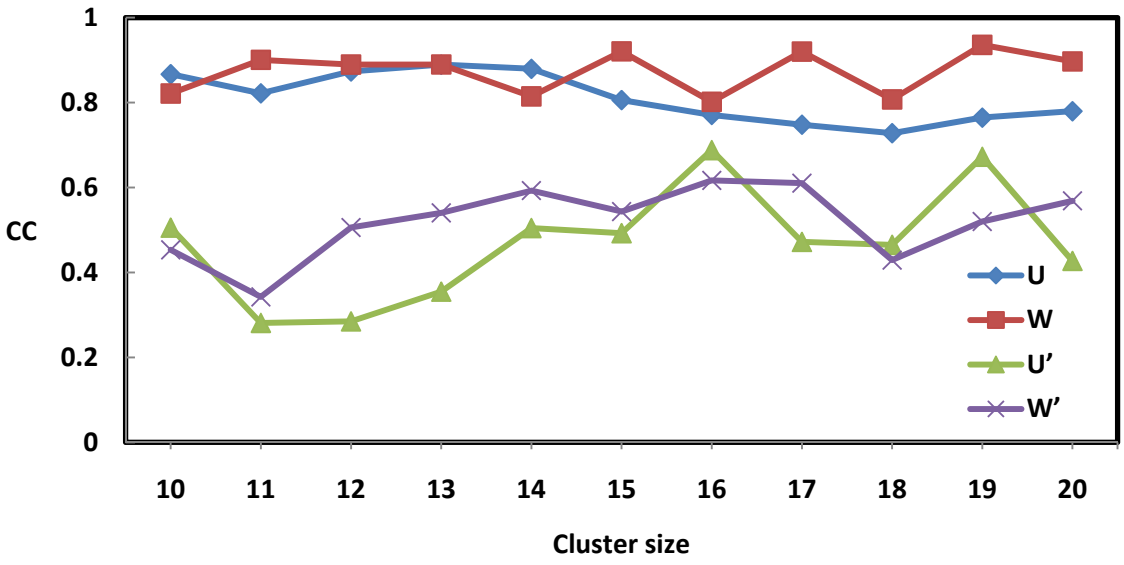

Figure 4.13 Average CC of testing RBF network for U, W, u'_{RMS}, and w'_{RMS} at x/H=3, 6, 10 as a function of number of cluster size

GFF network is able to predict most turbulence statistics because of:

1. Adaptive when learning, this gives an ability to learn how to converge based on the data given for training.
2. One of the techniques that utilize higher order learning rules effectively, since all neurons are interconnected which means that weights are configured properly.
3. GFF networks do not make any assumption regarding the underlying probability density functions or other probabilistic information under consideration in comparison to other probability based models.
4. They yield the required decision function directly via training.
5. One hidden layer network with sufficient hidden nodes has been proven to be a universal approximator **[**44**]**.
6. It uses the universal approximation theorem, which states that every continuous function that maps intervals of real numbers to some output interval of real numbers can be approximated arbitrarily closely by a multi-layer perceptron with just one hidden layer.

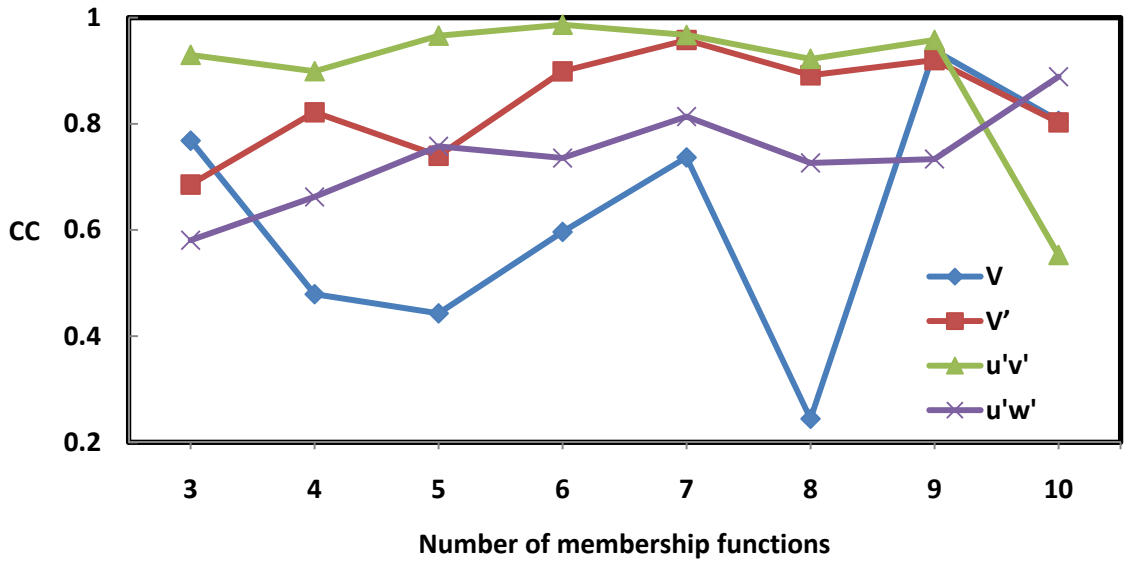

Figure 4.14 Average CC of testing GFF network for $V, v'_{RMS}, \overline{u'v'}$, and $\overline{u'w'}$ at x/H=3, 6, 10 as a function of number of neurons

However, RBF networks were unable to perform this task because they cannot deal effectively with irrelevant features; they also use same weights for all neurons because all of them are treated equally in the distance of computation. Hence, they cannot deal effectively with irrelevant functions.

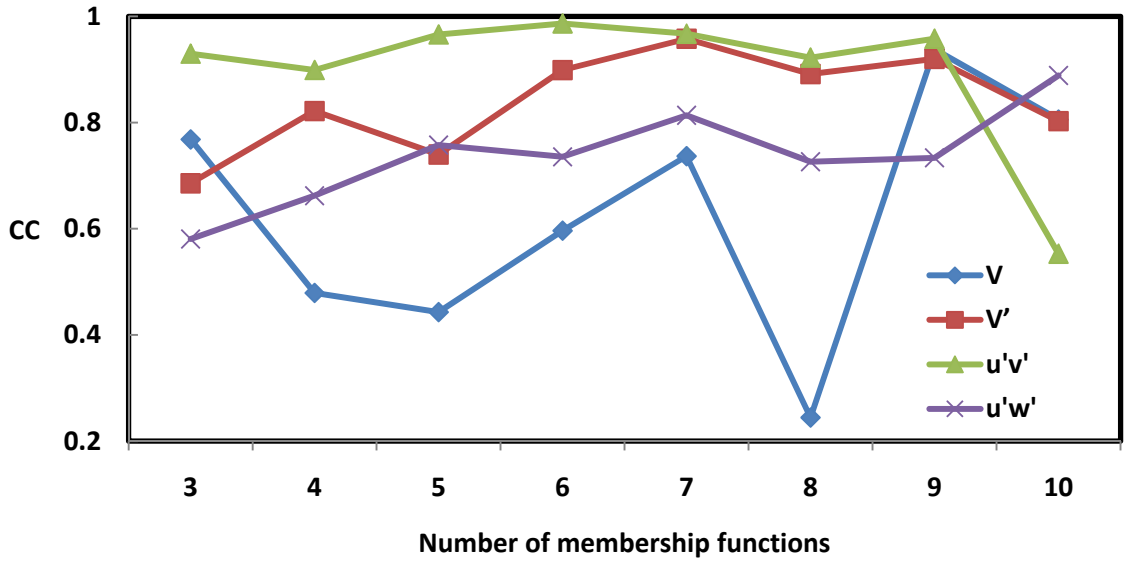

Figure 4.15 Average CC of testing Bell CANFIS network for $V, v'_{RMS}, \overline{u'v'}$, and $\overline{u'w'}$ at x/H=3, 6, 10 as a function of number of membership functions

The main disadvantage that prevents CANFIS network from predicting turbulence statistics of such model is that the fuzzy model lacks accuracy in the input–output mapping, since the use of the fuzzy if-then rules in the FIS are generally incomplete and insufficient to describe the input–output relationships. Another disadvantage is that sufficient data base volume is required to build the model. As such it is not capable of direct prediction for sites which have a lack of archived observations.

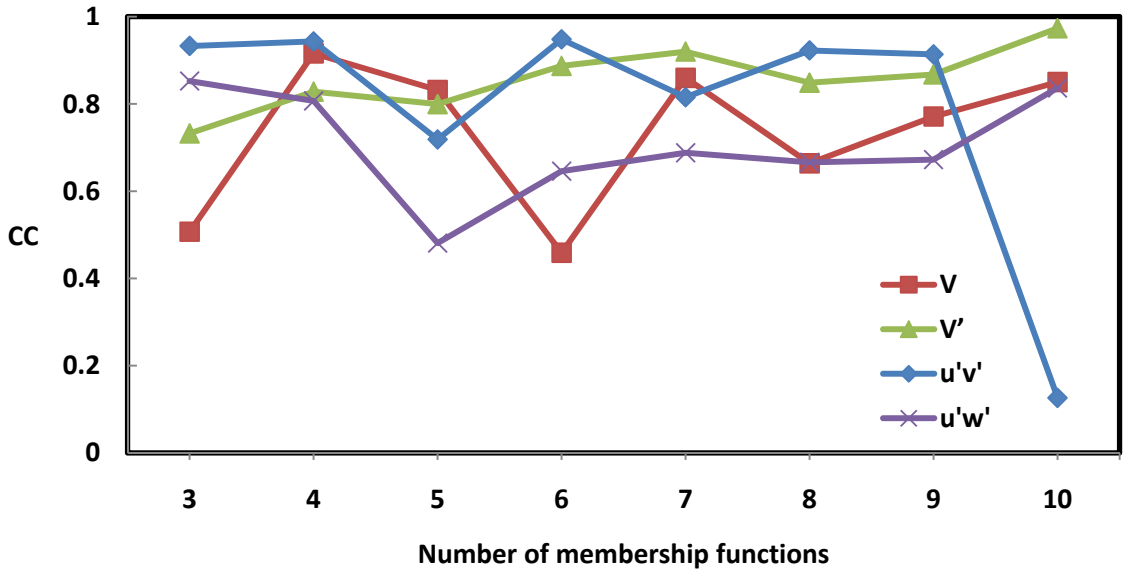

Figure 4.16 Average CC of testing Gaussian CANFIS network for $V, v'_{RMS}, \overline{u'v'}$, and $\overline{u'w'}$ at x/H=3, 6, 10 as a function of number of membership functions

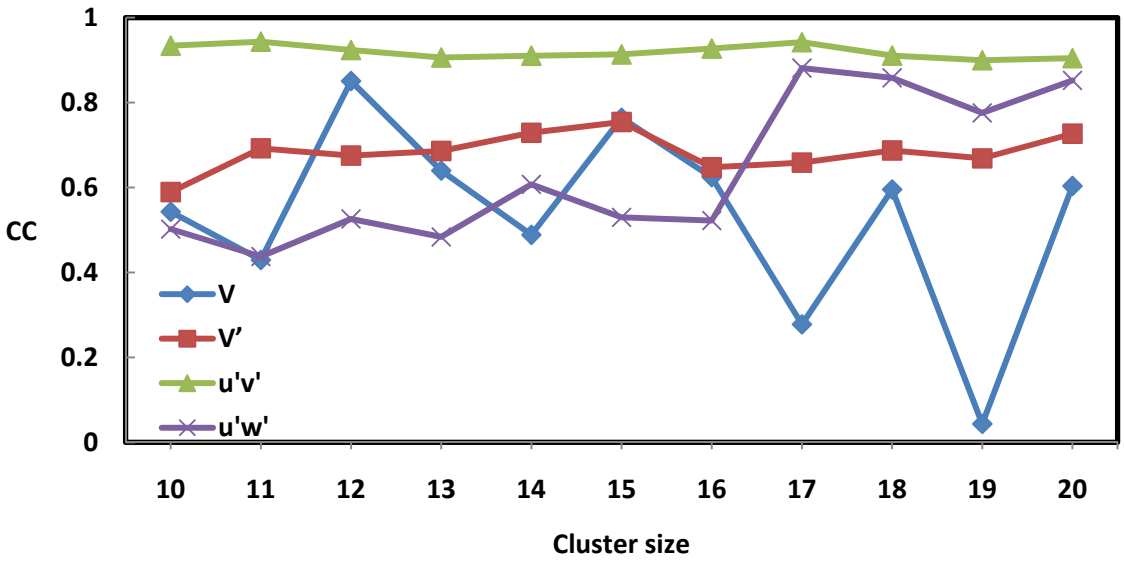

Figure 4.17 Average CC of testing RBF network for $V, v'_{RMS}, \overline{u'v'}$, and $\overline{u'w'}$ at x/H=3, 6, 10 as a function of number of cluster size

CHAPTER 5

RECONSTRUCTION AND PRODUCTION OF TURBULENCE STATISTICS

To ensure a complete successful implementation of the utilized ANN, all profiles are reconstructed by training the network on all profiles except one, and then the excluded profile is compared with the experimental data for the excluded one.

Figure 5.1-5.4 illustrate the comparison between the three networks with the experimental data. The shown profiles are at x/H=1, 3, 5, and 8. The experimental points are shown as markers only, the predictions done by the GFF network are plotted as solid red lines, RBF network data is shown in dashed green lines, and the CANFIS predictions are denoted by dashed-dotted blue lines. Zeros indicate the origin for each profile, and the scale is given by number at the right.

The plots show the most accurate network of each one of the three networks, note that one network only is selected for reconstructing between the Gaussian and Bell models, which is the most appropriate one.

The plots clearly show that GFF network successfully predicts all profiles with high trend, RBF and CANFIS networks, however, show promising prediction on some profiles, but not all, thus, GFF network is recommended to reconstruct turbulence statistics in this model.

The comparison between the experimental data and generated ones using ANN reveals that success of utilizing ANN in reconstructing turbulence statistics profiles, which are shown below in the figures for axial and tangential velocities and their fluctuating components. The results encourage generating extra profiles to enhance the experimental data; this is valuable in implementing

the normalized stream and turbulent kinetic energy (TKE) equations, since the generation of extra profiles decreases the unit step between the profiles. It is also useful in creating surface and contour plots for turbulence statistics, which gives more precise information about the flow inside the combustor.

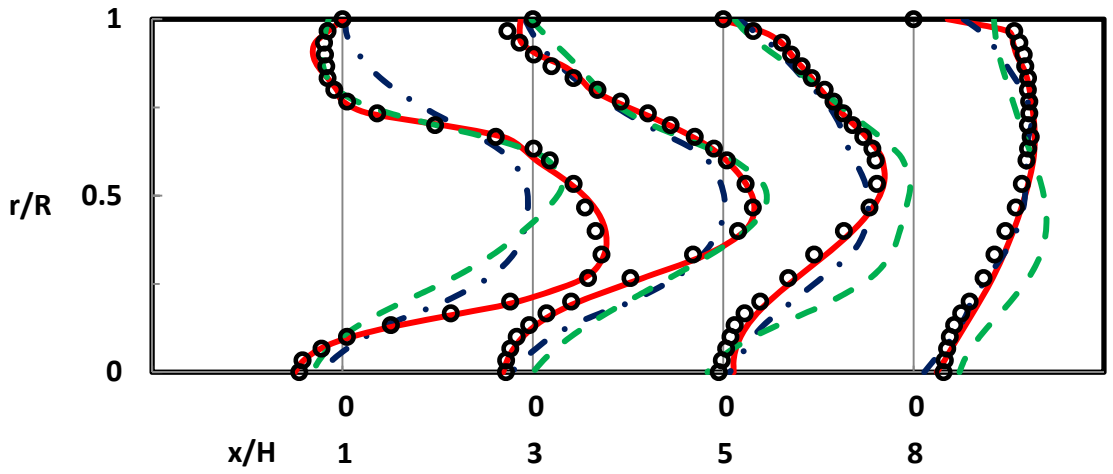

Figure 5.1 Evolution of U/U_o profiles at x/H=1, 3, 5, and 8 for experimental and neural networks predictions

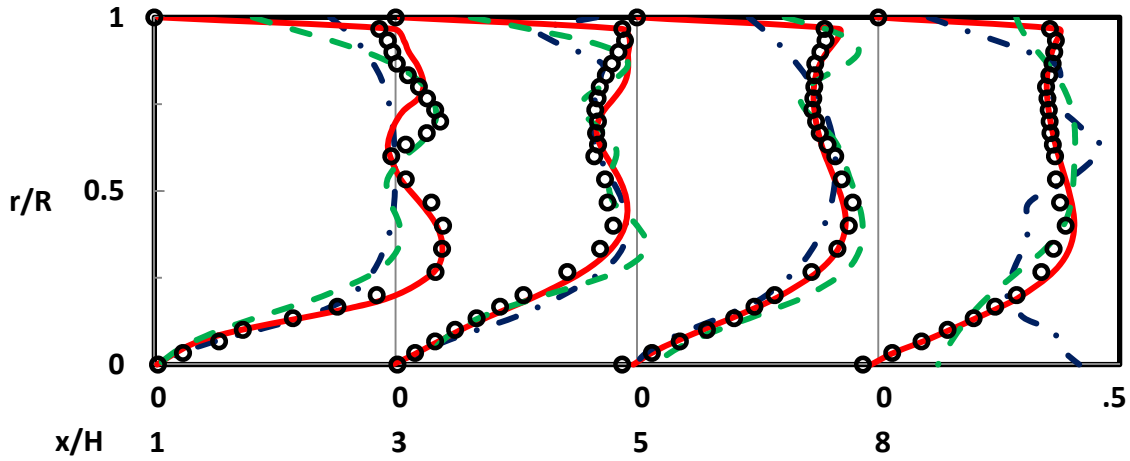

Figure 5.2 Evolution of W/U_o at x/H=1, 3, 5, and 8 profiles for experimental and neural networks predictions

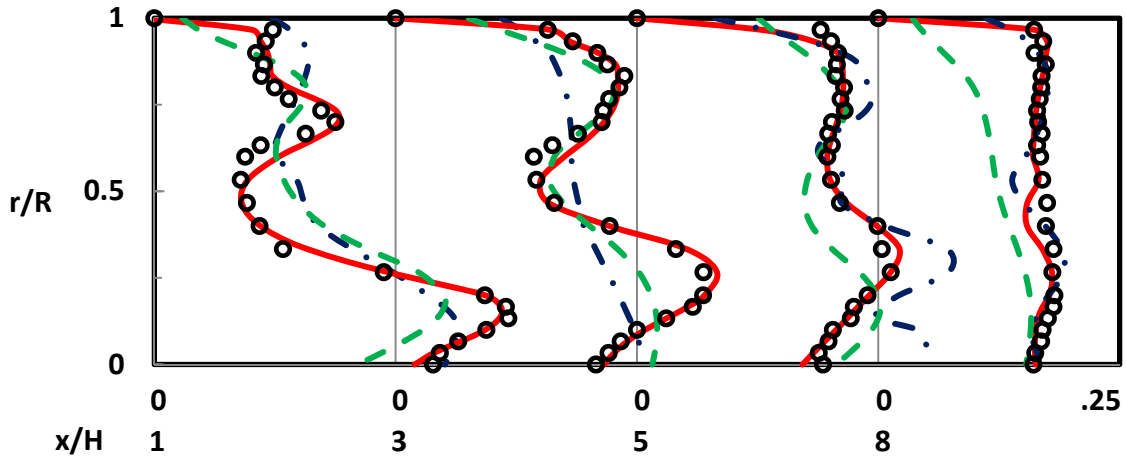

Figure 5.3 Evolution of u'_{RMS}/U_o profiles for experimental and neural networks predictions

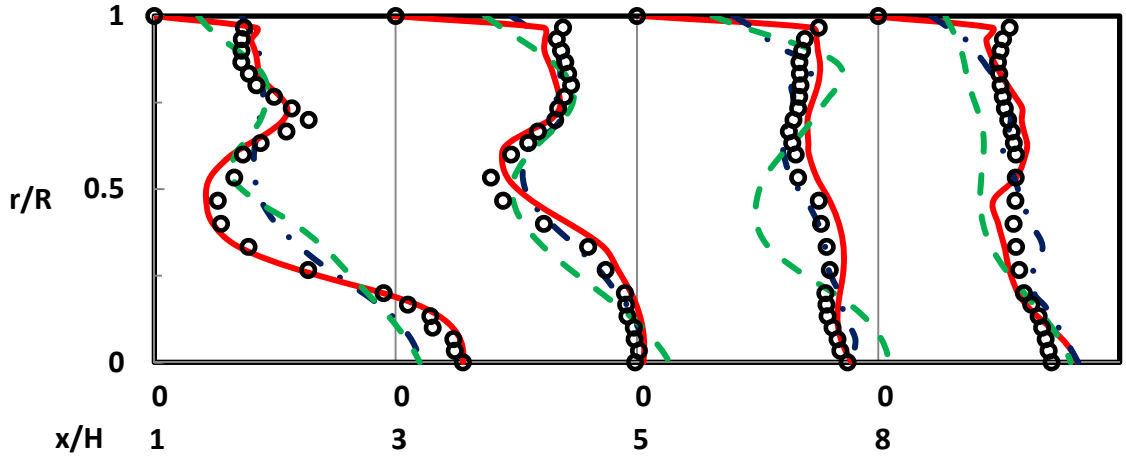

Figure 5.4 Evolution of w'_{RMS}/U_o profiles for experimental and neural networks predictions

Table 5.1 summarizes the best network, which will be used in reconstructing and generating turbulence statistics, GFF network succeeds to predict most of the components, however, $\overline{u'^2v'}$ and $\overline{u'^2w'}$ are predicted more precisely using CANFIS network. These results help in utilizing specific ANN structures to be used in predicting any turbulence component, since successful predictions occur at small range of neurons (i.e. 9-19 neurons), also, if the desired component is one of the studied ones in this thesis, the mentioned ANN structure can be used successfully, regardless the amount of data and the swirl number of the flow.

Table 5.1 Best network and CC values of turbulence statistics at x/H=6 for 0.5 swirler

Component	Best Network	CC
$\boldsymbol{U}$	GFF (19 Neurons)	0.995841
$\boldsymbol{V}$	GFF (11 Neurons)	0.98113
$\boldsymbol{W}$	GFF (18 Neurons)	0.997619
$\boldsymbol{u'_{RMS}}$	GFF (18 Neurons)	0.985182
$\boldsymbol{v'_{RMS}}$	GFF (18 Neurons)	0.992505
$\boldsymbol{w'_{RMS}}$	GFF (18 Neurons)	0.997619
$\boldsymbol{\overline{u'v'}}$	GFF (15 Neurons)	0.987104
$\boldsymbol{\overline{u'w'}}$	GFF (13 Neurons)	0.910396
$\boldsymbol{\overline{u'^3}}$	GFF (14 Neurons)	0.928483
$\boldsymbol{\overline{v'^3}}$	GFF (13 Neurons)	0.834668
$\boldsymbol{\overline{w'^3}}$	GFF (9 Neurons)	0.850757
$\boldsymbol{\overline{u'^2v'}}$	CANFIS (6 MFs)	0.714227
$\boldsymbol{\overline{u'v'^2}}$	GFF (14 Neurons)	0.930666
$\boldsymbol{\overline{u'^2w'}}$	CANFIS (4 MFs)	0.611352
$\boldsymbol{\overline{u'w'^2}}$	GFF (13 Neurons)	0.816574

Figure 5.5 and

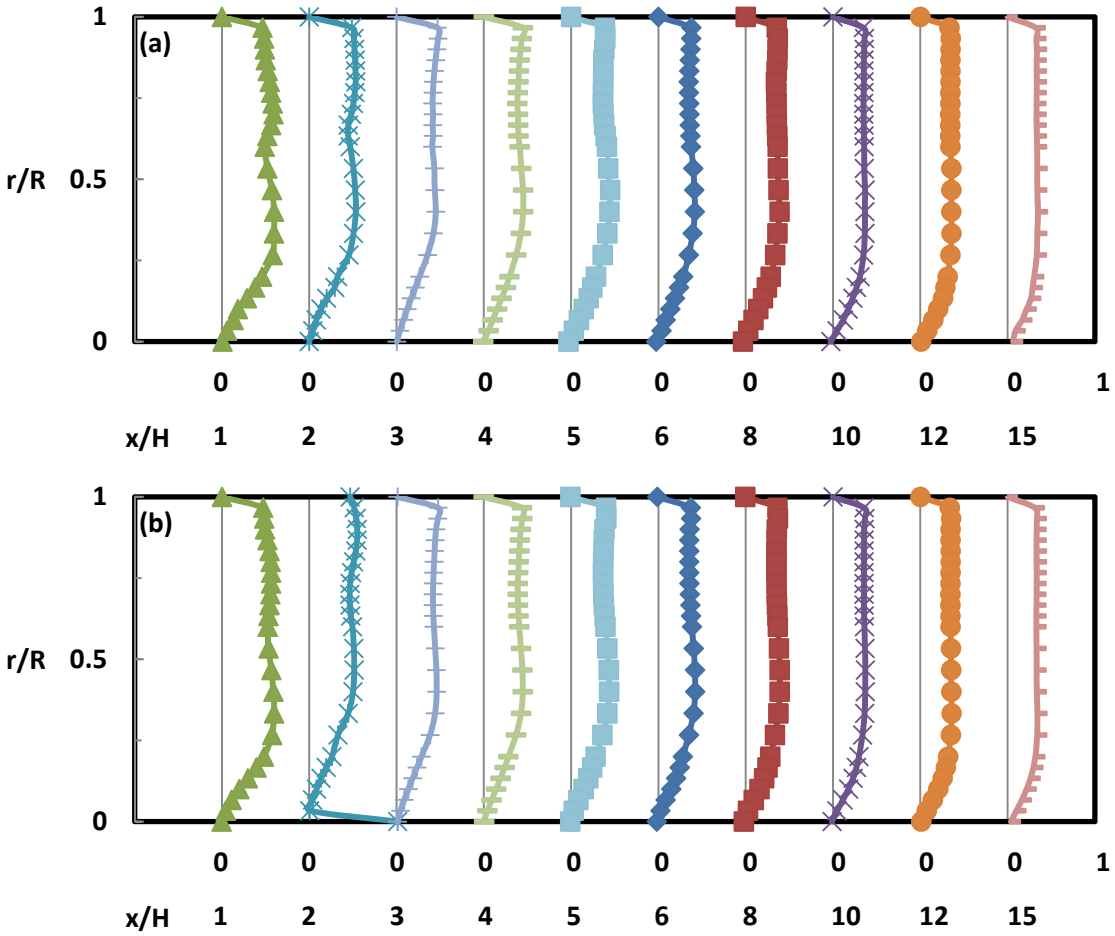

figure 5.6 show the experimental and predicted axial and tangential velocity profiles for 0.5 swirler, at $x/H = 1, 2, 3, 4, 5, 6, 8, 10, 12,$ and 15, respectively, using GFF network with 19 and 18 neurons, respectively. Zero values of axial velocity represent the reverse flow boundaries. ANN successfully predicts the axial and tangential component as the expected behaviors of them are present. Since the swirler is responsible for shortening the corner recirculation zone and creating central toroidal recirculation zone, the maximum axial velocity at each profile is located approximately halfway between the corner and the central recirculation region. ANN predictions also preserve the fact that axial velocity component is greater than tangential component, as can be seen from the scale of the plots.

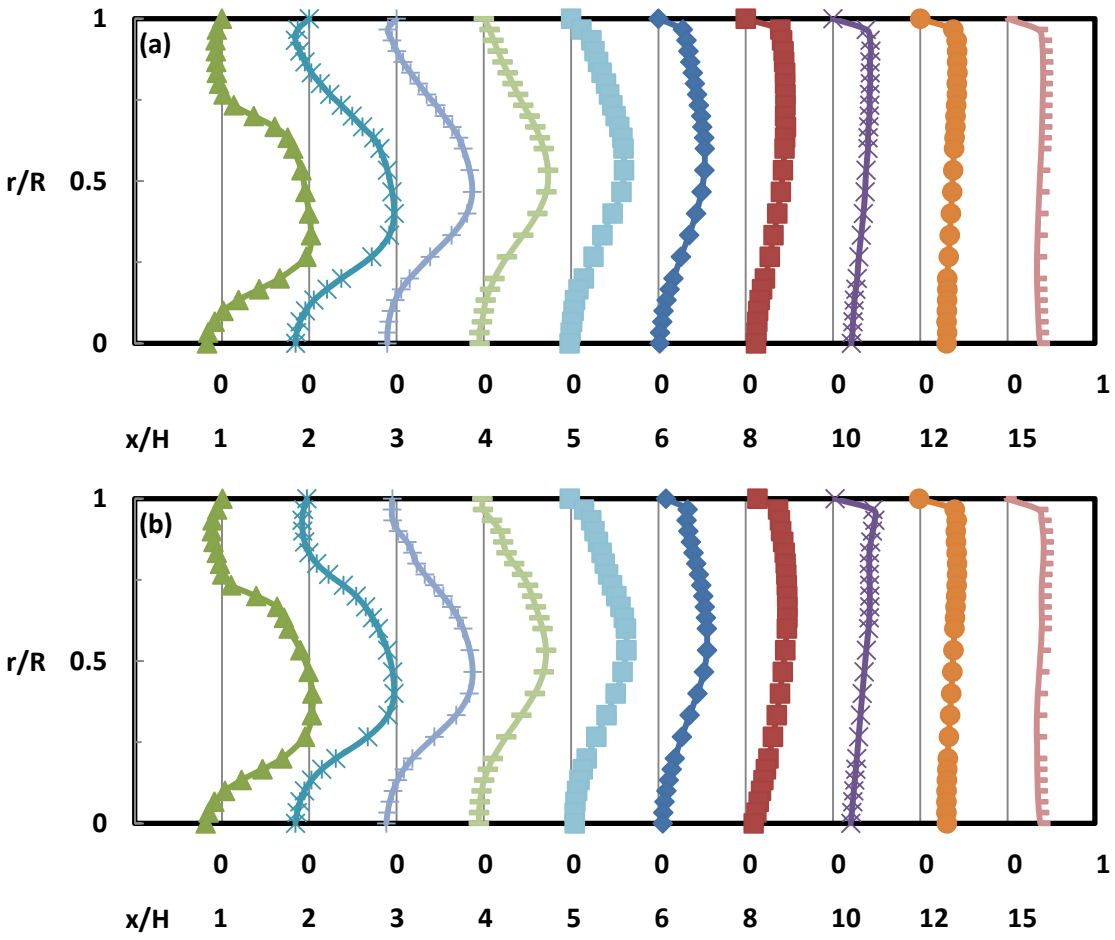

Figure 5.5 Evolution of U/U_o at 0.5 swirler, Zeros indicate the origin for each profile, and the Scale is given by number at the end right. (a)Experimental (b)ANN

In

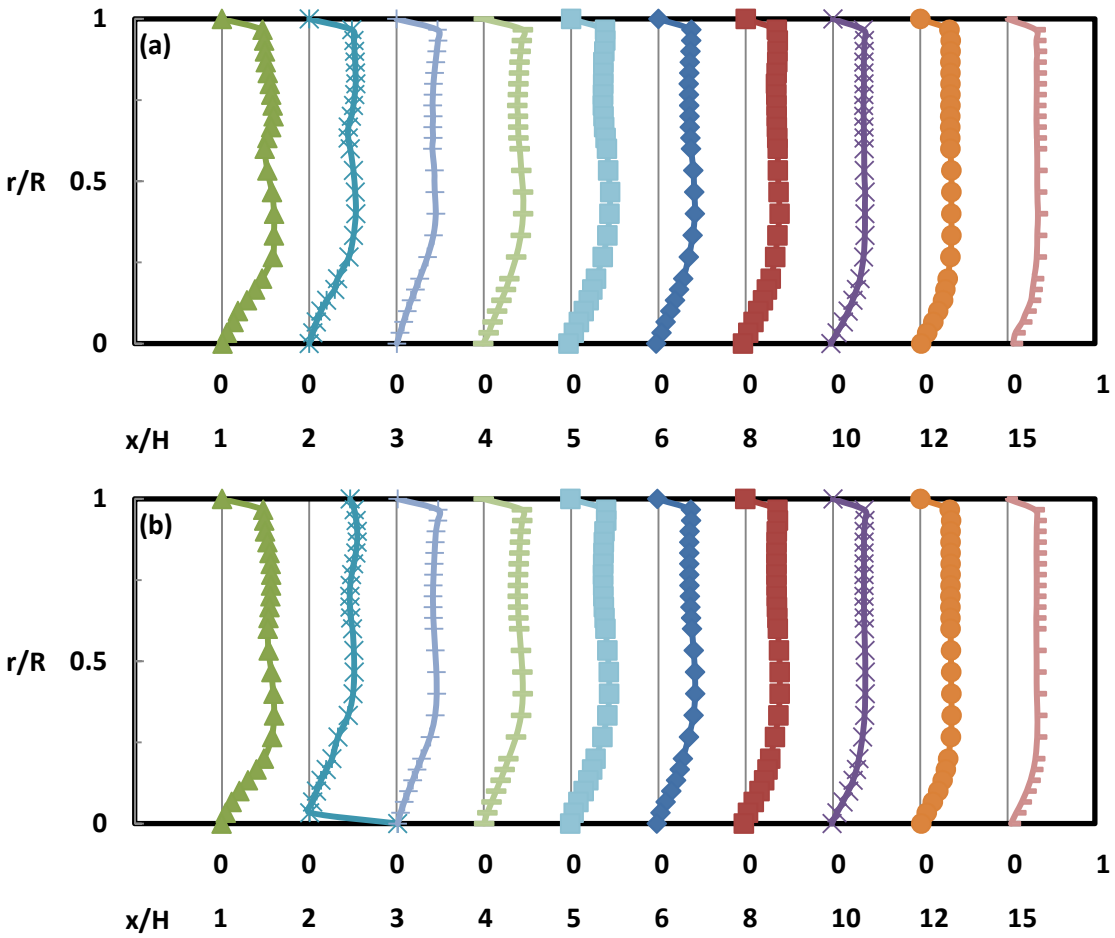

figure 5.6, the flow velocity characteristics of tangential velocity component are similar to free vortex flow. At the centerline, the flow behavior is akin to forced vortex, while the magnitude of tangential velocity is almost constant far downstream and away from the centerline. The predictions by ANN are successfully achieved, since the distribution of the tangential velocity is asymmetric, as anticipated.

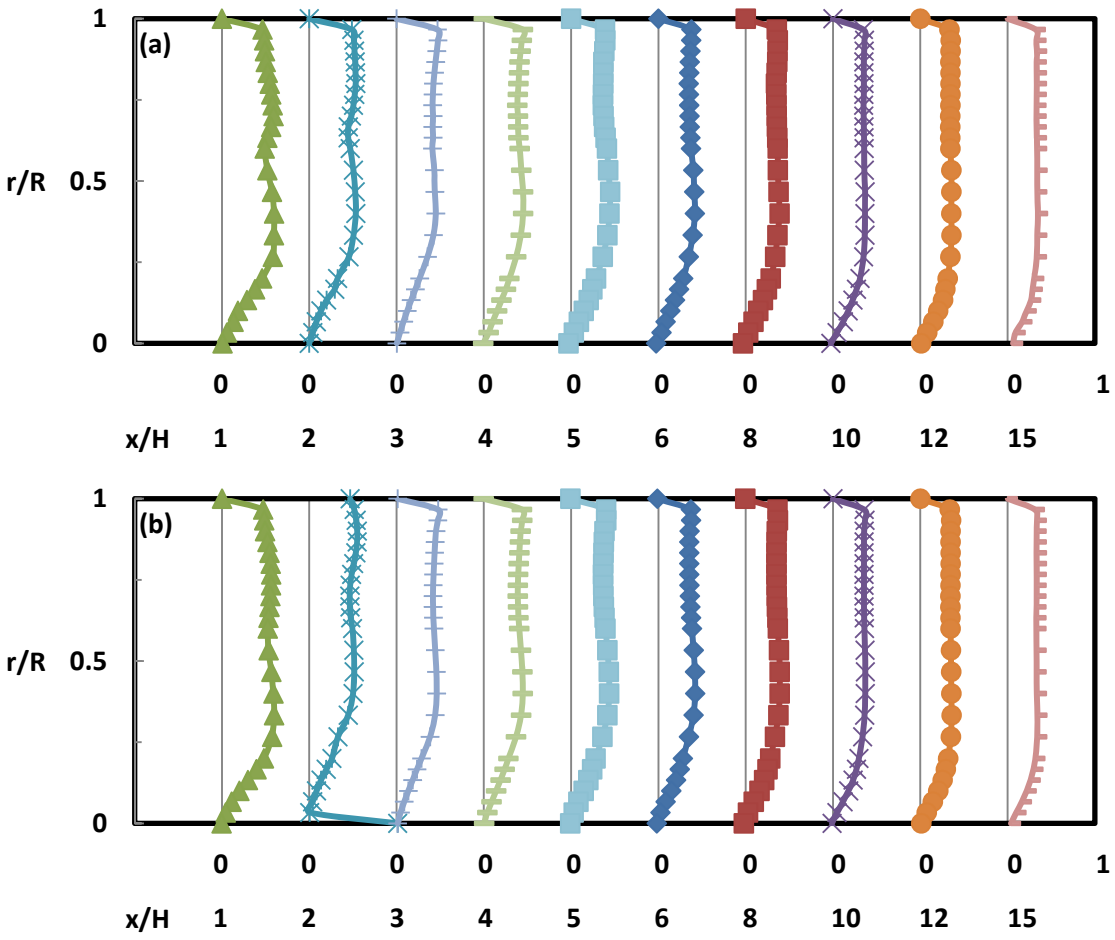

Figure 5.6 Evolution of W/U_o at 0.5 swirler, Zeros indicate the origin for each profile, and the Scale is given by number at the end right. (a)Experimental (b)ANN

Figure 5.7 shows the evolution of radial velocity component, (a) represents the experimental data and (b) represents the predicted profiles, the plotted profiles are for 0.5 swirler and at the near filed of the combustor (i.e. $x/H = 1, 2, 3, 4, 5,$ and 6). Predictions far downstream the combustor are not achieved because the radial velocity values are almost constant and very small compared to upstream profiles. The used ANN structure is also GFF network with 11 neurons. Though the CC values obtained from testing ANN predictions are not as high as in axial and tangential velocities, ANN still able to show the inward flow direction at the corner recirculation zone due to the flow reversal, since the values obtained there are negative. Also ANN predictions at the

halfway between the centerline and corner regions are similar to the experimental ones, where maximum values obtained there. Note that the location of the maximum radial velocity comes closer to the corner as moving far downstream.

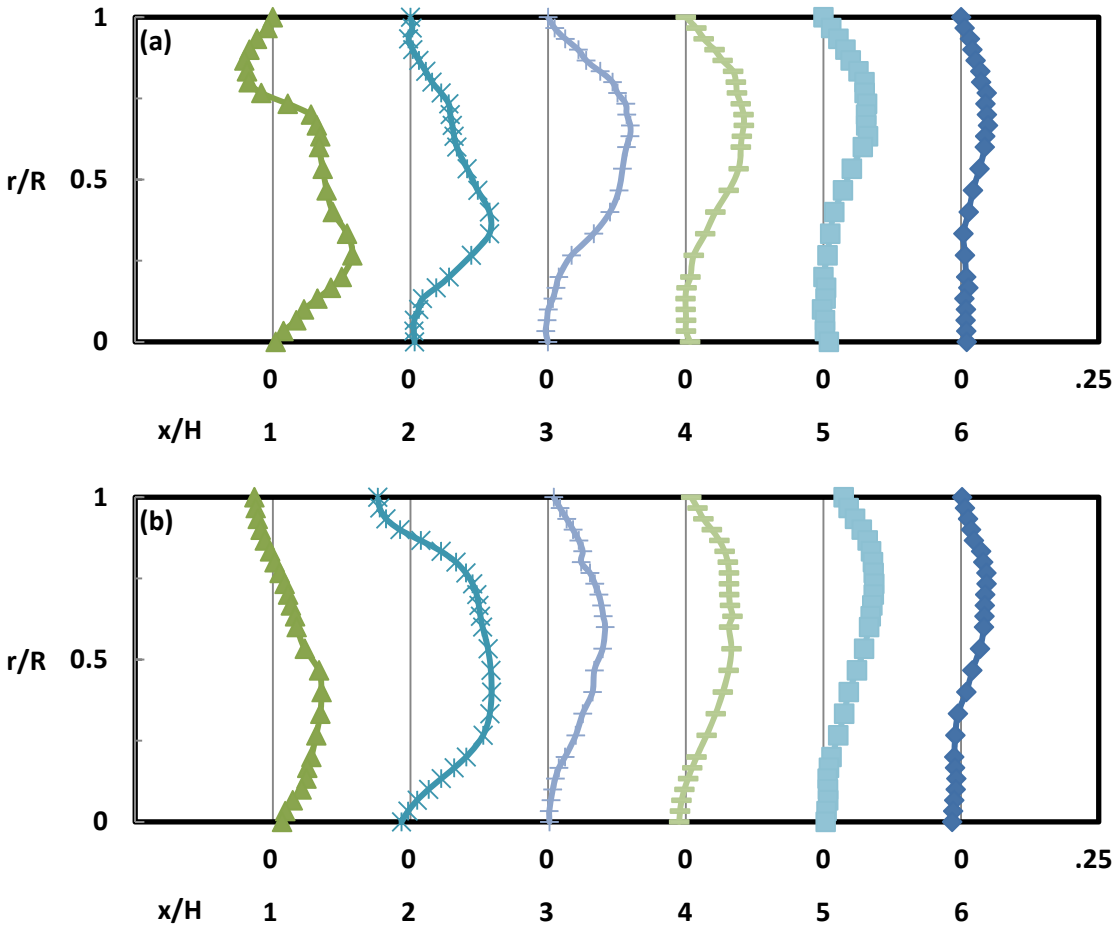

Figure 5.7 Evolution of V/U_o at 0.5 swirler, Zeros indicate the origin for each profile, and the Scale is given by number at the end right. (a)Experimental (b)ANN

Figure 5.8-5.10 show the experimental and ANN predictions of the fluctuating velocity components in the axial, tangential, and direction, respectively, for 0.5 swirler at x/H= 1, 2, 3, 4, 5, and 6. All predictions are similar to the experimental profiles as shown below.

All normal stresses are predicted using GFF network with 18 neurons GFF network successfully predicts all normal stresses profiles with the same network structure.

For all normal stresses, there are two peaks characterized the swirling flow around the inner and outer shear layers, the larger peak is located near the central toroidal recirculation zone, while the smaller one occurs near the corner recirculation zone.

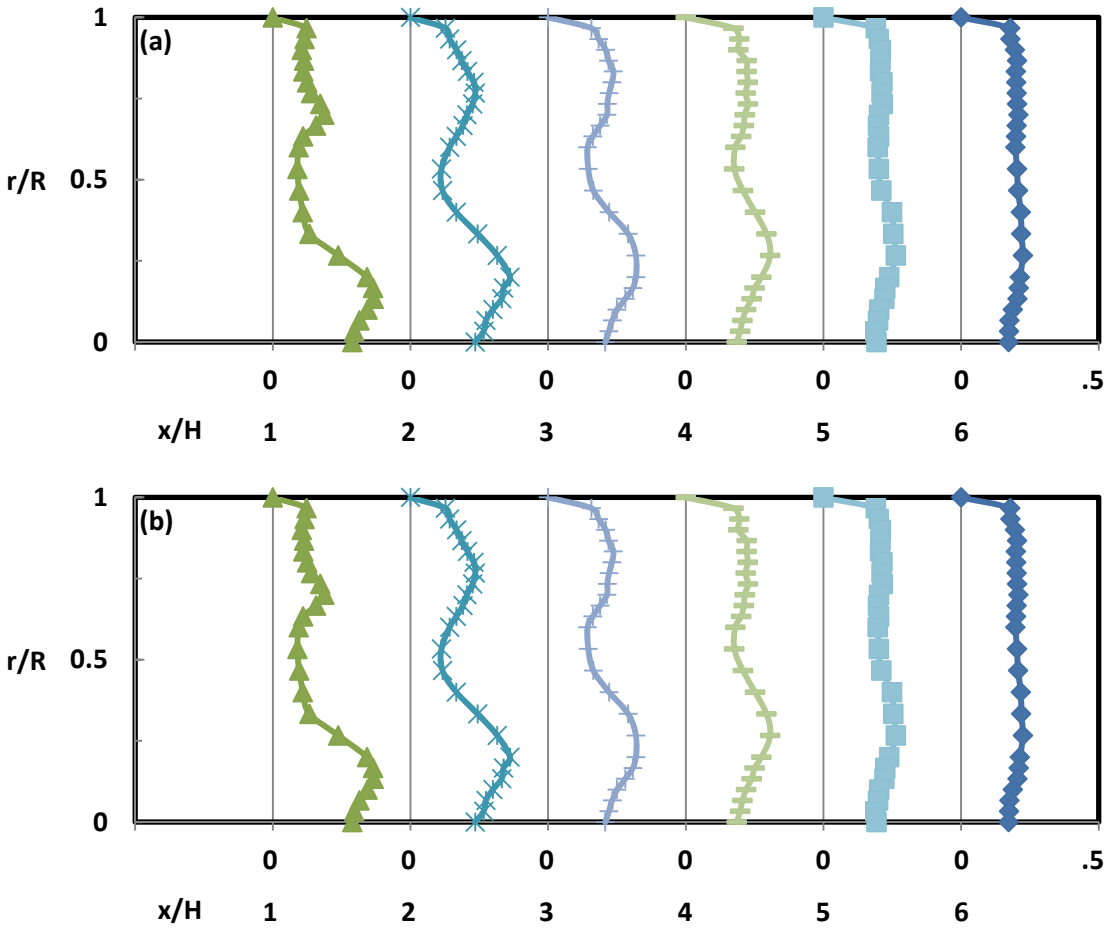

Figure 5.8 Evolution of u'_{RMS}/U_o at 0.5 swirler, Zeros indicate the origin for each profile, and the Scale is given by number at the end right. (a)Experimental (b)ANN

Note that all values of normal stress profiles are positive and always zero at the corners. Also, the peak value of axial fluctuating component is observed

to move towards the combustor wall as it decays in strength and growth in size, indicating a progressive development of the outer shear layer. Moreover, turbulence activity is more concentrated at the central shear layer and the centers of the maximum values for the two regions where the peak values occurred are observed to be approximately at $x/H = 3$.

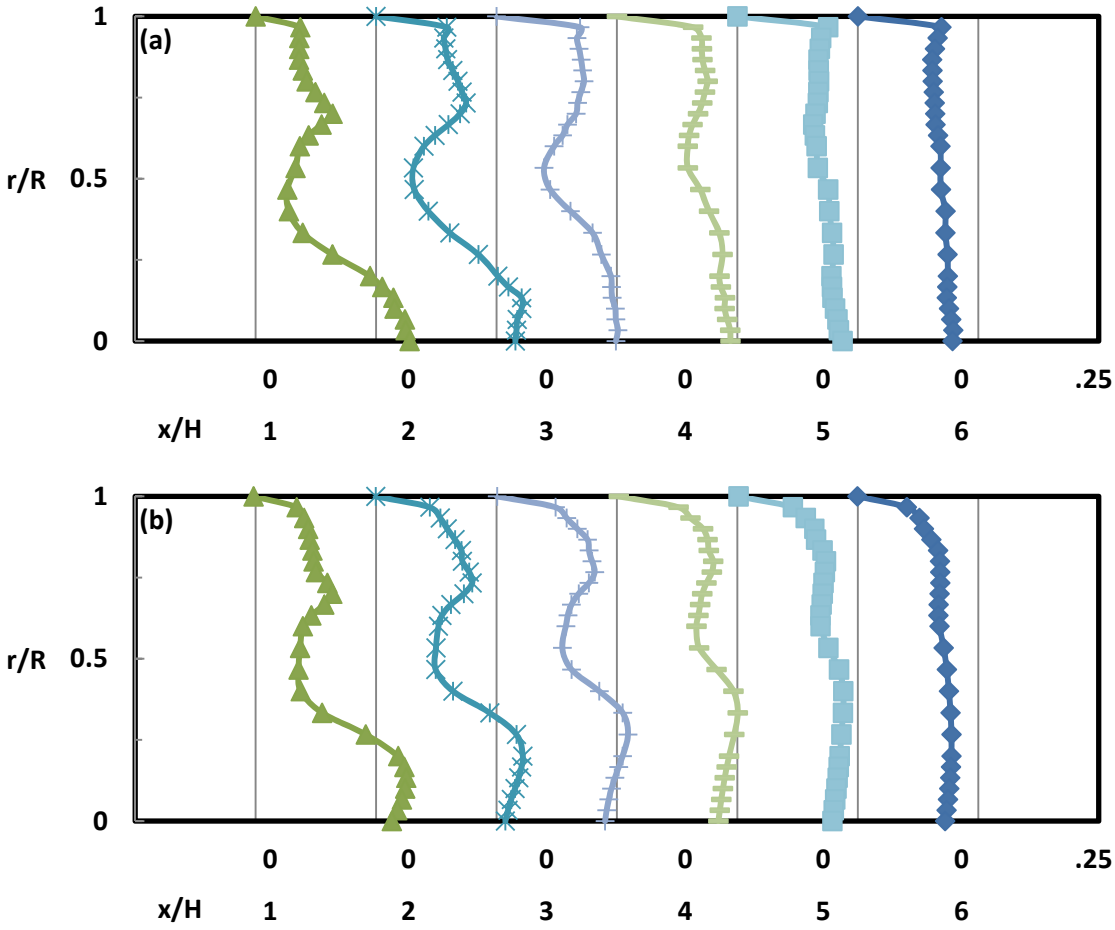

Figure 5.9 Evolution of w'_{RMS}/U_o at 0.5 swirler, Zeros indicate the origin for each profile, and the Scale is given by number at the end right. (a)Experimental (b)ANN

As discussed earlier, the characteristics of the tangential and radial fluctuating components are similar to the axial ones. However, the flow near the core is not completely recovered due to the existence of central toroidal recirculation zone as indicated by relatively higher values at each axial location.

Also, the values of tangential and radial fluctuating velocity components are smaller than axial ones, as indicated by the scale of the figures.

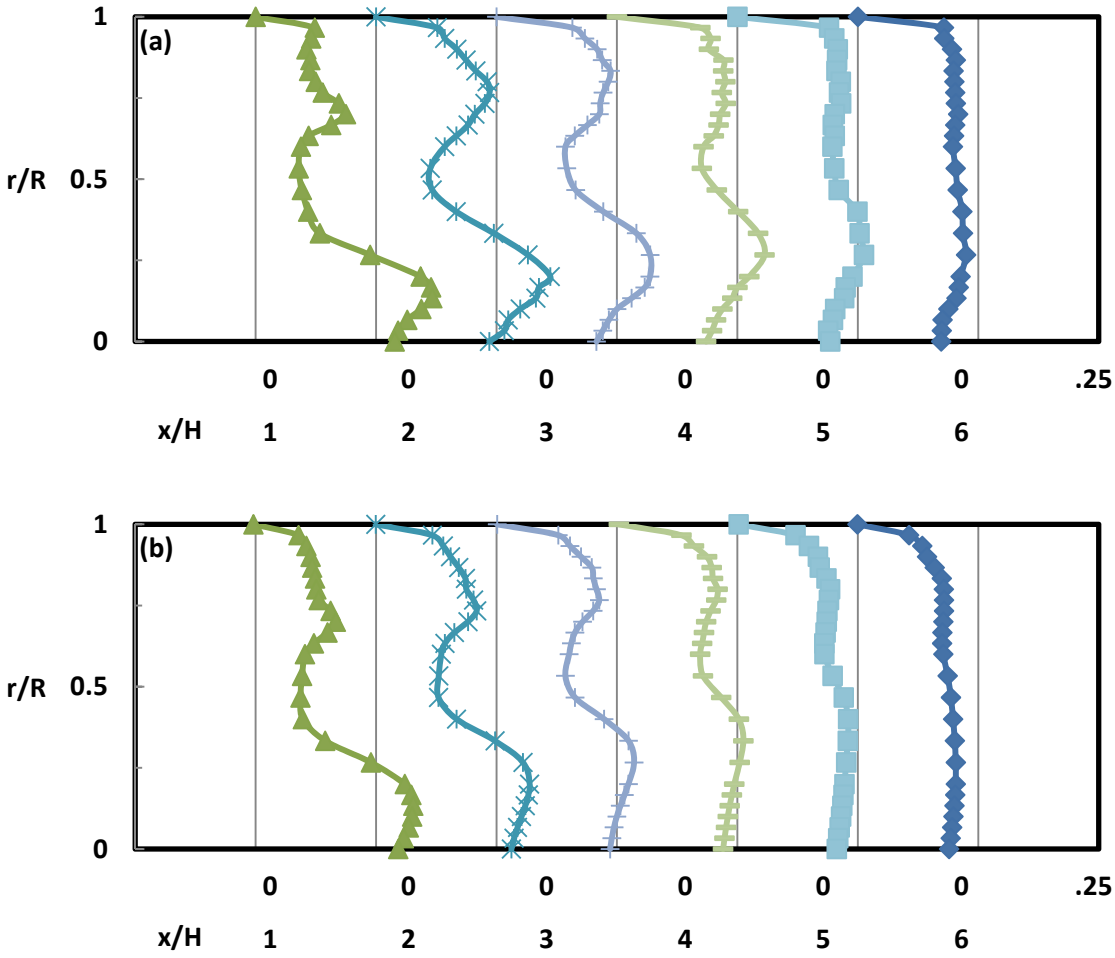

Figure 5.10 Evolution of v'_{RMS}/U_o at 0.5 swirler, Zeros indicate the origin for each profile, and the Scale is given by number at the end right. (a)Experimental (b)ANN

Shear stresses profiles are presented in figure 5.11 and figure 5.12 for both experimental and ANN at $x/H = 1, 2, 3, 4, 5,$ and 6 for 0.5 swirler. The shear stress in UV plane is shown in figure 5.11, while figure 5.12 shows the shear stress profiles in UW plane.

The Analogous of utilizing GFF network to predict shear stresses indicates a successful implementation of both Reynolds shear stresses. However, the GFF architecture used to predict the shear stress in UV plane is different

than the one used to reconstruct shear stress profile in UW plane. The number of processing elements used in the network used for shear stress in UV plane is 15, while 13 neurons are used to reconstruct shear stress profiles in UW plane.

Unlike normal stresses profiles, shear stresses can have negative and positive values depending on their location. For both shear stresses, the negative peaks occur at the shear layer of the centerline toroidal recirculation zone, which indicate reverse flow at these locations. The maximum positive peaks of the shear stress in UV plane are located at the shear layer of the corner recirculation zone, while the values of shear stresses in UW plane at the same location are not necessarily positive.

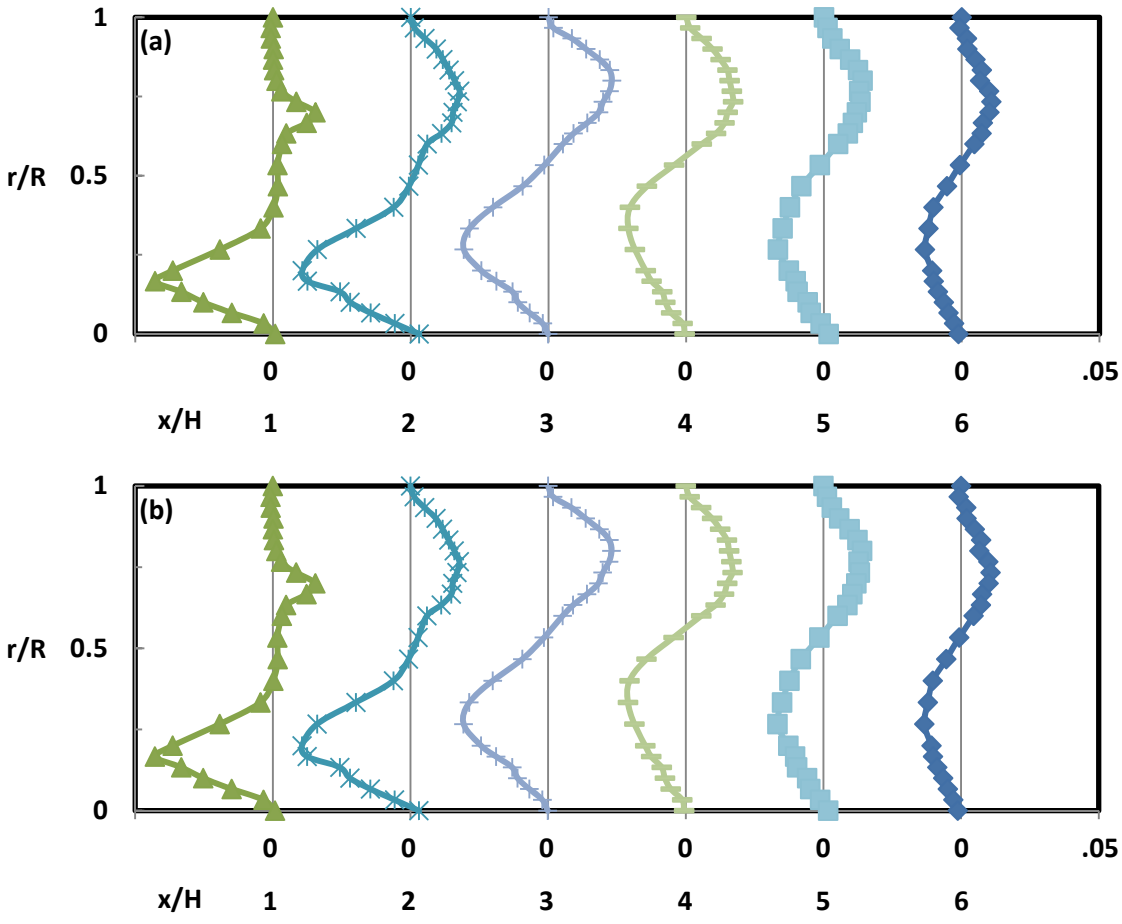

Figure 5.11 Evolution of $\overline{u'v'}/U_o^2$ at 0.5 swirler, Zeros indicate the origin for each profile, and the Scale is given by number at the end right. (a)Experimental (b)ANN

The shear layer is thin near the dump and then expands to fill the entire combustor as moving further towards the far field, this is not clearly shown here, since the far field profiles are not presented in the figures. The high Reynolds shear stress values occur at region of maximum velocity gradients, which confirms the observation that swirl is responsible for increasing the values of normal and shear stresses by an approximately an order of magnitude.

Though the trend of ANN predictions for the first profile (i.e. $x/H = 1$) of the shear stress in the UV plane at the layer located near the corner recirculation zone is not precisely similar to the experimental one, ANN successfully captured the peak at that location.

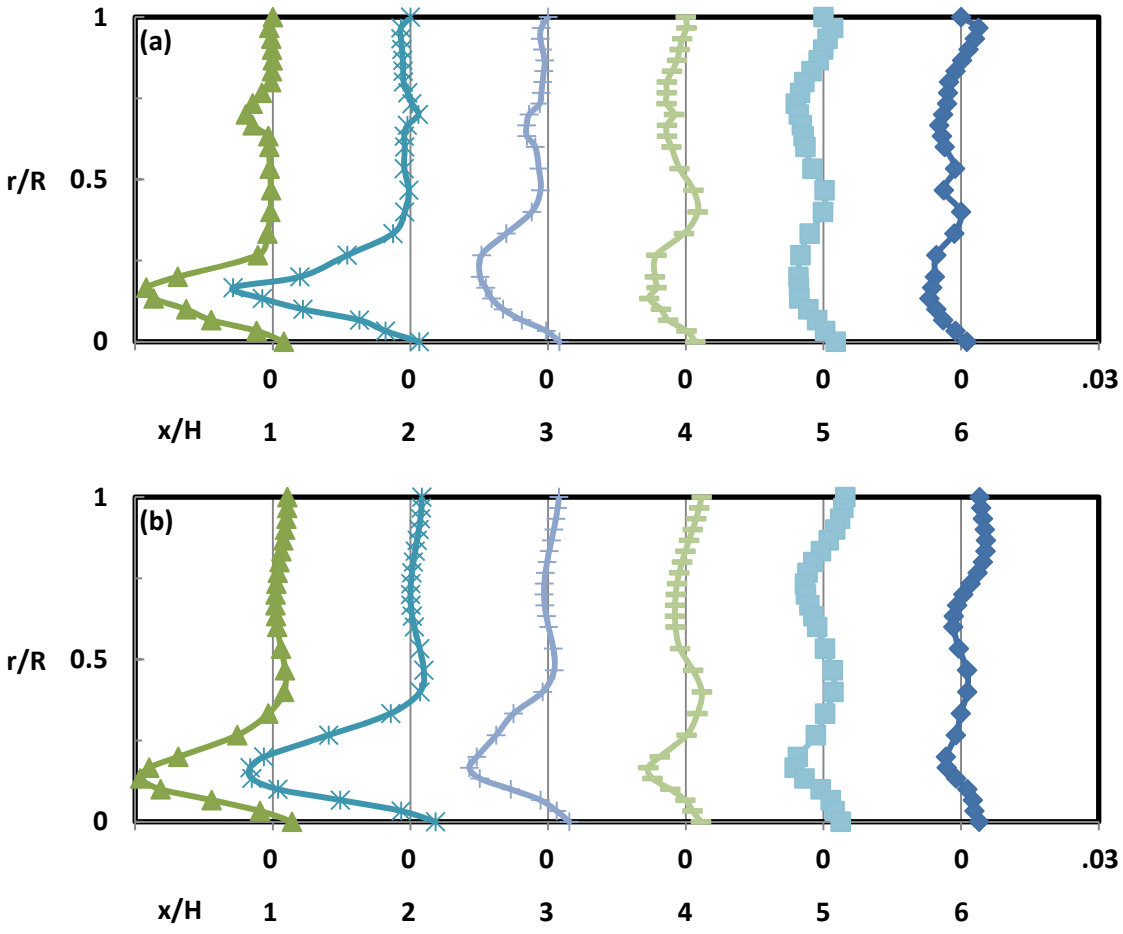

Figure 5.12 Evolution of $\overline{u'w'}/U_o^2$ at 0.5 swirler, Zeros indicate the origin for each profile, and the Scale is given by number at the end right. (a)Experimental (b)ANN

On the contrary, the peaks of the first two profiles (i.e. x/H =1 and 2) for the shear stress in UW plane in the ANN data are smaller than the ones in the experimental data. The trends of these profiles for ANN, however, are similar to the ones the experimental data. Also, ANN could not predict the change of the behavior of the third profile (i.e. x/H =3) just below the wall, but the values are negative for both, which is important to detect the reverse flow. This also occurs at the last profile (i.e. x/H =6) in the halfway between the corner and the centerline of the combustor.

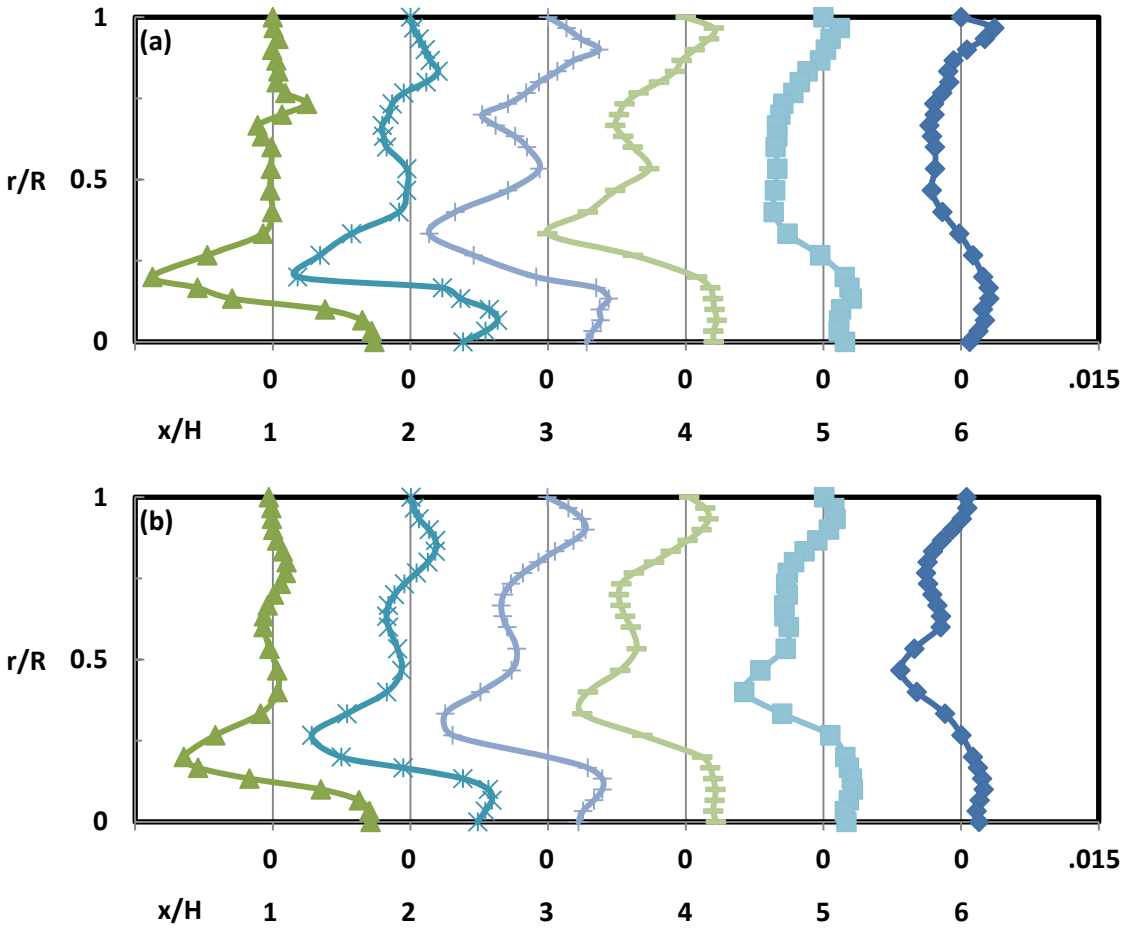

Figure 5.13 Evolution of $\overline{u'^3}/U_0^3$ at 0.5 swirler, Zeros indicate the origin for each profile, and the Scale is given by number at the end right. (a)Experimental (b)ANN

Figure 5.13 shows the experimental and ANN near field triple velocity component u'^3. Again, GFF network with 14 neurons is the most accurate

network that predicts $\overline{u'^3}$. ANN successfully reconstructs all main features for all profiles, except predicting the peak negative value of the first and fourth profiles, these peaks are located approximately at $r/R =$ 0.25 and 0.35, respectively. Note that all profiles contain negative peak located between the halfway between the wall and the centerline and the centerline, however, the peaks locations change as moving further from the dump. Also ANN managed to preserve zero values at the wall for all profiles except at x/H =6 where a positive value is predicted. ANN also predicted the sudden positive changes of values located between r/R =0.75 and 1, the location of these values rise as moving away from the dump.

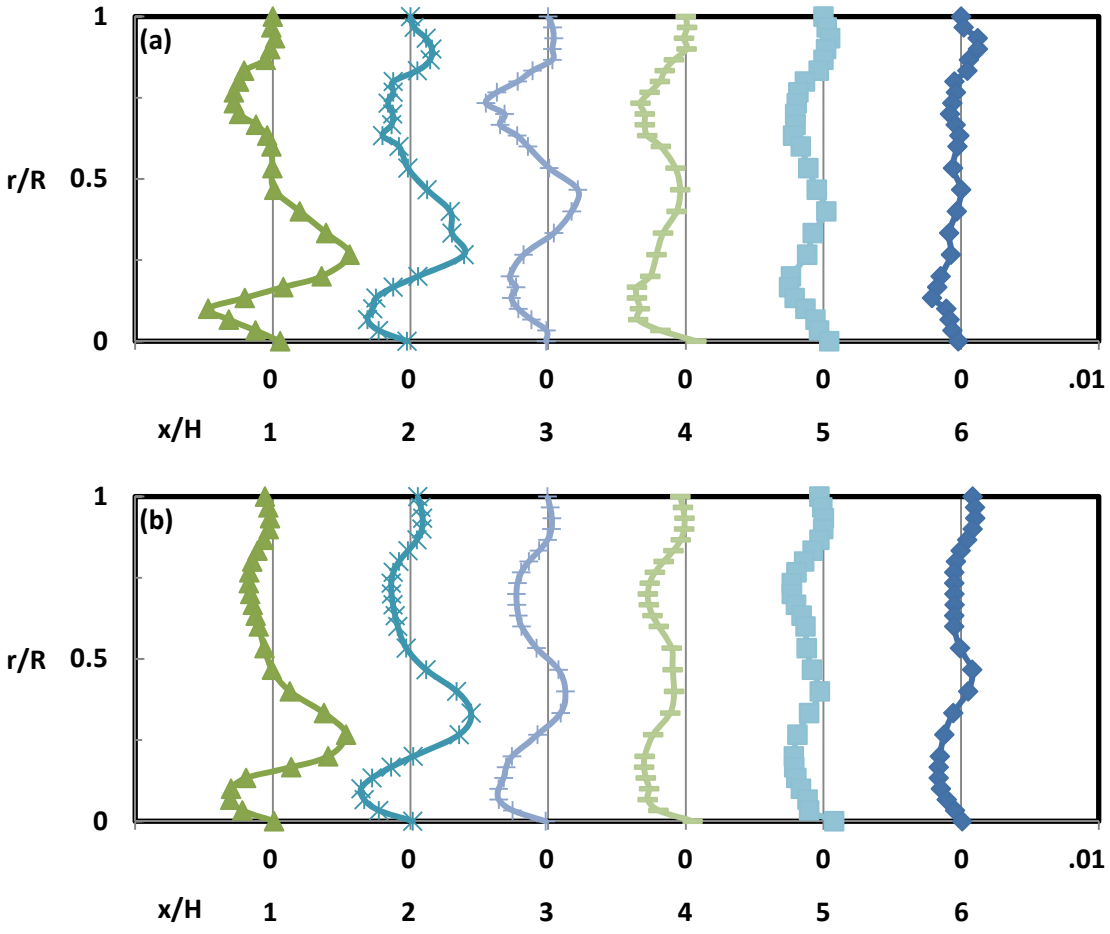

Figure 5.14 Evolution of $\overline{v'^3}/U_0^3$ at 0.5 swirler, Zeros indicate the origin for each profile, and the Scale is given by number at the end right. (a)Experimental (b)ANN

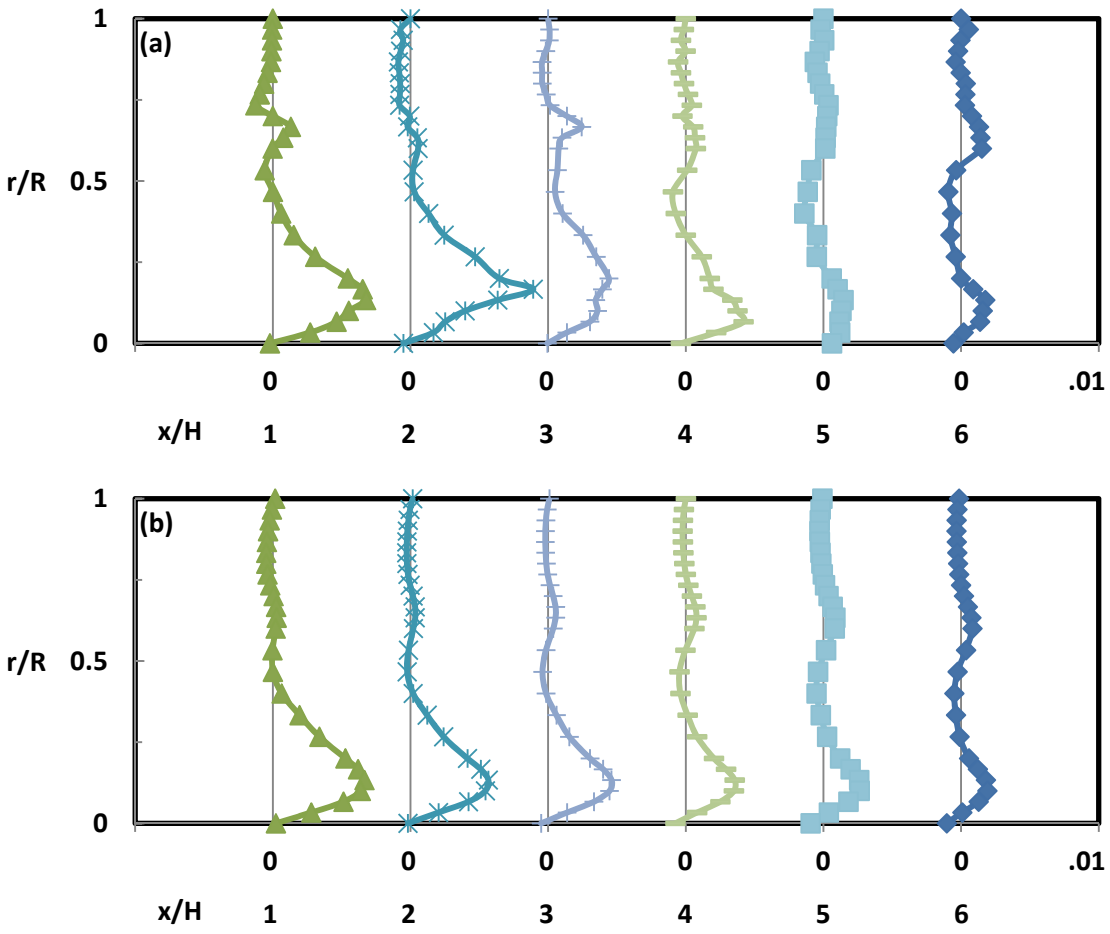

Figure 5.15 Evolution of $\overline{w'^3}/U_0^3$ at 0.5 swirler, Zeros indicate the origin for each profile, and the Scale is given by number at the end right. (a)Experimental (b)ANN

The results of predicting triple velocity components $\overline{v'^3}$ and $\overline{w'^3}$ are shown in figures 5.14, 5.15, respectively. The used ANN network is also GFF network with 13 neurons for $\overline{v'^3}$ and 9 neurons for $\overline{w'^3}$. All flow characteristics of $\overline{v'^3}$ are predicted successfully except the reverse flow located at the layer near the corner.

Even though ANN predicted non existing peak at x/H=3 for $\overline{w'^3}$, most features are predicted successfully, like the reverse flows at x/H =1 and 2.

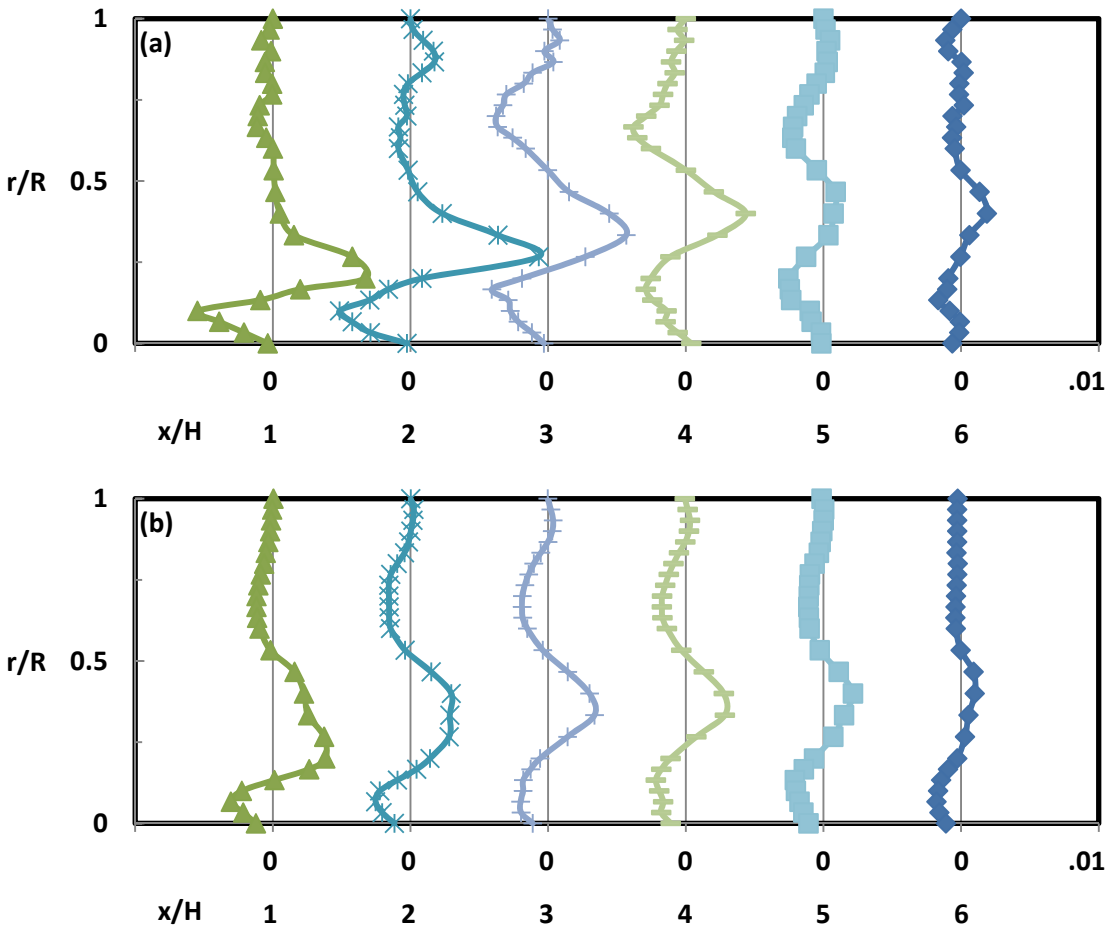

Figure 5.16 Evolution of $\overline{\overline{u'^2v'}}/U_0^3$ at 0.5 swirler, Zeros indicate the origin for each profile, and the Scale is given by number at the end right. (a)Experimental (b)ANN

Figure 5.16-5.19 present triple velocity correlations $\overline{u'^2v'}, \overline{u'v'^2}, \overline{u'^2w'}, \overline{u'w'^2}$, respectively.

The best network in reconstructing $\overline{u'^2v'}$ is CANFIS network with 4 membership functions, unfortunately, ANN is unable to locate most peaks in through all profiles; however, ANN still can be used to situate the positions of reverse flows.

For $\overline{u'v'^2}$, the most accurate network is GFF network with 14 neurons, the CC values of testing the network are more than 0.85 for all profile. All negative values are predicted correctly as well as all peaks which are located

successfully, however, small variation in the value of peaks at first two profiles.

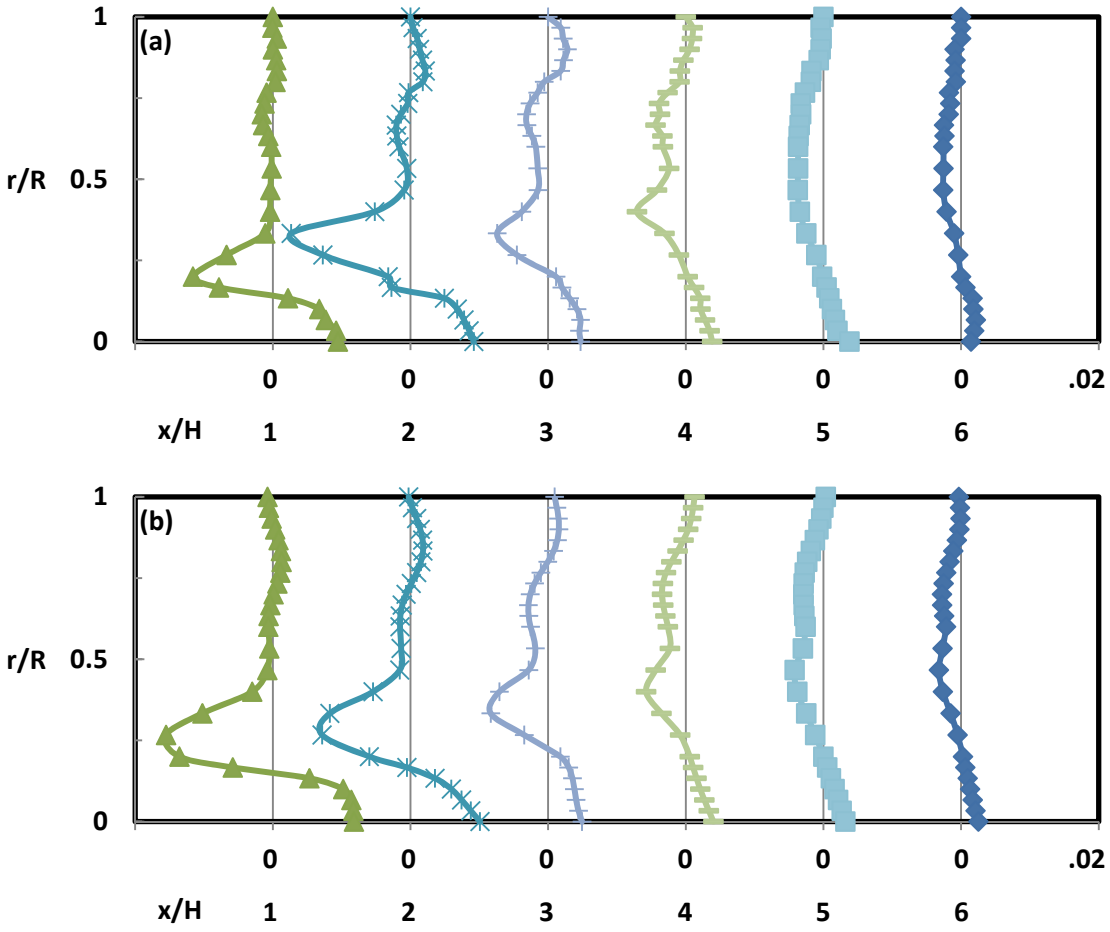

Figure 5.17 Evolution of $\overline{u'v'^2}/U_0^3$ at 0.5 swirler, Zeros indicate the origin for each profile, and the Scale is given by number at the end right. (a)Experimental (b)ANN

The used network in reconstructing $\overline{u'^2w'}$ is CANFIS with 4 membership functions. The obtained predictions are not accurate because of the sudden change in the behavior of the profiles.

Nevertheless, since the contribution of $\overline{u'^2w'}$ in TKE equation is very small, ANN is still used to generate extra data.

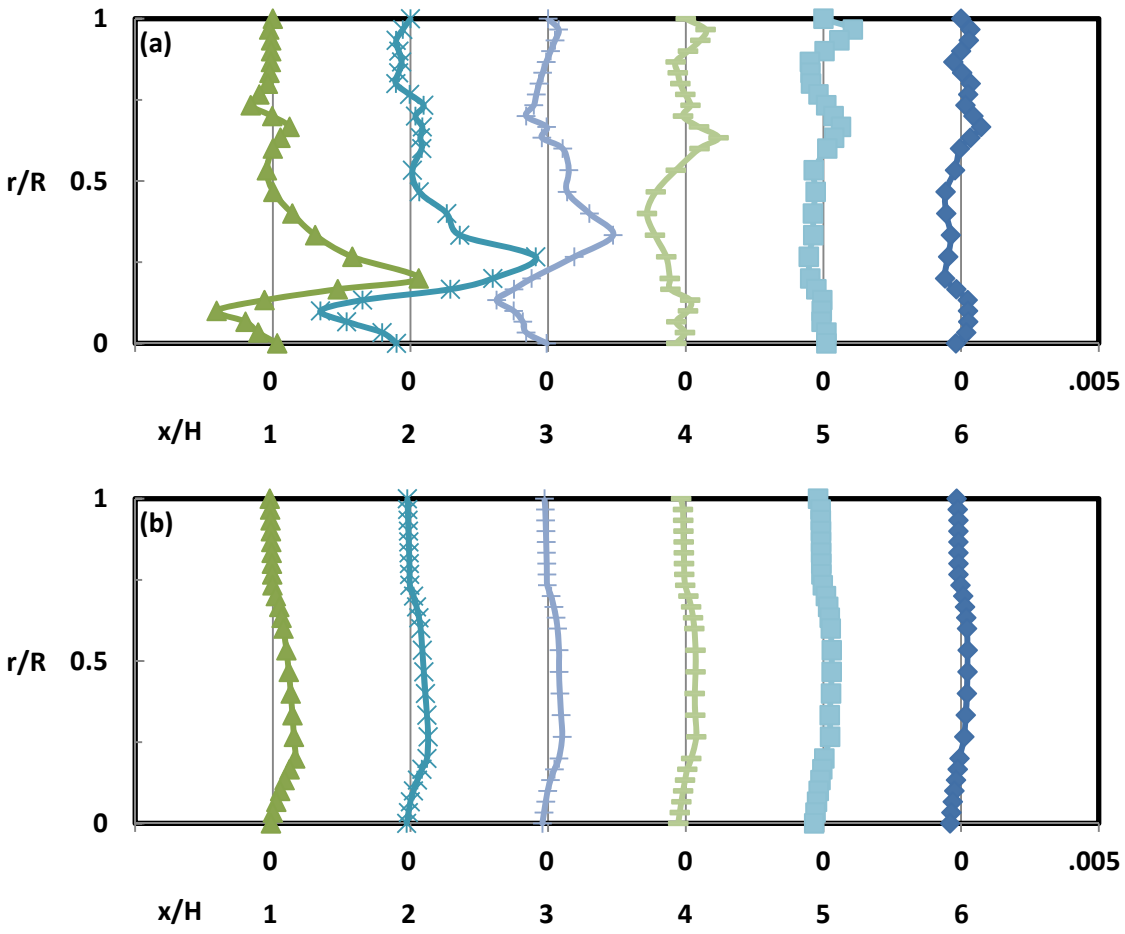

Figure 5.18 Evolution of $\overline{u'^2w'}/U_o^3$ at 0.5 swirler, Zeros indicate the origin for each profile, and the Scale is given by number at the end right. (a)Experimental (b)ANN

Figure 5.19 shows the evolution of experimental and ANN profiles of $\overline{u'w'^2}$, GFF network with 13 processing elements is used to reconstruct the corresponding profiles.

Most flow characteristics are predicted accurately, including peaks and negative values. However, all zero values at the wall are also predicted successfully except at x/H =3,

In general, all triple velocity products are asymmetric about the centerline of the shear layer. They peak to different values on both sides of the

shear layer and their values diminish at the edge of the shear layer. Note that these peaks are prominent before the reattachment point of the near filed.

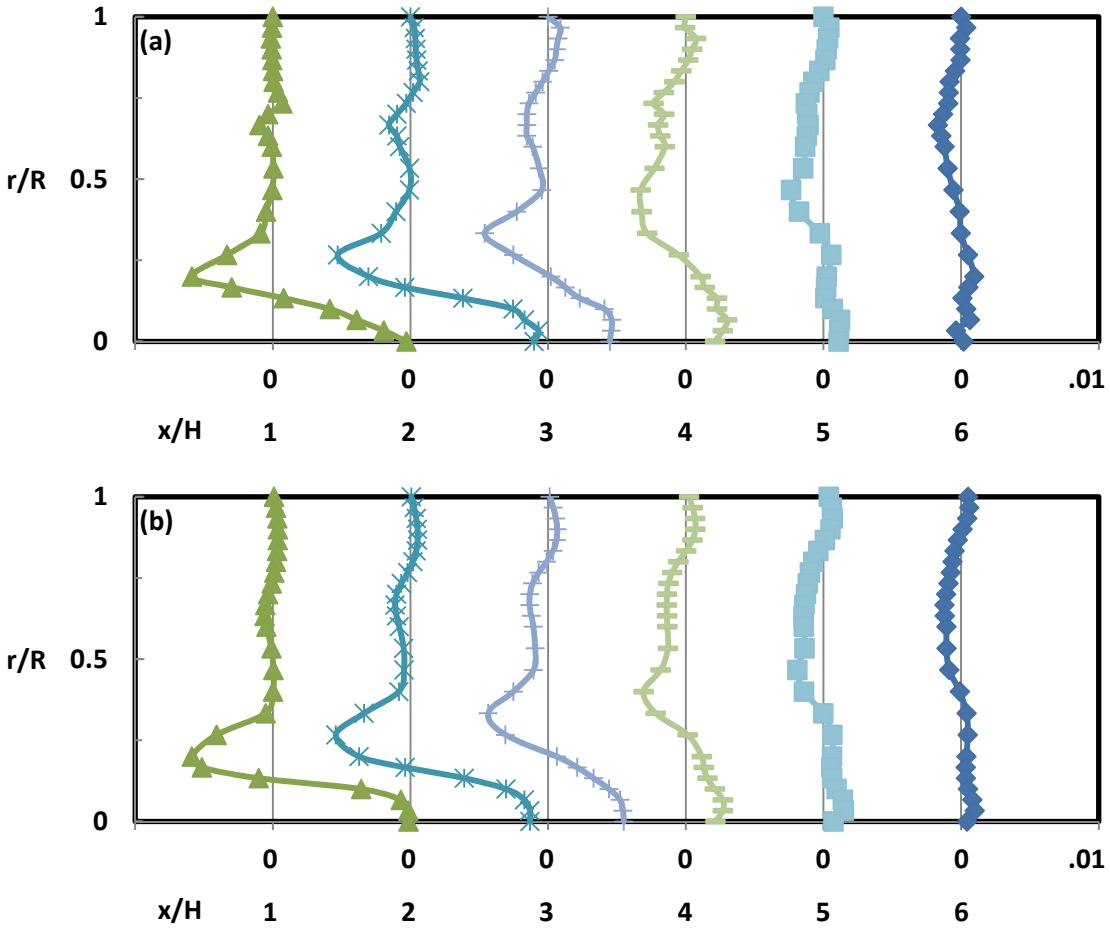

Figure 5.19 Evolution of $\overline{u'w'^2}/U_0^3$ at 0.5 swirler, Zeros indicate the origin for each profile, and the Scale is given by number at the end right. (a)Experimental (b)ANN

The success of reconstructing turbulence statistics using ANN encourages producing more profiles between the experimental ones, this is very practical since it decreases the unit steps between data points, which gives more accurate values for stream function and TKE equation.

The process is initiated by entering data points at the desired locations, the constructed network is trained on all experimental data, and then it is asked to produce the output at these locations. The step size between all data points is

set to be 0.1, in other words, more data is established between the experimental ones to set $\Delta(x/H) = \Delta(\mathrm{r/R}) = 0.1$.

To ensure that ANN is generating precise outputs, surface plots are sketched for each component, and then the smoothness of these surfaces can give an indication of the generating process. Figure 5.20, 5.22, 5.24, 5.26, 5.28, 5.30, 5.32, 5.34, 5.36, 5.38, 5.40, 5.42, 5.44, 5.46, 5.48 show the experimental near field turbulence statistics distribution, while figure 5.21, 5.23, 5.25, 5.27, 5.29, 5.31, 5.33, 5.35, 5.37, 5.39, 5.41, 5.43, 5.45, 5.47, 5.49 illustrate ANN turbulence statistics distribution.

As shown below, The mesh size is considerably reduced after exploiting ANN. ANN successfully managed to implement all components except triple velocity correlations $\overline{u'^2v'}/\mathrm{U_o^3}$ and $\overline{u'^2w'}/\mathrm{U_o^3}$. For the rest components, ANN is able to preserve peak values as they are represented in the experimental turbulence statistics distribution. Utilizing ANN also helps smoothening all crisps and discontinuities located in experimental figures.

In figure 5.20, the distribution of the experimental axial velocity component is shown. The maximum value of the axial velocity component is located at the inlet of the chamber, midway between the centerline and the wall, and covers the area around that region with a difference of ±0.2 in r/H direction and a length of 2.5 in the x/H direction, approximately.

This is also observed by the distribution shown in figure 5.21, where axial velocity component is predicted by GFF network with 19 neurons. All profiles are reconstructed accurately since the lowest correlation coefficient is 0.995.

From both figures, a reverse flow is located at the inlet corner of the combustor, this indicates a flow in the direction opposite the flow where the fluid should reaches, which leads to generate a CRZ.

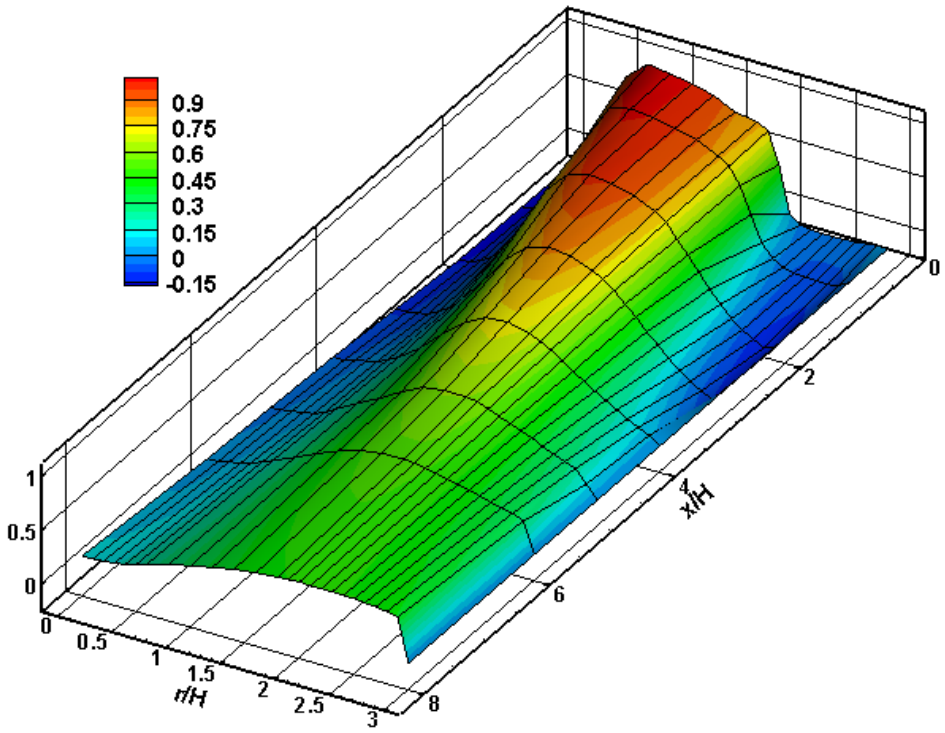

Figure 5.20 Experimental U/U_o distribution

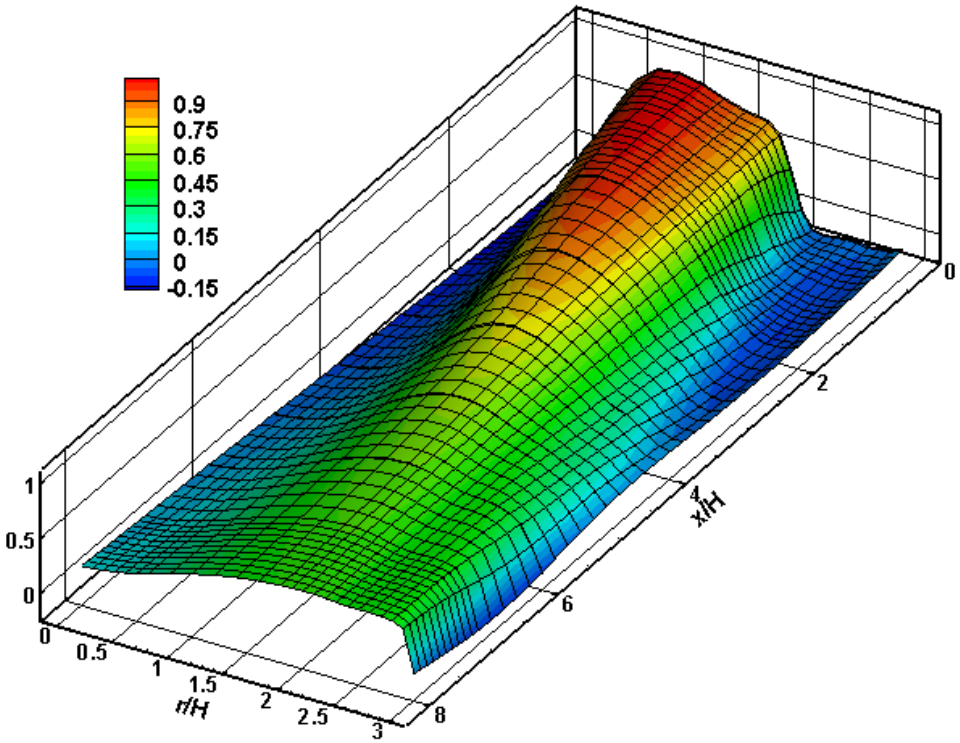

Figure 5.21 ANN U/U_o distribution

Figure 5.22 shows the distribution of the experimental radial velocity component. The values of the radial component are less than the ones presented in the axial component; this is indicated by the legend of both components. The maximum radial velocity is located at the inlet with a value of 0.14, which is located at r/H=1 approximately, but as moving far from the inlet, the location of the maximum velocity changes its location by moving towards the wall, however, the peak value decreases as going further.

The radial velocity is predicted using GFF network with 11 neurons. All near field profiles are reconstructed successfully, since the lowest obtained correlation coefficient is 0.9 at x/H=2. This is illustrated in figure 5.23, where the magnitude of the maximum value at this location is higher than the experimental measurement.

A reverse flow is also presented at the inlet corner, and it is more effective in generating a CRZ in the radial direction than the one presented in the axial direction, since the absolute difference between the peak values in both forward and reverse directions is only 0.1.

Also, as moving further towards the exhaust, specifically at x/H= 8, the flow becomes very slow until it is reversed in direction. This is successfully predicted by ANN as shown above.

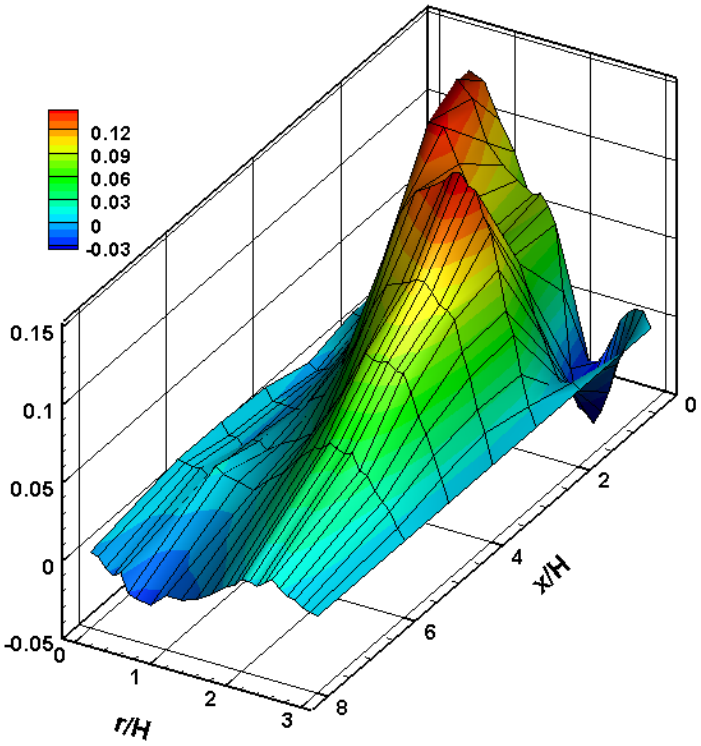

Figure 5.22 Experimental V/U_o distribution

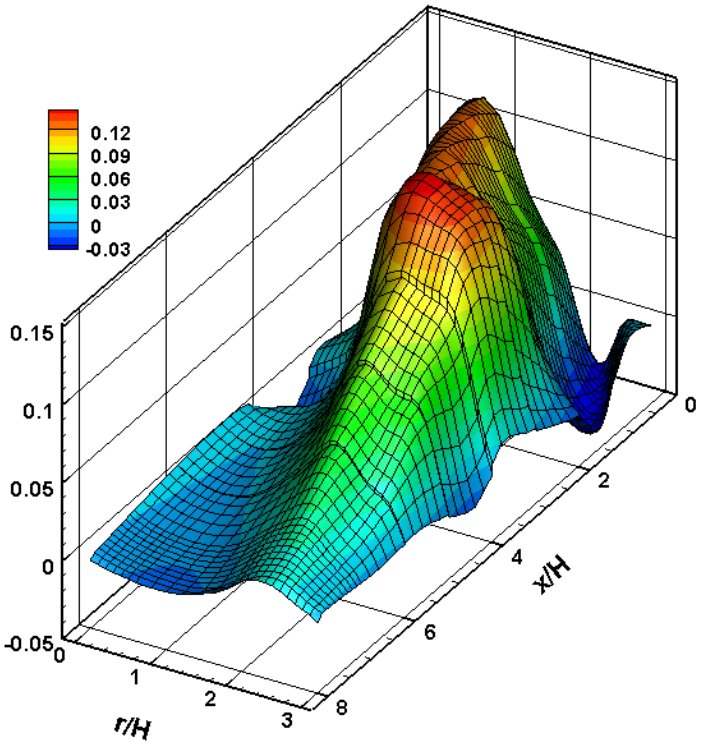

Figure 5.23 ANN V/U_o distribution

Figure 5.24 shows the distribution of the experimental velocity in the tangential direction. The values of the tangential velocity component is also less than the ones in the axial component, but higher than the ones measured in the radial direction.

There are two peak values located also at the inlet of the combustion chamber located approximately at r/H=1 and 2.5, but soon these peaks vanishes as moving further until the flow becomes stable all over the reaction area, since a small changes of the tangential values occur.

Moreover, no flow occurs at the centerline and the shear layer, since zero values obtained there. This is also successfully built using ANN, since all correlation coefficient values of all reconstructed profiles are higher 0.982. Note that no reverse flow happens in the tangential direction, since only positive values obtained there.

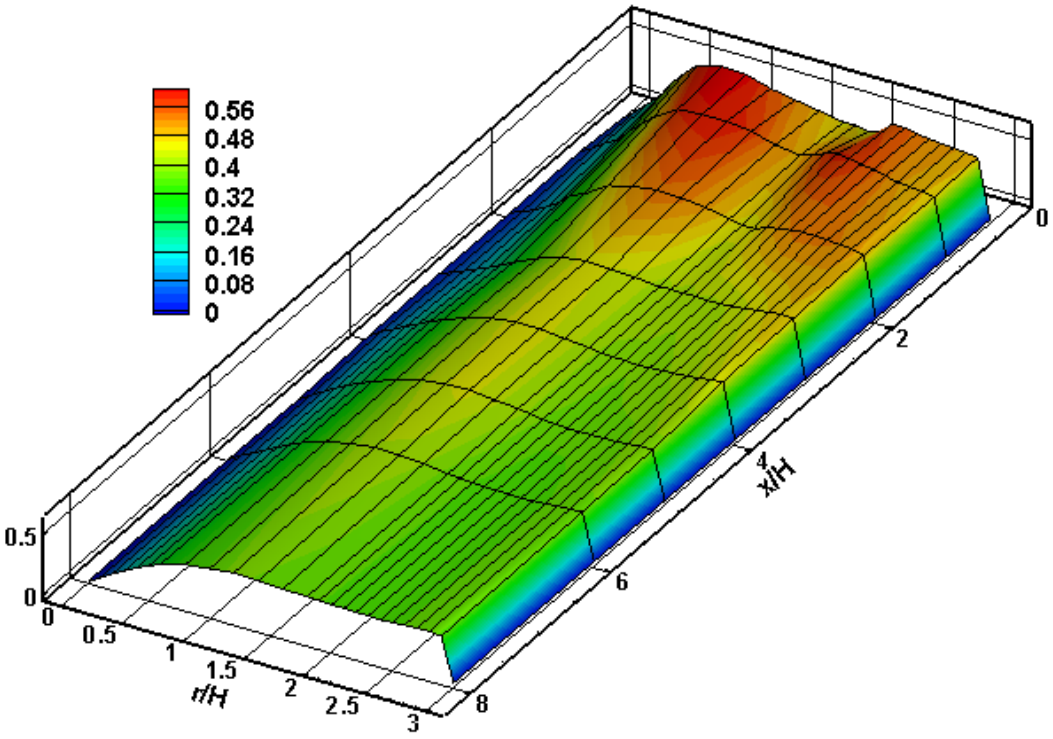

Figure 5.24 Experimental W/U_o distribution

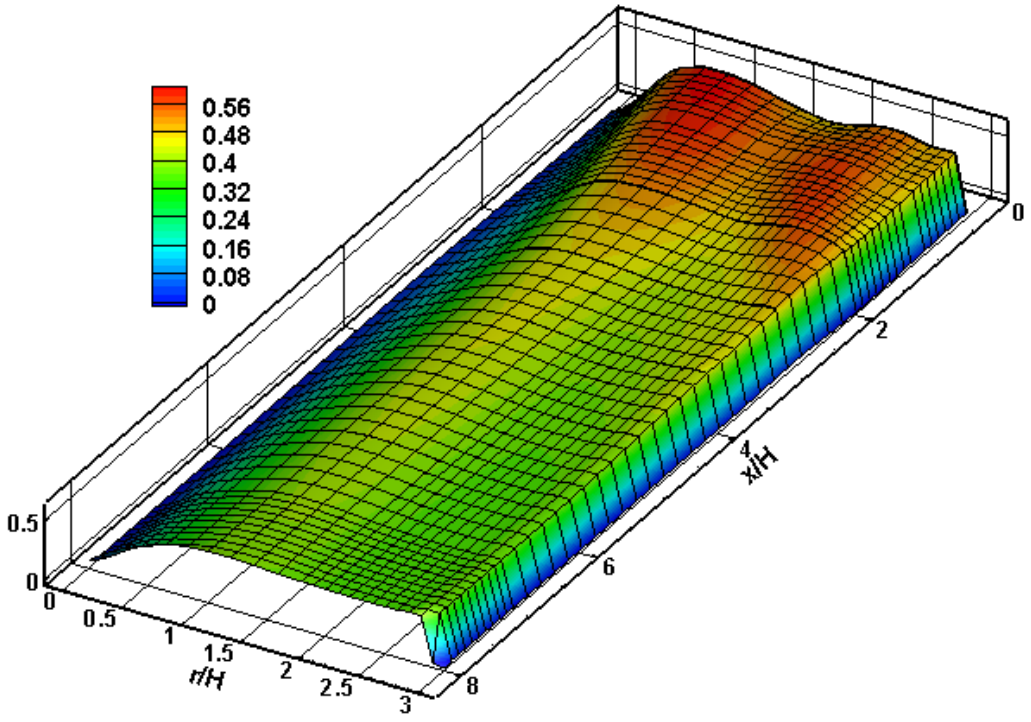

Figure 5.25 ANN W/U_o distribution

The distribution of the experimental axial fluctuating velocity component is presented in figure 5.26. The peak value is located near the centerline at approximately r/H=0.6 and at the entrance of the chamber, but soon the peak value changes its location by moving a little far from the centerline until it reaches r/H=1. Also the value of the peak decreases as moving towards the wall, but a small peak is generated r/H=2.25 approximately, but soon it vanishes as going towards the wall.

ANN managed to predict these features in addition to enhance the fact that the flame becomes stable after the reattachment point (i.e x/H=3), since nearly constant values (around 0.2) are indicated after that point.

Moreover, no activities take place at the shear layer, given that zero values obtained there as shown in both experimental and ANN figures, while most turbulence activities are concentrated in the center shear layer and the centers of the maximum values.

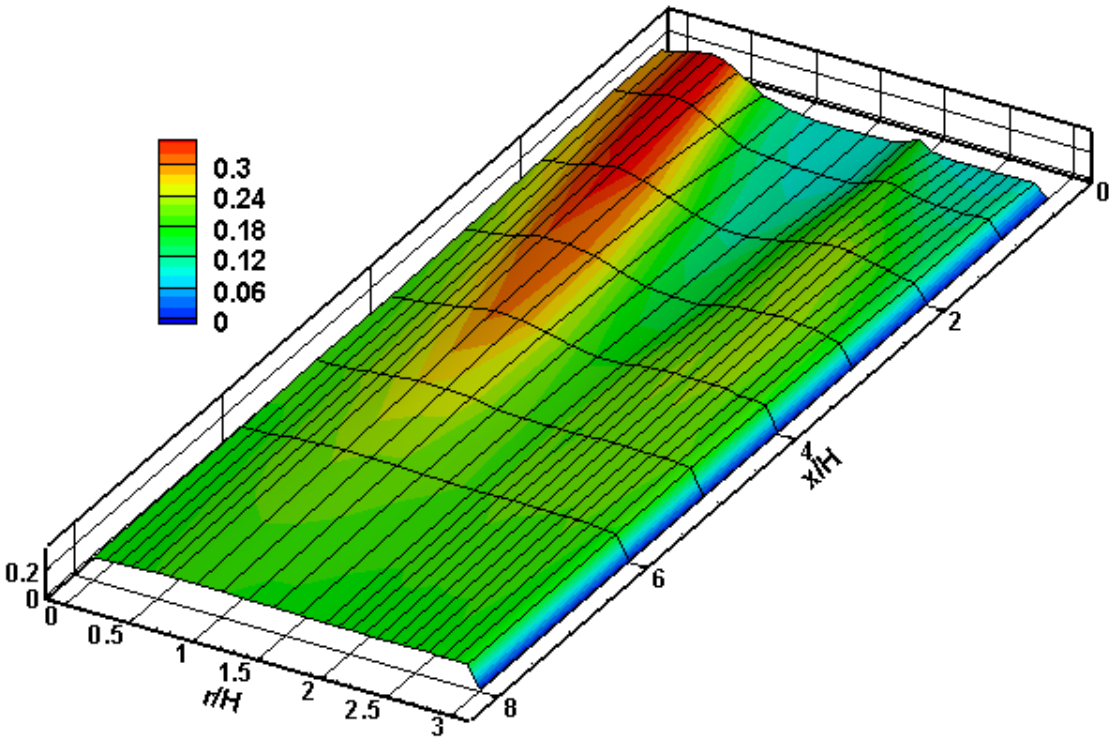

Figure 5.26 Experimental u'_{RMS}/U_0 distribution

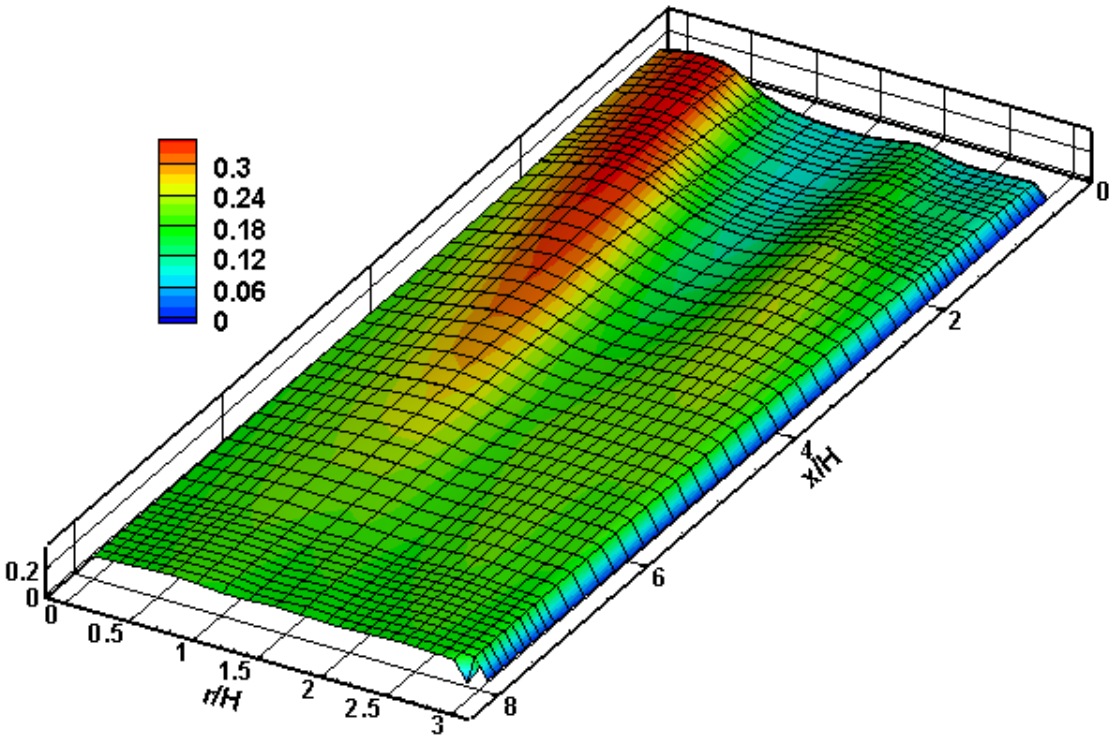

Figure 5.27 ANN u'_{RMS}/U_0 distribution

The characteristics of the radial fluctuating component is similar to the axial one, for example, the location of the peak is located at the inlet near the centerline, at approximately x/H=0.5, however, the region of peak values is more uniformly distributed in the axial fluctuating component. Also, the flame becomes uniform just after the reattachment point.

All reconstructed profiles obtained by ANN are similar to the ones shown in the experimental profiles. The correlation coefficient values all profiles are higher than 0.966, which is better than the reconstructed profiles of the fluctuating profiles in the axial direction, seeing as the values of the correlation coefficient at x/H=6 is 0.957.

Note that all values of both axial and radial fluctuating components are positive, and zero values located at the shear layer of the reaction area. This is observed also in the ANN predictions as shown in figure 5.28 and figure 5.29.

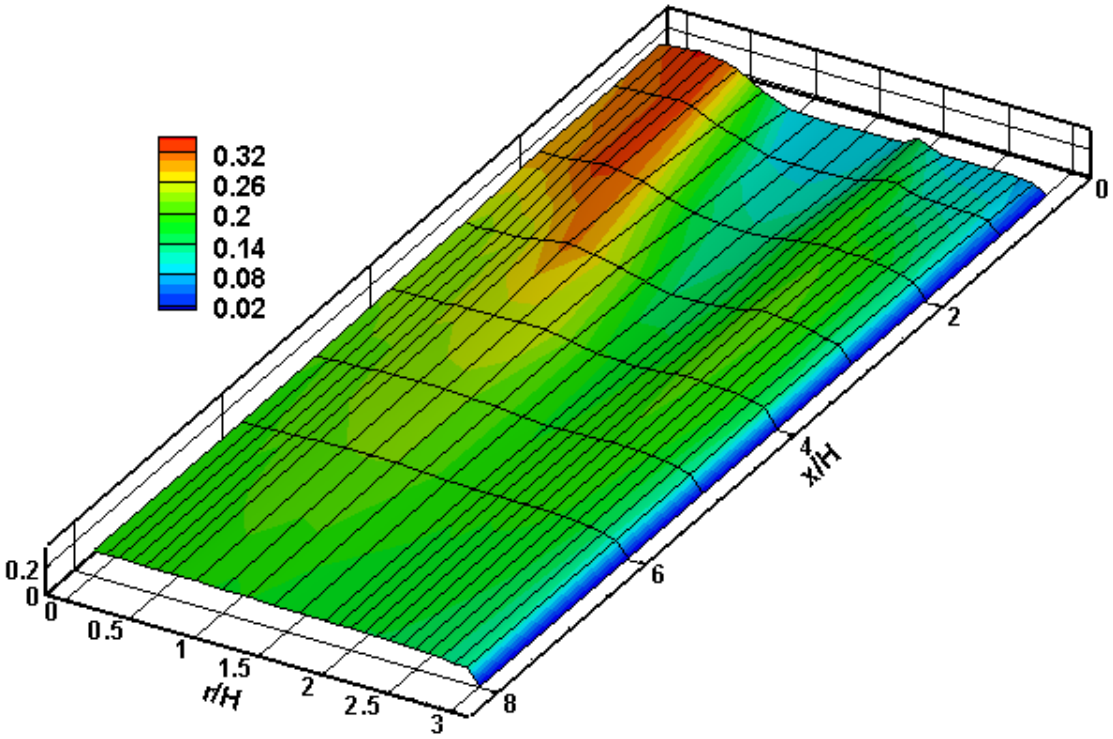

Figure 5.28 Experimental v'_{RMS}/U_odistribution

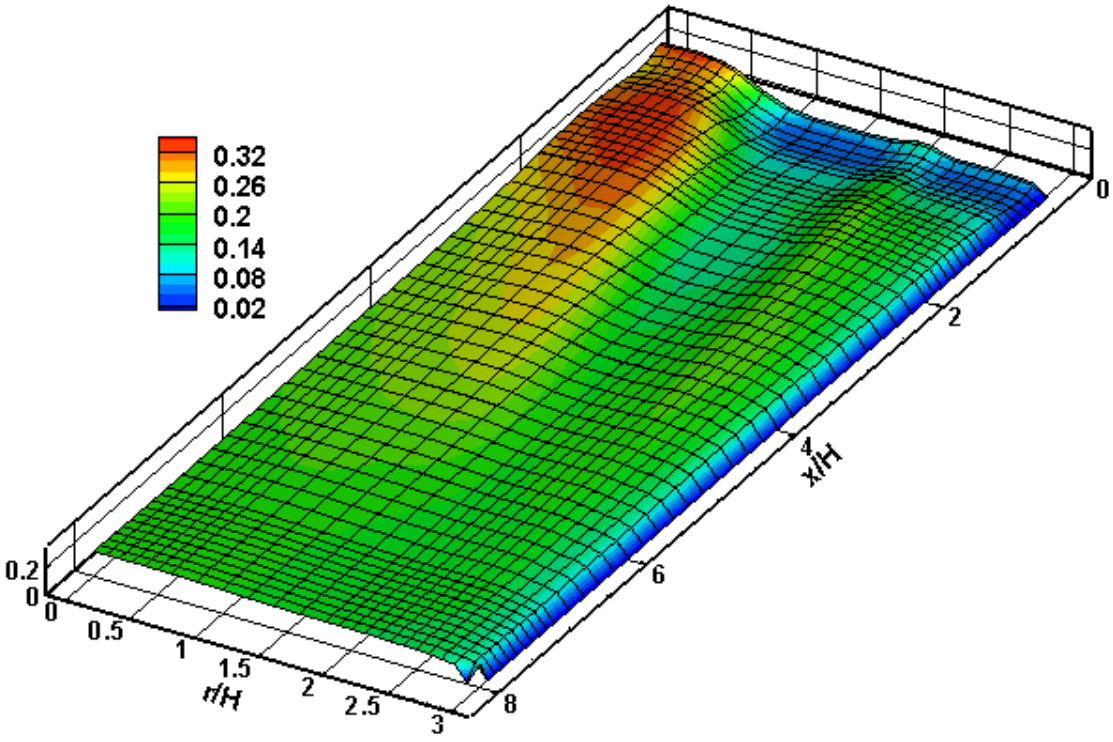

Figure 5.29 ANN v'_{RMS}/U_odistribution

Figure 5.30 shows the experimental measurements of the third normal Reynolds stress in the tangential direction. The behavior of the tangential component is also similar to the axial and radial components with difference in location of the peak region, which exists at the centerline and expands until it reaches r/H=0.5, approximately.

Also the region of low values that is located at the inlet of the chamber between the peak region and the wall becomes larger and it reaches the reattachment point, while the length of the flame becomes smaller, since the peak values vanishes just before it reaches the reattachment point. This means that the largest flame size is gained in the axial direction and then in the radial, and finally in the tangential direction.

Moreover, the small peak that is located at r/H=2.25 is less in value and larger in size in compare with the axial and radial fluctuation components. ANN managed to preserve the features of the peak value that is located at the centerline as well as the smaller peak, but the size of the small peak region is not predicted accurately as it shows in figure 5.31 that the region of this peak ends at x/H=1, while in fact, it should reach the reattachment point.

In addition, the behavior of the flow at the shear layer is successfully predicted by GFF network, which consists of 18 processing elements for all fluctuating components, and also the stability of flame which is located after the reattachment point that is shown in the experimental distribution is successfully expected by ANN.

Note that for both radial and tangential normal stresses, the flow did not recover completely near the core due to the existence of CTRZ.

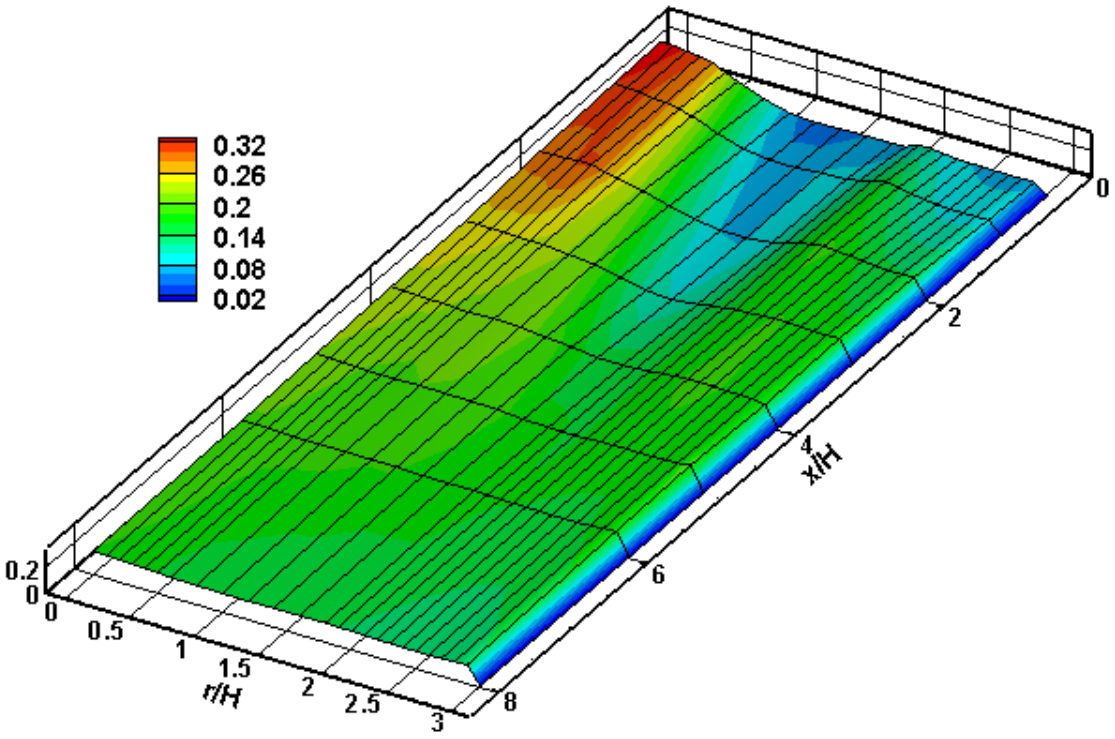

Figure 5.30 Experimental w'_{RMS}/U_o distribution

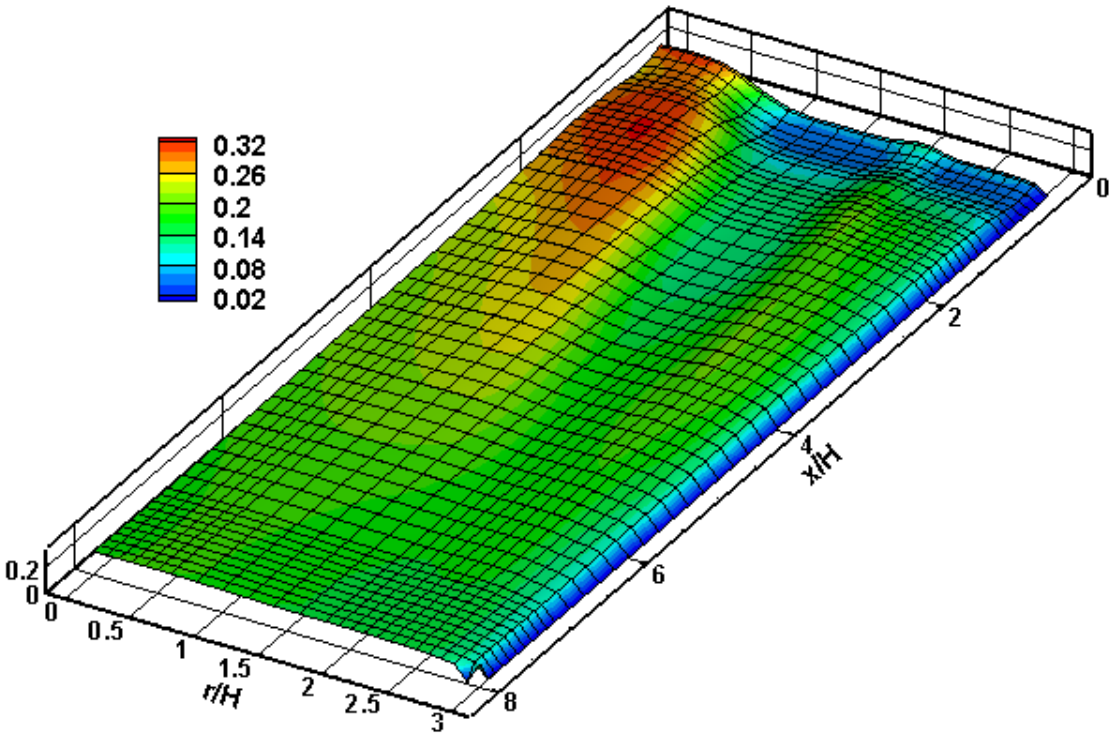

Figure 5.31 ANN w'_{RMS}/U_o distribution

Figure 5.32 shows the distribution of the experimental Reynolds shear stress in the UV plane, the scale is multiplied by 100, which preserves the fact that normal Reynolds normal stresses are much higher than the shear ones in the confined isothermal combustion case.

As can be seen, shear stresses can have negative values which might be higher in magnitude than positive ones. The maximum positive values of shear stress in the UV plane exist at near the shear layer around r/H=2.5, while the absolute maximum peak, which is negative value, occurs near the centerline at r/H=1, approximately. The absolute maximum positive peak is located at the reattachment point, while the absolute maximum negative one is at the entrance.

Note that the peak value increases as moving from the inlet towards the reattachment point until it reaches the maximum value, but soon the shear activity in that area becomes less and the value of the peak decreases as moving further towards the exit.

These features are plotted successfully in figure 5.33 using GFF network with 15 neurons, in view of the fact that all built profiles are tested and the obtained correlation coefficient values are higher than 0.96, and the NMSE values are less than 0.098.

Moreover, ANN managed to smooth the crisps between the profiles; this can be seen clearly at the peak region. Also, the predictions at the centerline and the shear layer are correct as all predicted values are very close to zero, as can be seen in figure 5.32.

Nevertheless, though the trend of the first profile in ANN plot is similar to the experimental one, the predictions attained at the inlet of the combustor are not very accurate, since no peak values are presented at this location.

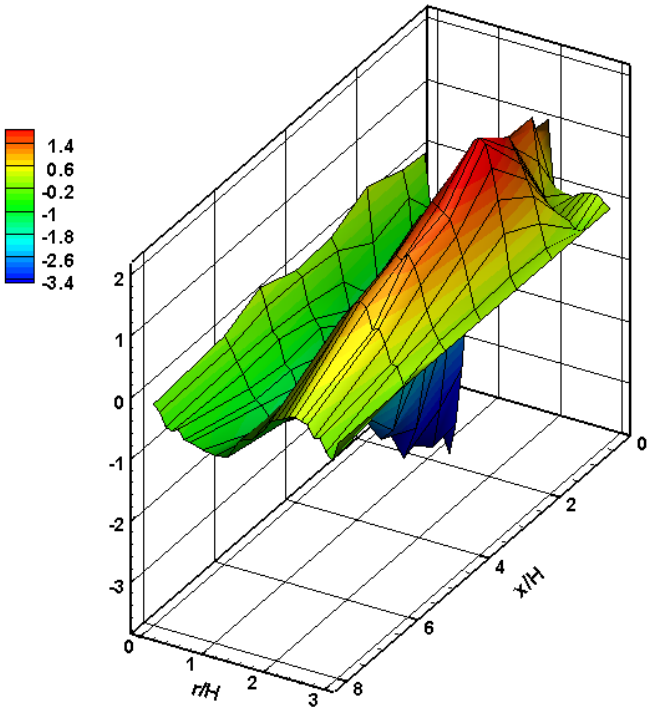

Figure 5.32 Experimental $100\overline{u'v'}/U_o^2$ distribution

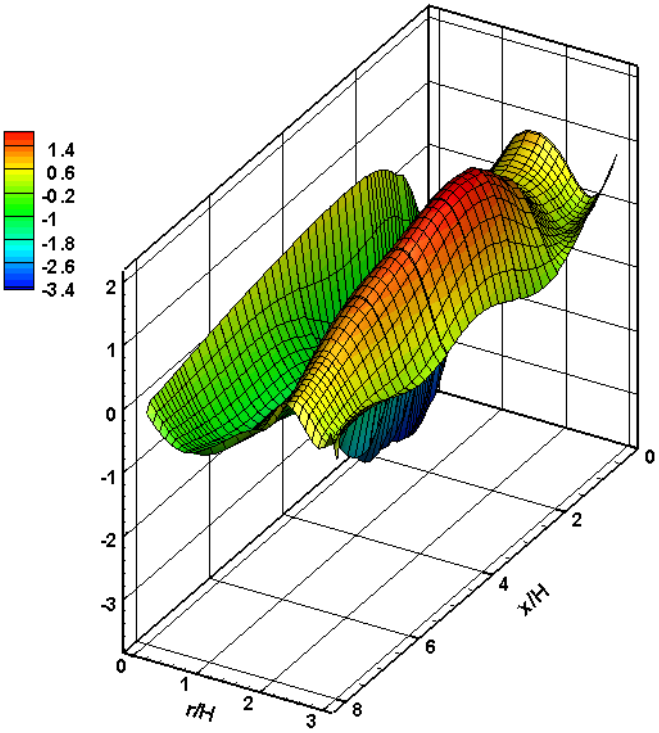

Figure 5.33 ANN $100\overline{u'v'}/U_o^2$ distribution

The distribution of experimental Reynolds shear stress is plotted in figure 5.34. As shown below, the positive peak values are not located at one region, one peak value can be located at r/H=2.5, x/H=2.5, while another one is found at r/H=1.5, x/H=4, while the absolute maximum peak, which is a negative is located approximately at r/H=0.5 and x/H=4.

As shown in both shear stresses, the shear layer is thin near the dump and then expands to fill the entire combustor as moving far away towards the exit. Also the fact that high shear stresses occur at regions of maximum velocity gradients is preserved.

Furthermore, the distribution of all normal and shear stresses confirm the observation made by Ahmed and Nejad [**6**], which states that swirl is responsible for increasing the values of normal and shear stresses by approximately an order of magnitude.

The Reynolds shear stress is reconstructed using GFF network with 13 processing elements; all profiles are renovated successfully with correlation coefficient values higher than 0.862.

The highest NMSE value is gotten when reconstructing x/H=3, its values is 0.4, this gives an indication of the succeed in utilizing ANN for predicting normal Reynolds stresses as well as shear ones too.

Regardless the inability of acquiring exact values near the shear layer, the trend of the profiles through the entire combustion zone is well plotted, as most peak values are captured correctly and the behavior of the flow at the centerline and the shear layer are predicted accurately.

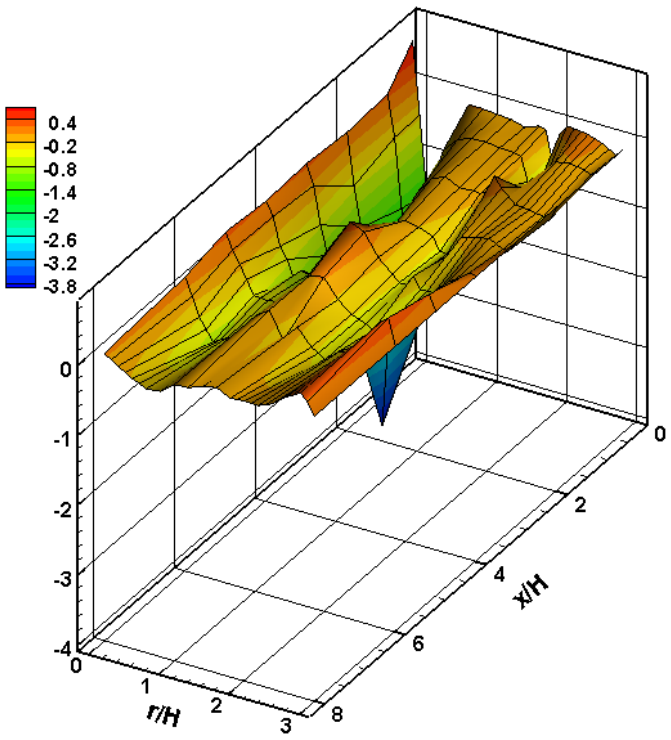

Figure 5.34 Experimental $100\overline{u'w'}/U_o^2$ distribution

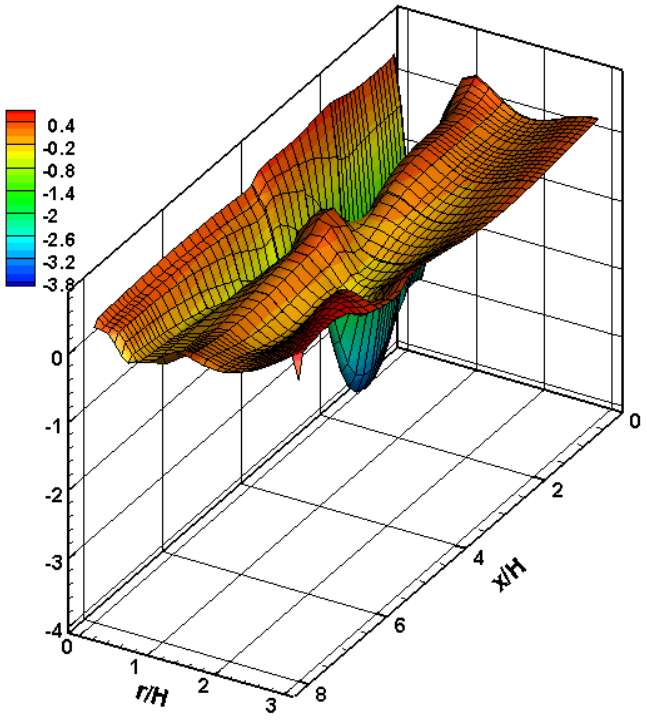

Figure 5.35 ANN $100\overline{u'w'}/U_o^2$ distribution

Figure 5.36 shows the distribution of the experimental triple velocity correlation ($\overline{u'^3}$). The positive peak value is located at the inlet and the centerline of the combustor, while the absolute maximum peak, which is negative value, is found halfway between the centerline and the shear layer, however, the location of this peak moves towards the shear layer until it dies out downstream at x/H=4.

Furthermore, the characteristics of the triple velocity correlation ($\overline{u'^3}$) are asymmetric about the centerline of the shear layer, and the peaks at the shear layer side come into view and diminish when they reach the shear layer. Note that most activities occur upstream before x/H=6.

The distribution of the triple velocity correlation ($\overline{u'^3}$) constructed by ANN is shown in figure 5.37. Most features are erected successfully, for example, the positive and negative peaks are located correctly and their values are similar to the ones in the experimental data.

The network used to predict the behavior of the triple velocity correlation ($\overline{u'^3}$) is GFF using 14 processing elements. The values of the correlation coefficient for all profiles are higher than 0.93, and the highest NMSE value is found after testing the fifth profile (i.e x/H=5) which equals 0.46. This is the reason behind the sudden initiating of small peaks at that location, as shown below.

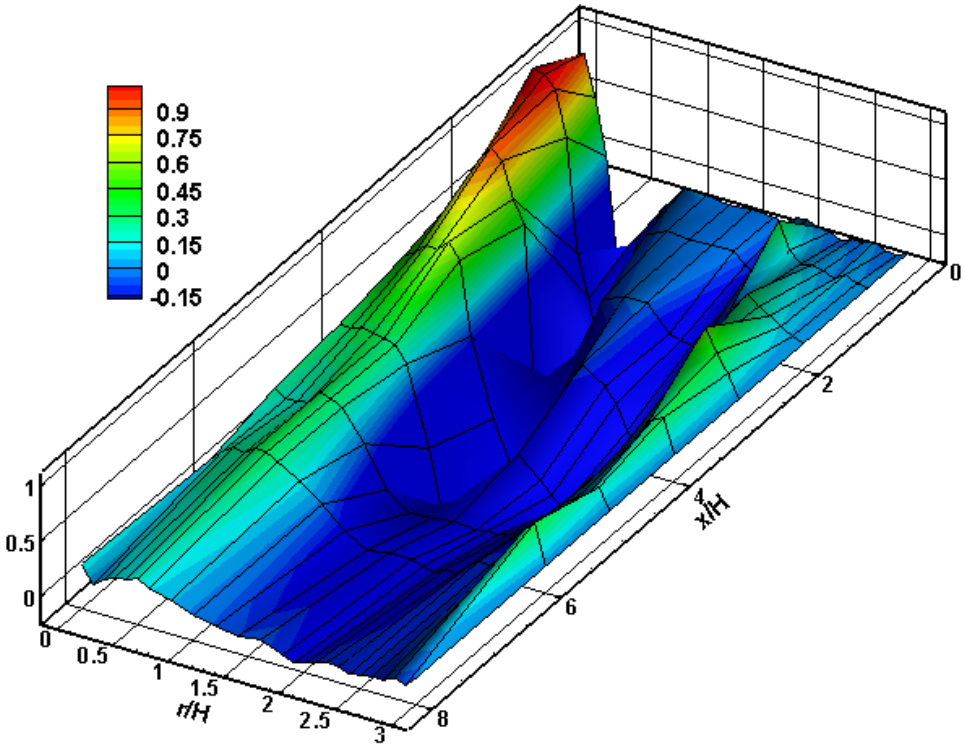

Figure 5.36 Experimental $100\overline{u'^3}/U_o^3$ distribution

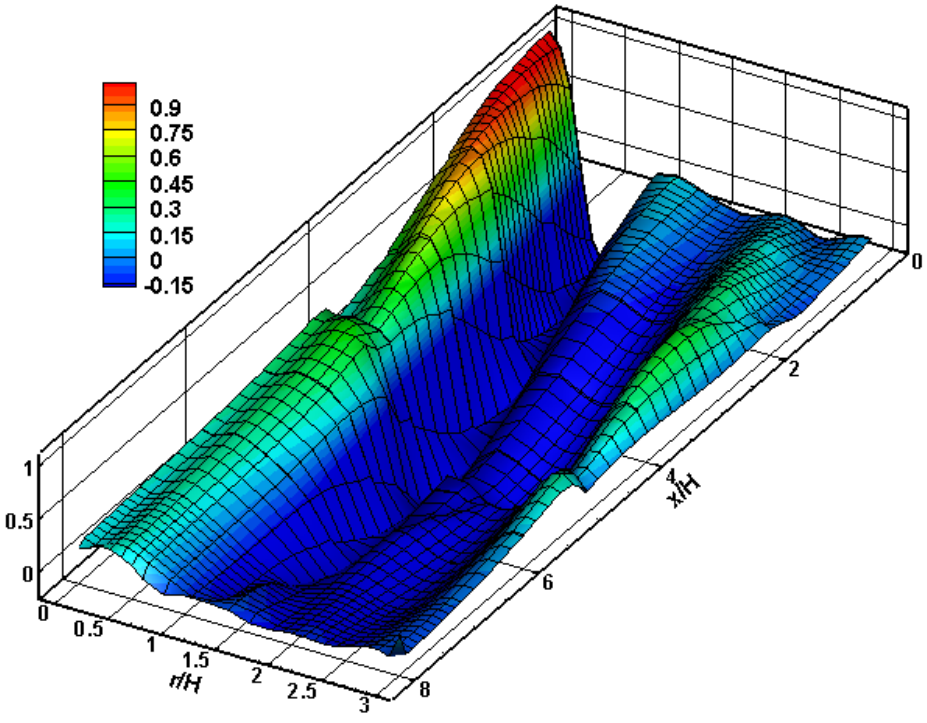

Figure 5.37 ANN $100\overline{u'^3}/U_o^3$ distribution

Figure 5.38 shows the distribution of the experimental triple velocity correlation ($\overline{v'^3}$), while figure 5.39 illustrates the distribution of this component using GFF network with 13 neurons.

The testing results between the experimental and the produced profiles by ANN are slightly less than the ones acquired from ($\overline{u'^3}$), from the time when the correlation coefficient values are less than 0.9 for all profiles, but higher than 0.81, except at x/H=3, where the value of the correlation coefficient is 0.72.

The NMSE values range between 0.43 and 1.38, which is high in compare with the previous turbulence statistics. Nevertheless, the constructed plot by ANN is still able to show the main features at their correct locations, but with different values, such as the peak located at the centerline and r/H=1.3, where the size of the region is successfully predicted, while the values of the peaks are less than observed in the experimental plot.

Also, ANN managed to show the symmetry of the negative regions located on both sides of the midway between the shear layer and the centerline, and the values are almost the same, except at the first peak that exists near the shear layer at the inlet of the combustor.

Note all peak values, either they are negative or positive, are less than the peaks in the triple velocity correlation $\left(\overline{u'^3}\right)$, which can be noticed from the scale of both products.

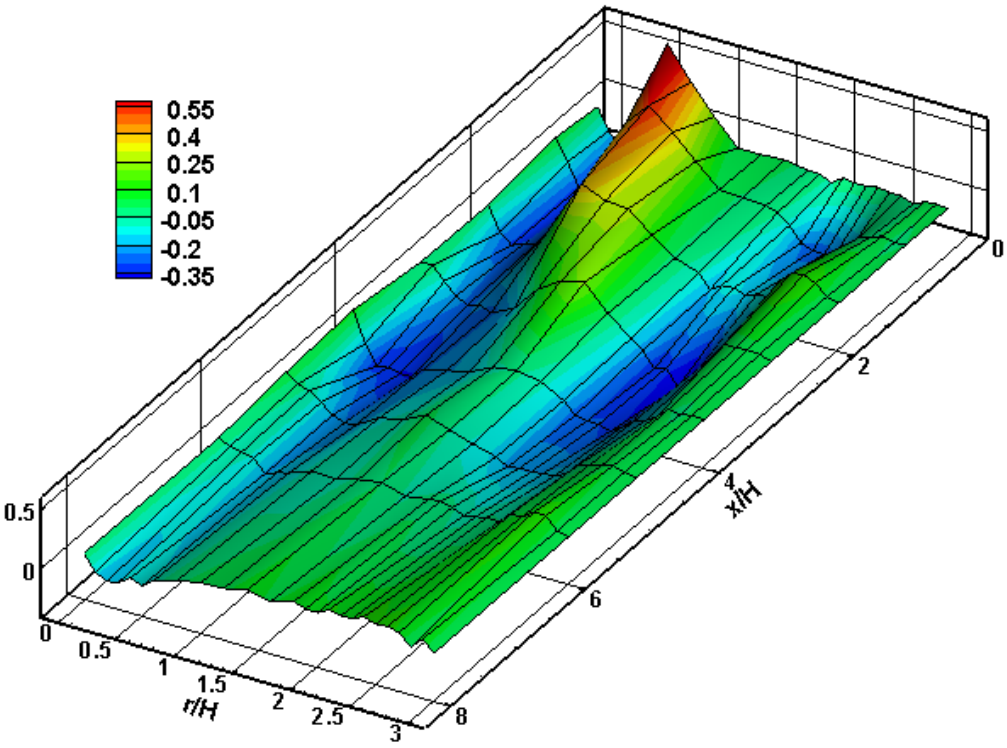

Figure 5.38 Experimental $100\overline{v'^3}/U_o^3$ distribution

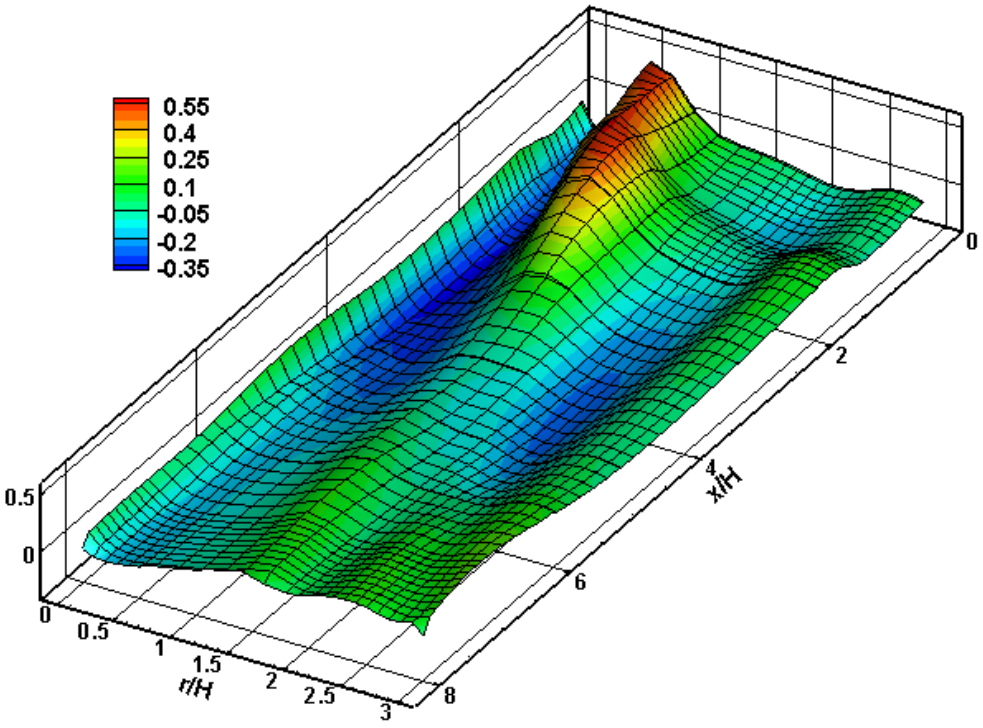

Figure 5.39 ANN $100\overline{v'^3}/U_o^3$ distribution

The distribution of the tangential triple velocity product is shown in figure 5.40 and figure 5.41, they represent the experimental and ANN profiles, respectively.

The experimental plot shows peaks at several places, which are symmetric about r/H=1.5 in locations, but different in values. These peaks reduce in amount as going downstream until they generate a negative peak at x/H=0.6.

Though the predictions obtained by ANN not accurate, ANN is still able to predict the location of most features throughout the combustion area, such as the peak at the centerline and the inlet of the chamber, and the peaks near the shear layer. The data is predicted using GFF network with 9 neurons only, this gives an advantage when producing the data of ($\overline{w'^3}$), which is time saving during training the data.

In spite of the high values of correlation coefficient, which are between 0.81 and 0.95, the NMSE values are comparably higher than the previous turbulence statistics, as they exceed 1 for two profiles.

The main reason behind the failure of guessing the values of the peaks is because of the sudden initiation of these peaks, seeing as they are initiated at one profile and disappear at the next profile, before another peak is generated. This prevents ANN from constructing the profiles correctly, since generating each profile depends on the closest two profiles before and after the desired one.

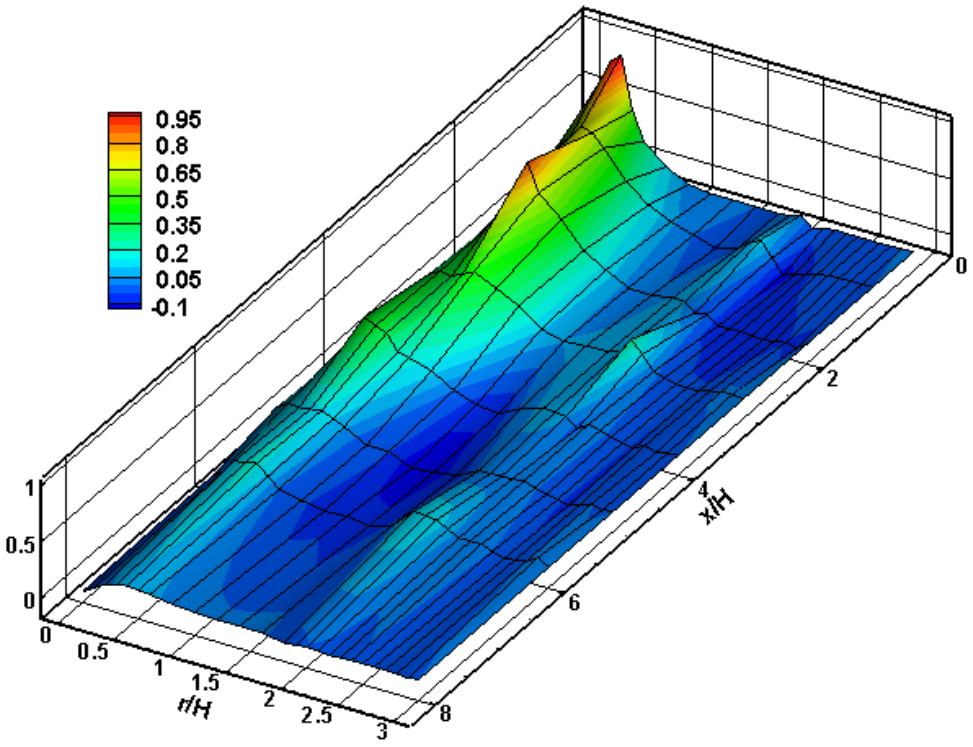

Figure 5.40 Experimental $100\overline{w'^3}/U_o^3$ distribution

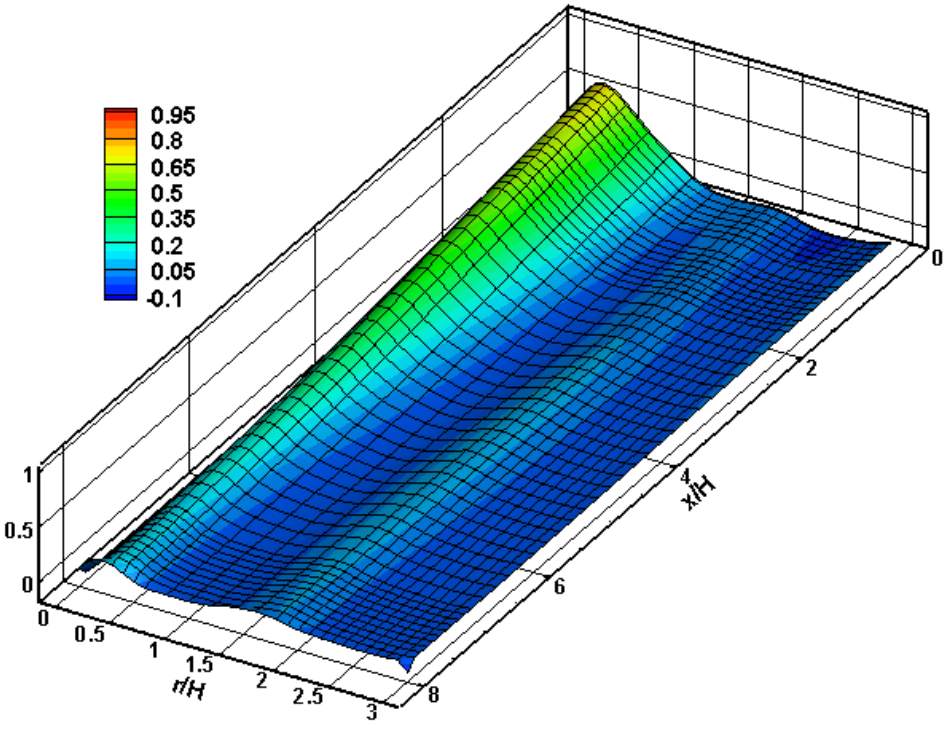

Figure 5.41 ANN $100\overline{w'^3}/U_o^3$ distribution

Figure 5.42 points up one of the turbulence statistics where ANN failed to predict its behavior, which is $\overline{u'^2v'}$. As shown above, $\overline{u'^2v'}$ contains positive peak region which is initiated at the entrance and around r/H=1.3, and diminish as moving downstream until x/H=4.

Similar to other triple velocity product correlations, $\overline{u'^2v'}$ is symmetric about the centerline of the shear layer, where two negative peaks are located at r/H=0.75 and 2.25. These peaks are relatively high comparing to its positive maximum point.

Most activities become uniform downstream when they reach x/H=6. Note the small peaks that are generated near of the shear layer because of the swirler, and die out as they reach the wall, such as the one located at x/H=2.

As shown figure 5.43, the distribution constructed by ANN, which is formed using CANFIS network this time with 6 membership functions. Except at x/H=1, all correlation coefficient values that are calculated from testing the network are less than 0.726.

ANN failed to predict the values of all peaks, but their locations are correct. ANN is not able to generate the profile of $\overline{u'^2v'}$ correctly because of the sudden changes between each profile and its neighbor ones, and since ANN neurons weights are mainly affected by the previous and next profiles, it was unable to provide a satisfied distribution of this product. This is also the same reason for $\overline{u'^2w'}$, where ANN also could not manage to reconstruct its characteristics.

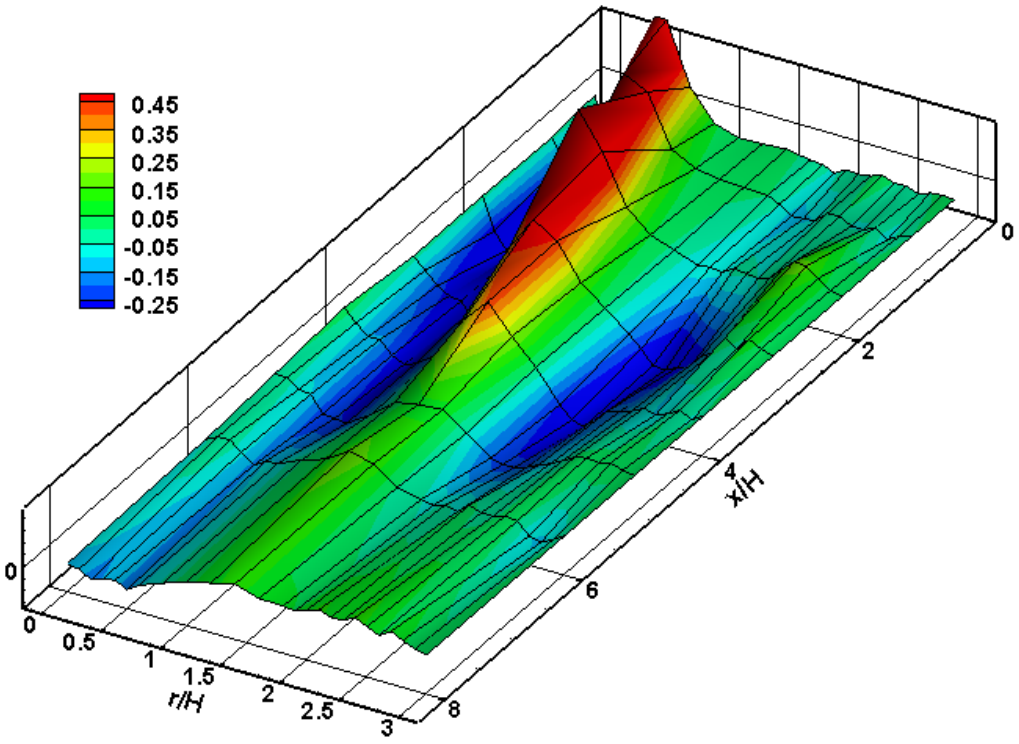

Figure 5.42 Experimental $100\overline{u'^2v'}/U_0^3$ distribution

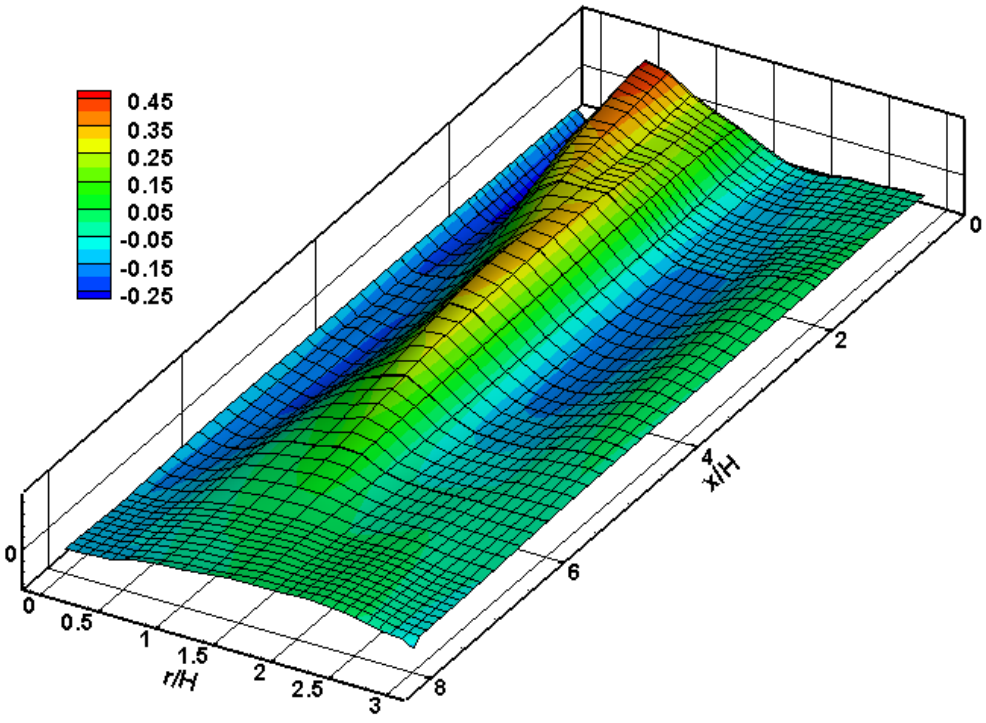

Figure 5.43 ANN $100\overline{u'^2v'}/U_0^3$ distribution

Figure 5.44 shows the distribution of experimental $\overline{u'v'^2}$, normalized like all other triple velocity correlations by U_o^3 and multiplied by 100. There are mainly two peaks which characterize the behavior of $\overline{u'v'^2}$, the positive one is created at the inlet of the combustor and the centerline, its values decreases as going further downstream towards the exhaust. The absolute maximum peak is negative one, located near the midway between the centerline and the shear layer, and starts at the inlet until it vanishes when x/H=4. Some other peaks are also created at several locations, for example the ones located at the wall, but are small in size.

The network that successfully predicts all characteristics of $\overline{u'v'^2}$ is GFF network 14 processing elements. All profiles are reconstructed accurately with correlation coefficient values higher than 0.84. The peaks gradient are smoothened which provides a continuous distribution, also the mesh size is fined and all features are presented at their locations with very close values to the experimental ones.

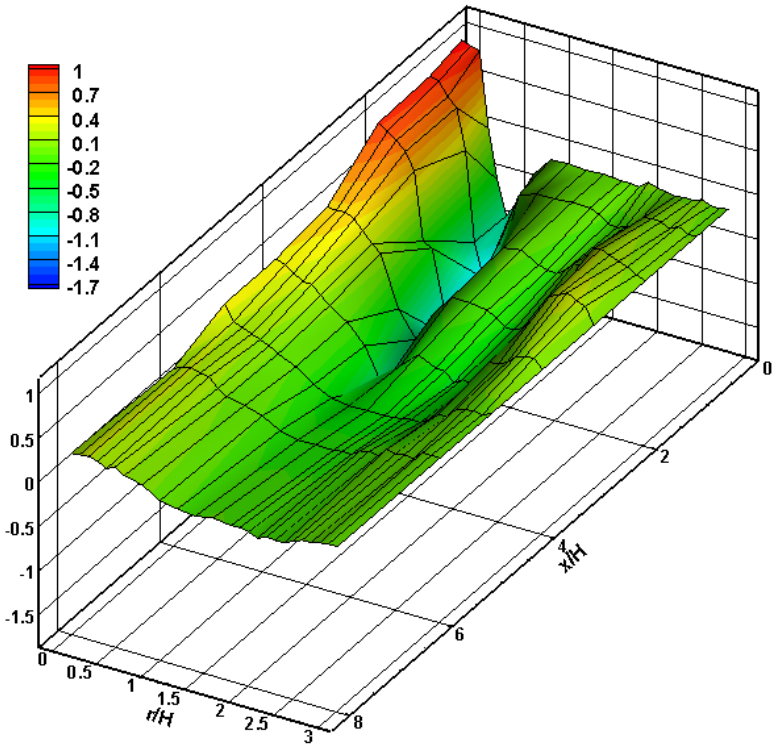

Figure 5.44 Experimental $100\overline{u'v'^2}/U_o^3$ distribution

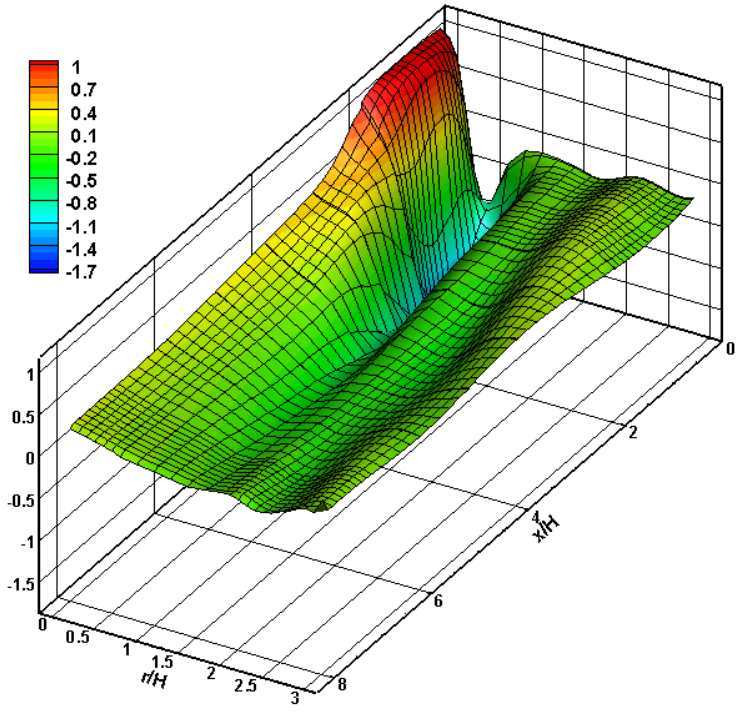

Figure 5.45 ANN $100\overline{u'v'^2}/U_o^3$ distribution

ANN gives a promising solution for predicting all turbulence statistics, regardless the order of the components; all products are reconstructed successfully except $\overline{u'^2v'}$ and $\overline{u'^2w'}$, using GFF network with number of neurons ranges between 9 and 19.

This helps in optimizing combustor design, since it enhances the knowledge of the characteristics of most turbulence statistics and the main features and changes that are caused from using swirler.

ANN is utilized here to predict the behavior of fluid flowfield characteristics when the swirl number is less or equal 0.5, but this can be generalized for higher swirl numbers.

CHAPTER 6

CALCULATION OF STREAM FUNCTION AND TKE EQUATION

6.1 Stream Function

To describe the streamlines and flow velocity in a three-dimensional incompressible flow with axisymmetry, the Stokes stream function is used. Surface with a constant value of the Stokes stream function encloses a stream tube, everywhere tangential to the flow velocity vectors. Further, the volume flux within this stream tube is constant, and all the streamlines of the flow are located on this surface. The velocity field associated with the Stokes stream function is solenoidal, it has zero divergence. Normalized stream function is defined in equation (5.8):

$$\Psi(\mathrm{r}) = 1 - \left(\int_0^{\mathrm{r}} \mathrm{Ur}\ \mathrm{dr} \Big/ \int_0^{\mathrm{r_c}} \mathrm{Ur}\ \mathrm{dr}\right) \tag{6.1}$$

Zero values of Ψ depicts the corner recirculation zone boundaries, while Ψ=1 is the boundary of toroidal recirculation region. The second recirculation region is only generated in the swirling case. This can be clearly shown by plotting the contour plots of the stream function.

The stream function in this study is evaluated numerically using trapezoidal integration technique, which is defined as:

$$\int_a^b f(x)dx \approx (b-a)\frac{f(a)+f(b)}{2} \tag{6.2}$$

Where a and b are the limits of the integral, $f(a)$ and $f(b)$ are the outputs of the function corresponding to a and b, respectively. Thus the stream function can be rewritten in the following formula:

$$\Psi(\mathrm{r}) = 1 - \frac{\sum_0^r (r_{i+1}-r_i)[U(r_{i+1})+U(r_i)]}{\sum_0^r (r_{i+1}-r_i)[U(r_{i+1})+U(r_i)]} \tag{6.3}$$

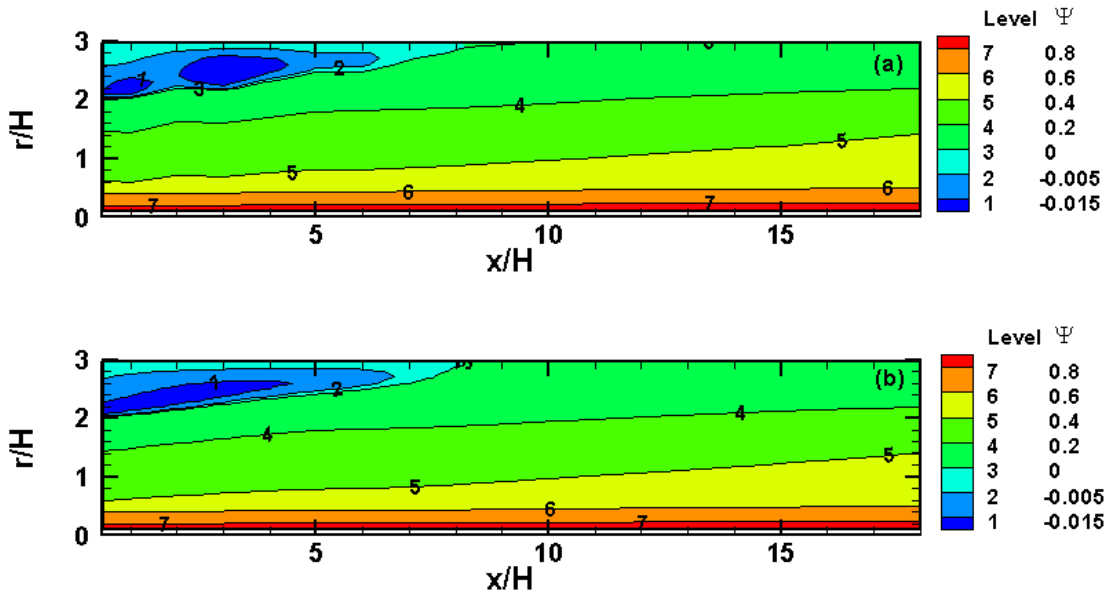

Figure 6.1 Non-dimensional stream function contours at S_n =0 (a) Experimental (b) ANN

Figure 6.1 shows the contour of non-dimensional stream function in no swirling case, (a) represents the experimental contour while (b) is generated by ANN. Since the stream function is mainly a function of the axial velocity component, the same network is used to generate the contour profiles of the stream function, which is GFF network with 19 neurons.

In both figures, CRZ are clearly shown at the upper corner of both plots, however, ANN managed to connect between both zones because many profiles are generated between the experimental ones. It is known that all contours must be closed when they reach the wall, this is not the case at Ψ=0 in the experimental one, since no enough profiles are used to plot the contour. ANN solves this issue as shown above by closing this profile at x/H=8.2, approximately.

Figure 6.2 shows the non-dimensional stream function contours at S_n=0.3, this figure is similar to the previous one where no CTRZ is created, however, the CRZ becomes smaller as the size of its region close at x/H=4,

while ANN predicts the closure of this contour to be at x/H=5. ANN also connected between the contours that have values of Ψ less than zero.

Moreover, the small wiggling which are located between x/H=0 and 5 have been cleared by ANN. Note that the region of contours that have values of Ψ higher than zero become wider, this fact is also preserved by the predictions obtained by ANN.

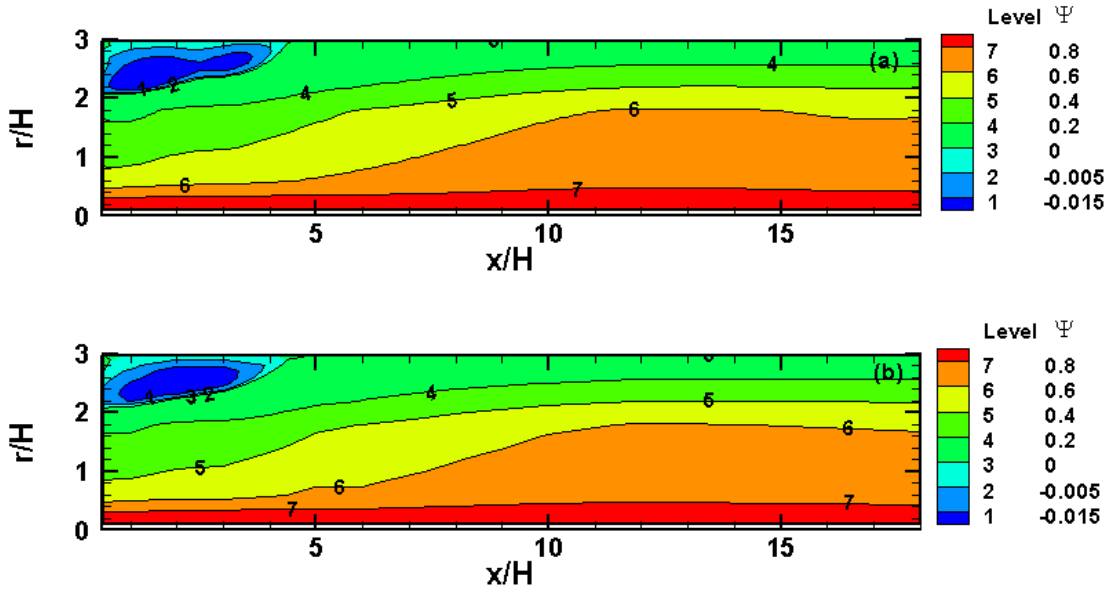

Figure 6.2 Non-dimensional stream function contours at S_n =0.3 (a) Experimental (b) ANN

Similarly for figure 6.3, which has the same characteristics of 0.3 swirl. The CRZ becomes smaller, while the regions of Ψ larger than 0.4 cover a wide range of the combustor downstream, which means a uniform flow is recovered. These facts are observed also in the contour that is generated by GFF network, both experimental and ANN plots are very close to each other, and the differences barely appear, for example, at level 2, the shape is not circular at x/H=3.5, while ANN managed to make it smoother, also, at Ψ=0, the contour intercepts the shear layer at x/H>4, but in ANN plot, it touches it exactly at x/H=4. Note that the maximum value of Ψ is 0.8, which means no CTRZ are created at 0.4 swirl.

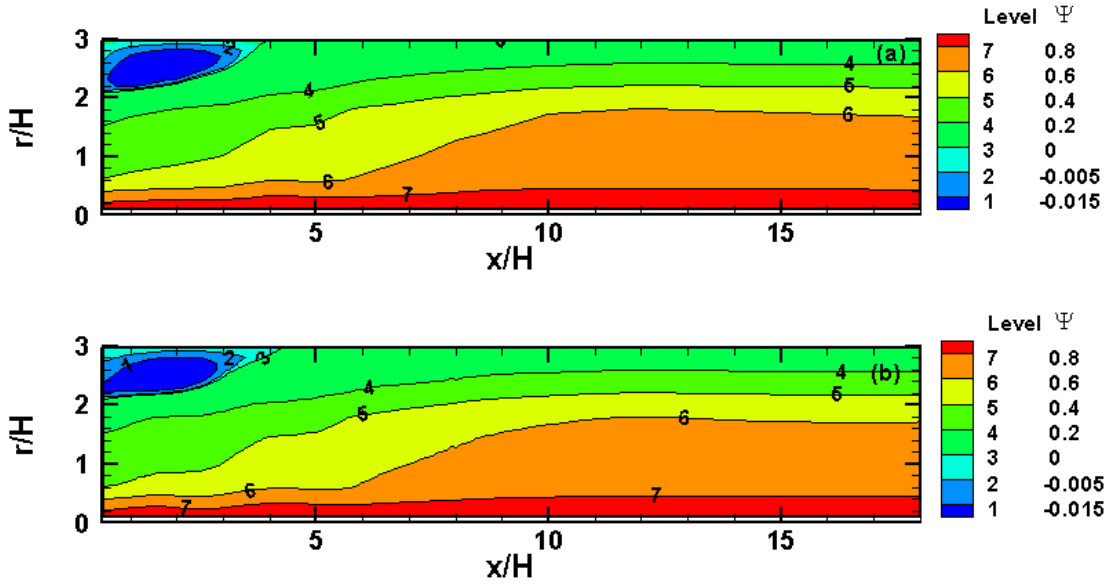

Figure 6.3 Non-dimensional stream function contours at S_n =0.4 (a) Experimental (b) ANN

Figure 6.4 (a) and (b) show the experimental and ANN contours of non-dimensional stream function at 0.5 swirl, respectively. It is clearly seen that the size of CRZ decreases, while a new recirculation zone is created, which is CTRZ, it is created near the centerline when the swirl number is higher or equals 0.5. This zone is successfully predicted by ANN as it is initiated at the same location, however, the contour at Ψ=1 in the experimental case intercepts the centerline at x/H>5, while in ANN plot, the contour intercepts at x/H=5. Note that contours with values of Ψ higher than 0.6 are affected from the swirler, this gives them circular profiles as they die out downstream at x/H=10.

The contour of zero stream function looks smoother in ANN plot, since it has a circular and closed profile shape. Note that the value of Ψ exceeds one as it also has low negative values, this satisfies the fact that swirler is responsible on creating CTRZ and reduces CRZ until it completely disappears at higher swirl numbers.

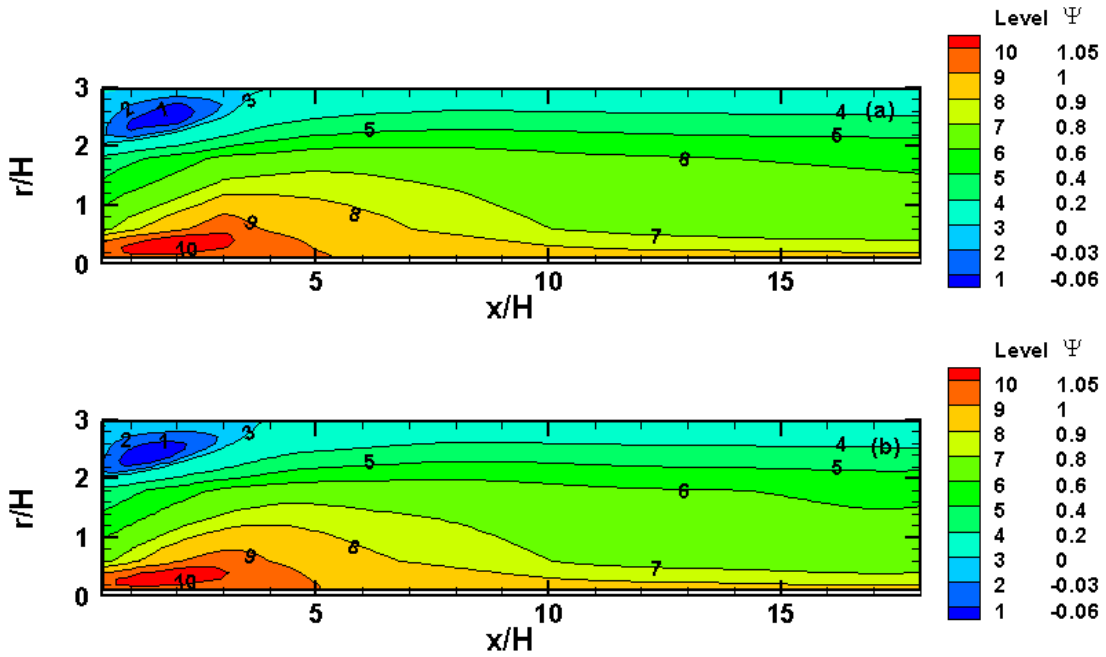

Figure 6.4 Non-dimensional stream function contours at S_n =0.5 (a) Experimental (b) ANN

At 0, 0.3, 0.4 and 0.5 swirlers, recirculation zone boundaries exist at Ψ=0. These recirculation zones, however, lengthen as the value of swirl number decreases, since the swirler responsibility is to shorten the circulation zone boundaries. At Ψ=1, another recirculation region exists, which is known as central toroidal recirculation zone, occurs at 0.5 swirler. This type of recirculation only exists in swirling case.

6.2 Turbulent Kinetic Energy Equation

The importance of turbulence kinetic energy comes from its functionality of characterizing the velocity fluctuations, since production, diffusion, convection, and viscous dissipation terms are included in the equation, TKE can be produced by fluid shear, friction or buoyancy, or through external forcing at low-frequency Eddie scales (integral scale). Turbulence kinetic energy is then transferred down the turbulence energy cascade. The TKE equation can be written in cylindrical coordinates x, r, θ as [**45**]:

$$U\frac{\partial k}{\partial x} + V\frac{\partial k}{\partial r} = \qquad (6.4\text{ a})$$

$$-\left[\overline{v'^2}\frac{\partial V}{\partial r}+\overline{u'v'}\frac{\partial U}{\partial r}+\overline{u'v'}\frac{\partial V}{\partial x}+\overline{u'^2}\frac{\partial U}{\partial x}+\overline{w'^2}\frac{V}{r}+\overline{u'w'}\frac{\partial W}{\partial x}+\overline{v'w'}\frac{\partial W}{\partial r}+\overline{v'w'}\frac{W}{r}\right] \quad (6.4\text{ b})$$

$$+\frac{1}{\bar{\rho}}\frac{\partial}{\partial x}\left[-\bar{\rho}\frac{\overline{u'v'^2}}{2}-\bar{\rho}\frac{\overline{u'w'^2}}{2}-\bar{\rho}\frac{\overline{u'^3}}{2}\right]+\frac{1}{\bar{\rho}r}\frac{\partial}{\partial r}\left[-\bar{\rho}r\frac{\overline{v'^3}}{2}-\bar{\rho}r\frac{\overline{v'w'^2}}{2}-\bar{\rho}r\frac{\overline{u'^2v'}}{2}\right] \quad (6.4\text{ c})$$

$$+\frac{1}{\bar{\rho}}\frac{\partial}{\partial x}\left[\mu\frac{\partial k}{\partial r}\right]+\frac{1}{\bar{\rho}r}\frac{\partial}{\partial r}\left[\mu r\frac{\partial k}{\partial r}\right]+\left[\frac{\mu}{\bar{\rho}}\frac{\overline{v'^2}}{r^2}+\frac{\mu}{\bar{\rho}}\frac{\overline{w'^2}}{r^2}\right] \quad (6.4\text{ d})$$

$$+\frac{1}{\bar{\rho}}\frac{\partial}{\partial x}[-\overline{u'p'}\,]+\frac{1}{\bar{\rho}r}\frac{\partial}{\partial r}[-r\overline{v'p'}] \quad (6.4\text{ e})$$

$$-\frac{\mu}{\bar{\rho}}\left[\overline{\left(\frac{\partial v\prime}{\partial r}\right)^2}+\overline{\left(\frac{\partial w\prime}{\partial r}\right)^2}+\overline{\left(\frac{\partial u\prime}{\partial r}\right)^2}+\overline{\left(\frac{\partial v\prime}{\partial x}\right)^2}+\overline{\left(\frac{\partial w\prime}{\partial x}\right)^2}+\overline{\left(\frac{\partial u\prime}{\partial x}\right)^2}\right] \quad (6.4\text{ f})$$

Where U, V and W are the mean velocity components in axial, radial, and azimuthal direction, respectively, $\bar{\rho}$ is the mean fluid density which is approximately 1.18 kg/m^3, μ is the dynamic viscosity which equals 1.8462 X 10^{-5} kg/ms. The convection of turbulent kinetic energy is represented in equation (6.4 a), equation (6.4 b) assimilates the production of turbulent kinetic energy, while equation (6.4 c) is called turbulent diffusion of kinetic energy. Equation (6.4 d) represents the viscous diffusion of turbulent kinetic energy, while (6.4 e) is the pressure diffusion of turbulent kinetic energy, the combination of equations (6.4 d) and (6.4 e) give the diffusion of turbulent kinetic energy, finally the last equation (6.4 f) represents the viscous dissipation of turbulent kinetic energy.

All terms are calculated numerically except the pressure diffusion terms (6.4 e), since it can be neglected without incurring any significant error as their magnitudes are considerably small when compared with other terms [**45**]. Equation (6.4 f) is calculated by balancing the equation, also some terms of the equation are not measured, and valid assumptions are made to account for them, $\overline{v'w'}=\overline{u'w'}$, and $\overline{v'w'^2}=\overline{u'w'^2}$. All terms are normalized by U_o^3/H. The equation is applied for 0.5 swirler, it is solved using central difference method, thus, the kinetic turbulent terms are calculated at all data location except at the

boundaries (i.e. at x/H=0.38 and 8, and r/R=6 and 9). Thus, equation 6.4 becomes:

$$U_{i,j}\frac{k_{i+1,j}-k_{i-1,j}}{\Delta x}+V_{i,j}\frac{k_{i,j+1}-k_{i,j-1}}{\Delta r}= \quad (6.5\text{ a})$$

$$-\left[\overline{v'^2}_{i,j}\frac{V_{i,j+1}-V_{i,j-1}}{\Delta r}+\overline{u'v'}_{i,j}\frac{U_{i,j+1}-U_{i,j-1}}{\Delta r}+\overline{u'v'}_{i,j}\frac{V_{i+1,j}-V_{i-1,j}}{\Delta x}+\overline{u'^2}_{i,j}\frac{\bar{U}-U_{i-1,j}}{\Delta x}+\right.$$

$$w'2i,jVi,jri,j+u'w'i,jWi+1,j-Wi-1,j\Delta x+u'w'i,jWi,j+1-Wi,j-1\Delta r+u'w'i,j$$

$$Wi,jri,j \quad (6.5\text{ b})$$

$$+\frac{1}{\bar{\rho}\Delta x}\left[-\bar{\rho}\frac{\overline{u'v'^2}_{i+1,j}-\overline{u'v'^2}_{i-1,j}}{2}-\bar{\rho}\frac{\overline{u'w'^2}_{i+1,j}-\overline{u'w'^2}_{i-1,j}}{2}-\bar{\rho}\frac{\overline{u'^3}_{i+1,j}-\overline{u'^3}_{i-1,j}}{2}\right]+$$

$$\frac{1}{\bar{\rho}r_{i,j}\Delta r}\left[-\bar{\rho}\left(r_{i,j+1}-r_{i,j-1}\right)\frac{\overline{v'^3}_{i,j+1}-\overline{v'^3}_{i,j-1}}{2}-\right.$$

$$\rho ri,j+1-ri,j-1u'w'2i,j+1-u'w'2i,j-12-\rho ri,j+1-ri,j-1u'2v'i,j+1-u'2v'i,$$

$$j-12 \quad (6.5\text{ c})$$

$$+\frac{1}{\bar{\rho}\Delta x}\left[\mu\frac{\left(k_{i,j+1}-k_{i,j-1}\right)_{i+1,j}-\left(k_{i,j+1}-k_{i,j-1}\right)_{i-1,j}}{\Delta r}\right]+$$

$$\frac{\partial}{\bar{\rho}r_{i,j}\Delta r}\left[\mu\left(r_{i,j+1}-r_{i,j-1}\right)\frac{\left(k_{i,j+1}-k_{i,j-1}\right)_{i,j+1}-\left(k_{i,j+1}-k_{i,j-1}\right)_{i,j+1}}{\Delta r}\right]+\left[\frac{\mu}{\bar{\rho}}\frac{\overline{v'^2}_{i,j}}{r^2{}_{i,j}}+\frac{\mu}{\bar{\rho}}\frac{\overline{w'^2}_{i,j}}{r^2{}_{i,j}}\right] \quad (6.5\text{ d})$$

Where i,j start from 2 to N-1, $\Delta x=x_{i+1,j}-x_{i-1,j}$ and $\Delta r=r_{i,j+1}-r_{i,j-1}$.

Figure 6.5 and figure 6.6 show the distribution of experimental and ANN production term, respectively. As shown in both figures, there are two positive and one negative peaks, the positive peaks are located are initiated at the inlet of the combustion chamber, the larger one is at x/H=1, approximately, and the other one is at x/H=2, the negative peak is found between the centerline and the highest positive peak, it is created due to CTRZ. Positive values indicate energy gains, and negative ones indicate energy loss, this shows that swirler enhances the production of TKE. ANN accomplishes to smoothening the surface and join between peaks to obtain a continuous presentation of the surface.

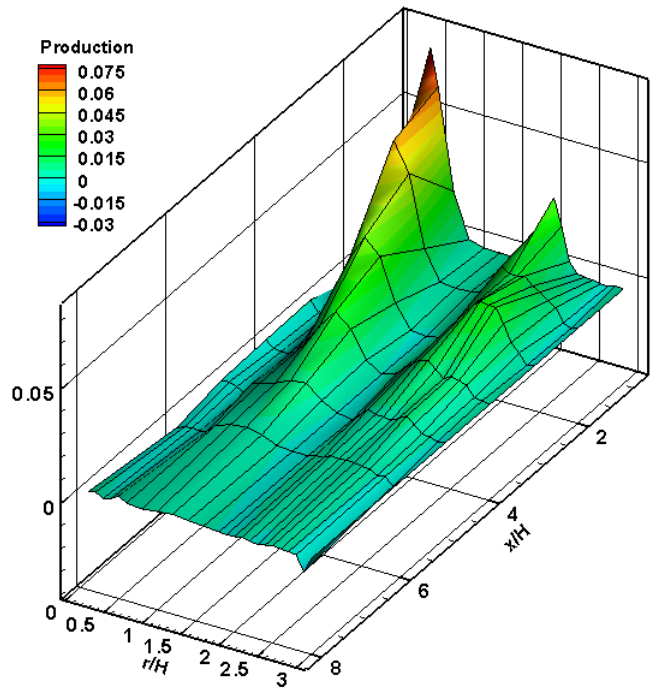

Figure 6.5 Experimental distribution of normalized production term of turbulent kinetic energy

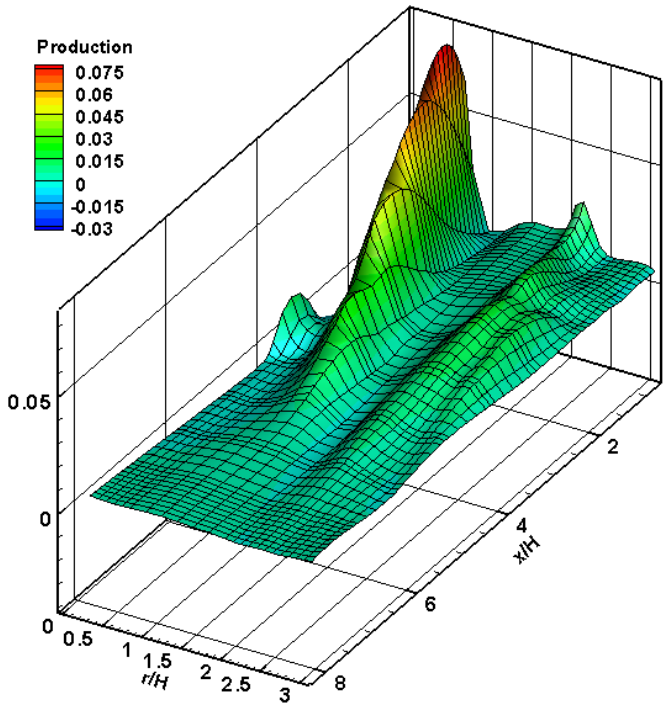

Figure 6.6 ANN distribution of normalized production term of turbulent kinetic energy

Similarly, figure 6.7 shows the distribution of convection term for experimental data, while figure 6.8 is for ANN. The convection has small peaks around the step plane and they diminish downstream of the reattachment point, which means energy is convected. The reattachment point is located at x/H=6.

The introduction of the swirler creates another peak, which is located between the centerline and the step until a distance of x/H=3, and merges with the other peak to form a larger size one that covers a big portion of the combustor.

This observes an increment in energy transportation and distribution. Also the convection is initiated as an energy loss, before it becomes energetic gain just few step after the starting point. The magnitude of the peaks after reattachment, however, is less compared to their values before reattachment.

The plot produced by ANN is similar to the experimental one, since most main features are presented. However, the two peaks that are created at the inlet are merged together, and they form one peak at the reattachment point. This is not the real case because both peaks are created and vanish separately.

On the other hand, ANN predicted the characteristics of the convection term correctly downstream after x/H=4. As can be seen, the energy is convected uniformly until it reaches zero as moving further towards the exit.

Also, the convection term is zero near the shear layer, this can be seen clearly in both experimental and ANN distributions, except small peaks which are generated incorrectly at x/H=2 and 4, because this profile is affected by the weights of the previous locations at the same profile, from here, the weights that correspond to the neurons which are responsible on implementing the function are modified incorrectly which leads to inaccurate predictions.

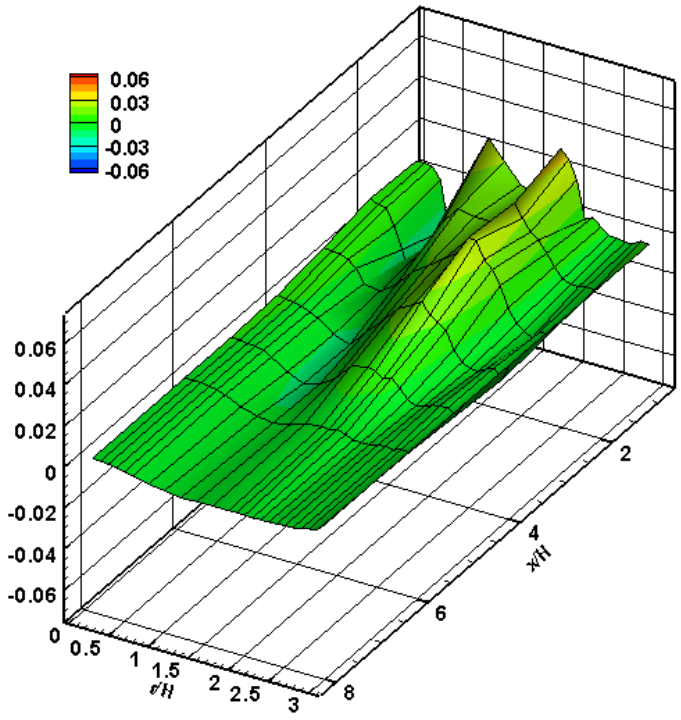

Figure 6.7 Experimental distribution of normalized convection term of turbulent kinetic energy

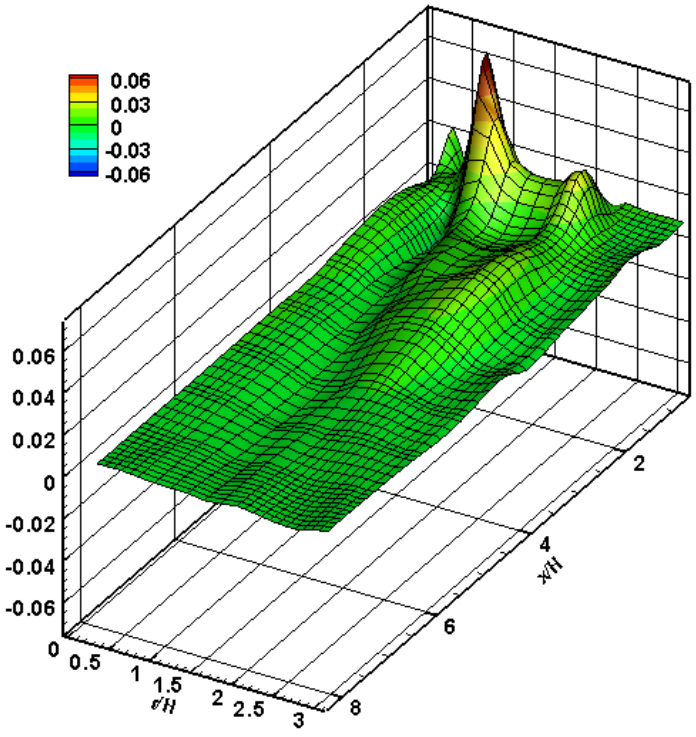

Figure 6.8 ANN distribution of normalized convection term of turbulent kinetic energy

The distribution of diffusion of turbulent kinetic energy, which is shown in figure 6.9 and figure 6.10, is completely undistributed uniformly, as bumps appear and vanish suddenly before they start once again at the next step. ANN manages to solve this discontinuity by joining these peaks and reduce them to reasonable values as should be for diffusion term peaks. The total diffusion term redistributes the energy in the vicinity of the shear layer from the centers to the outer parts of the shear layer.

Despite of the inability of showing the real value of the peak at the centerline, ANN is able to locate the location of all peaks correctly, as the size of these peaks appears below correctly. However, the trend of the diffusion at the shear layer are not presented accurately in the ANN plot, ANN predicts a uniform distribution there instead. This is because of the fact that ANN join between all profiles continuously.

This occurrence is primarily due to swirl introduction which proves the importance of stirring the flow at the inlet of the combustor. The intensity of energy diffusion at the step plane and the boundary decreases with increasing streamwise distance.

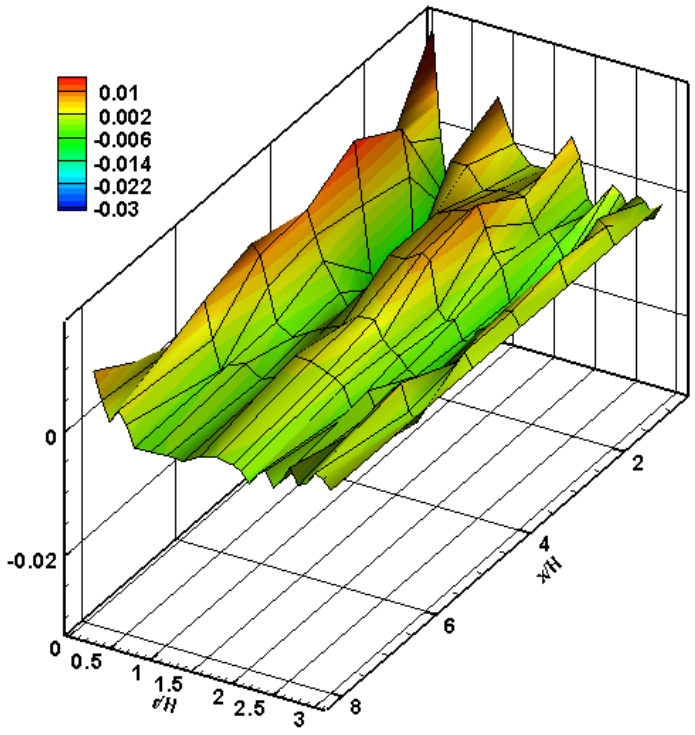

Figure 6.9 Experimental distribution of normalized diffusion term of turbulent kinetic energy

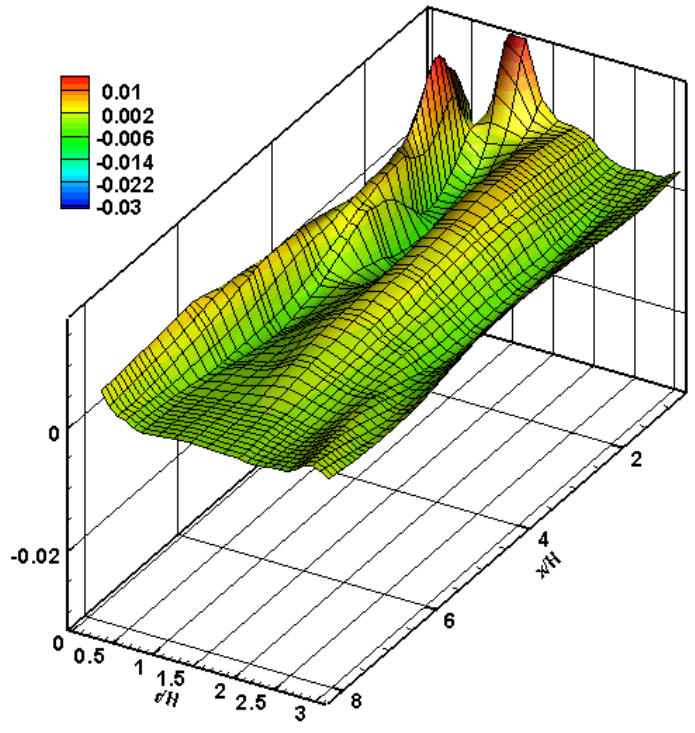

Figure 6.10 ANN distribution of normalized diffusion term of turbulent kinetic energy

The total viscous dissipation term is calculated by balancing the TKE equation. As shown in figure 6.11 and figure 6.12, the crisps at the boundary layer are en suited after utilizing ANN, while the small rises between profiles are smoothened and the peaks at the inlet of the combustor are clearly appear as they should be.

There are mainly two peaks at the inlet of the combustor; one indicates energy gain while the other is a loss one, the swirler initiates a negative peak, but soon it opposes the sign while obtaining the same magnitude as going little further from the inlet. These peaks dissipate as moving through the axial direction of the combustor to vanish at the reattachment point. Two interesting reversal energetic sign occur at the midpoint between the inlet and the reattachment zone in the axial direction, and between the centerline and the boundaries in the radial direction, and disappear as they reach the reattachment point. Mostly, the viscous dissipation makes negative contribution to the TKE, and portrays a similar but opposite distribution as the production term.

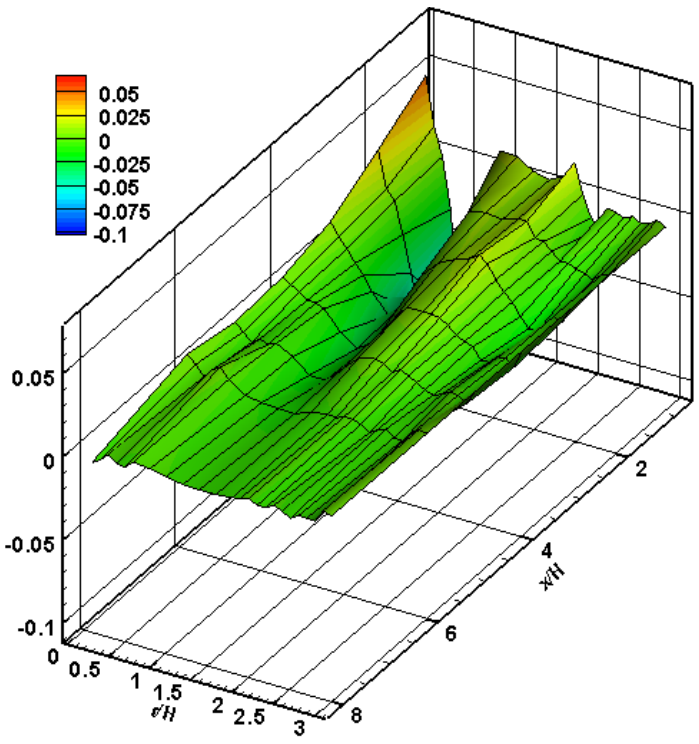

Figure 6.11 Experimental distribution of normalized viscous dissipation term of turbulent kinetic energy

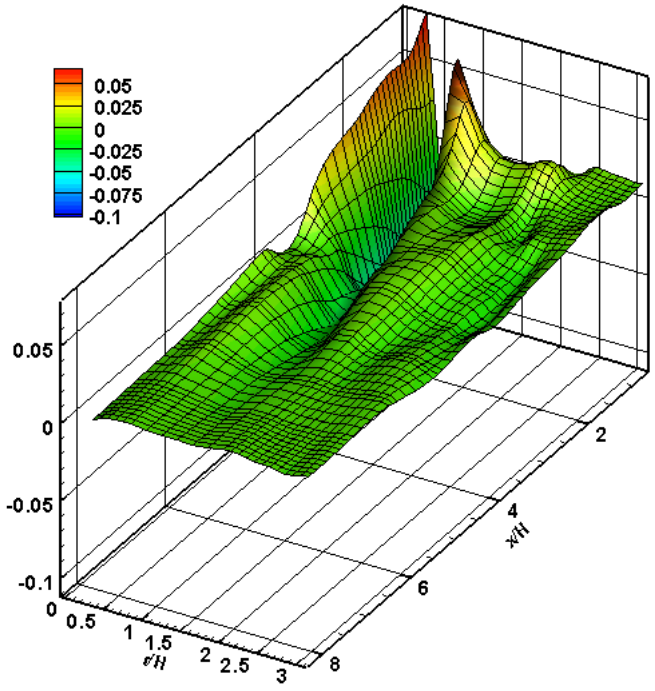

Figure 6.12 ANN distribution of normalized viscous dissipation term of turbulent kinetic energy

CHAPTER 7

PREDICTION OF DATA FOR A DIFFERENT SWIRL NUMBER

Perhaps the ability of generating new swirlers which have not been measured experimentally is one of the most beneficial outcomes from this study; this can be obtained by training the ANN structure on all swirlers but one, which is chosen as testing set. In this case, the inputs of the network are 3; which are: x, r, and swirl number. Note in this case that all radial directions are shifted to the same limits, (i.e. from 0-3) to facilitate ANN in configuring its weights properly. The network is trained on 0, 0.3, and 0.5 swirler, while 0.4 swirler is chosen to be the testing set, since its data points are located closely to the rest of the other swirlers (i.e. 0.3 and 0.5). The predictions are achieved for $U, V, W, u'_{RMS}, v'_{RMS}$, and w'_{RMS}, the higher order components are durable to predict, because of the high non linearity in their trends. Once the network successfully implemented the desired output, a whole set of new swirl number can be generated, in this study, however, one swirl number is presented here, which is at 0.35 swirler.

Table 7.1 summarizes the NMSE and CC values after testing the network on 0.4 swirler data set, even though the correlation coefficient values are low in compare with previous values, they are still valid to produce set of data at new swirl number with expected distributions of the components.

Table 7.1 NMSE and CC values of testing 0.4 swirler for each component

Component	Best Network	NMSE	CC
$\boldsymbol{U}$	GFF (19 Neurons)	0.156379	0.926021
$\boldsymbol{V}$	GFF (11 Neurons)	0.460423	0.752776
$\boldsymbol{W}$	GFF (18 Neurons)	0.390408	0.82252
$\boldsymbol{u'_{RMS}}$	GFF (18 Neurons)	0.451576	0.789185
$\boldsymbol{v'_{RMS}}$	GFF (18 Neurons)	0.382483	0.856094
$\boldsymbol{w'_{RMS}}$	GFF (18 Neurons)	0.560318	0.784616

Figure 7.1Figure 7.3 show the near field distributions of axial, radial, and tangential velocity components, respectively, while figure 7.4-Figure 7.6 show the near field distributions of axial, radial and tangential fluctuating velocity components, respectively.

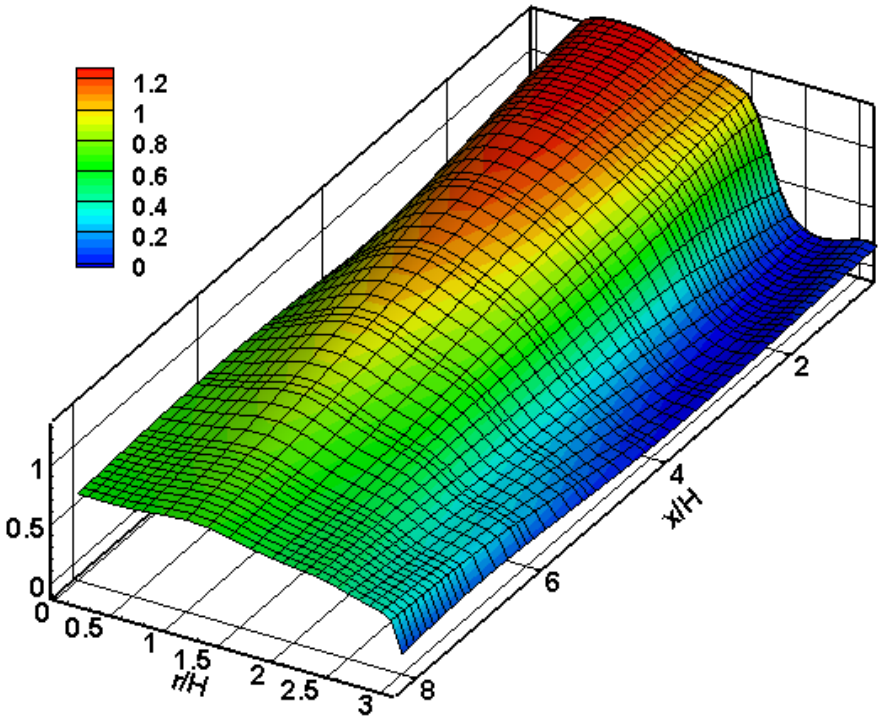

Figure 7.1 Distribution of U/U_o at 0.35 swirler

Figure 7.1 shows the distribution of the non-dimensional axial velocity component generated by ANN. The used network is GFF with 19 processing elements, which is the same network that is used in reconstructing and producing the axial profiles for 0.5 swirl.

It is known that the swirler is responsible on decreasing the velocity of the flow at the inlet, this can be seen clearly from the legend, since the peak value reaches 1.2, while the maximum value of the axial velocity is 0.9 when S_n=0.5.

Meanwhile, the swirler is also decreases the size of the peak at the inlet because it generates CTRZ, this decreases the value of the speed near the centerline, while as shown above, the region of the peak covers the combustion area until its amount reduces when reaching the shear layer.

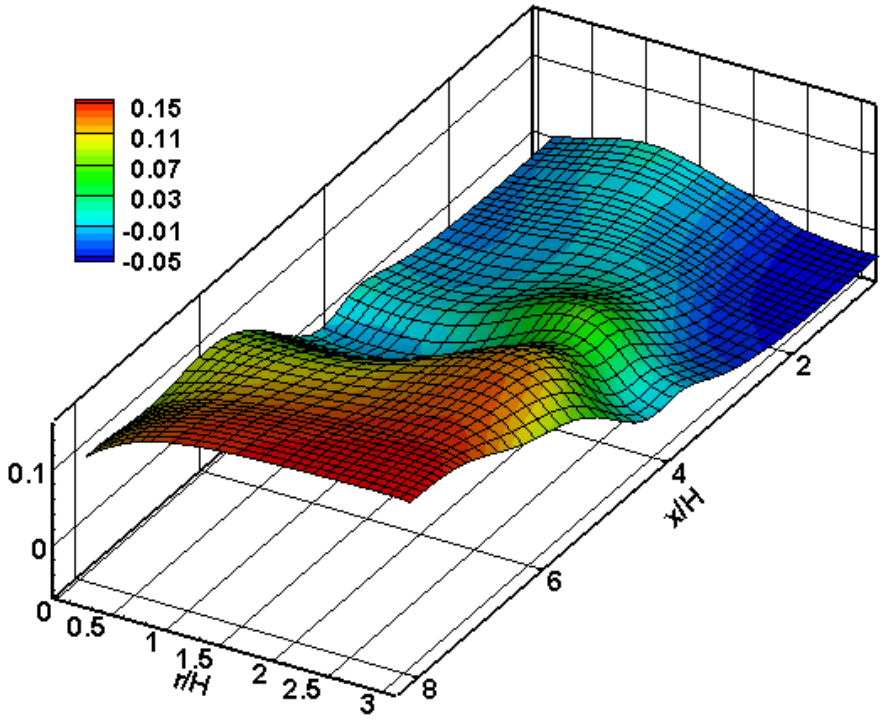

Figure 7.2 Distribution of V/U_o at 0.35 swirler

The distribution of the radial velocity component is presented in figure 7.2, the same network is used in constructing the radial velocity profiles, which is GFF network with 11 neurons. Though the correlation coefficient values obtained from testing the network with the experimental data of the radial velocity at S_n=0.4 are low in compare with the axial ones. ANN successfully managed to show all near field flow characteristics successfully.

The radial velocity of the flow at the inlet is almost zero except at the corner of the combustor, where a reverse flow occurs due to the existence of CRZ. The amount of the speed increases as moving further downstream. Also several peaks appear and die out shortly in the direction of flow speed

increment. Moreover, the increment of radial velocity before x/H=4 is conveyed up, while it conveys down when moving towards the exhaust.

All these features prove the success of ANN in generating the radial profile at 0.35 swirl number, because all these characteristics are presented in 0.3 and 0.4 swirl numbers radial velocities.

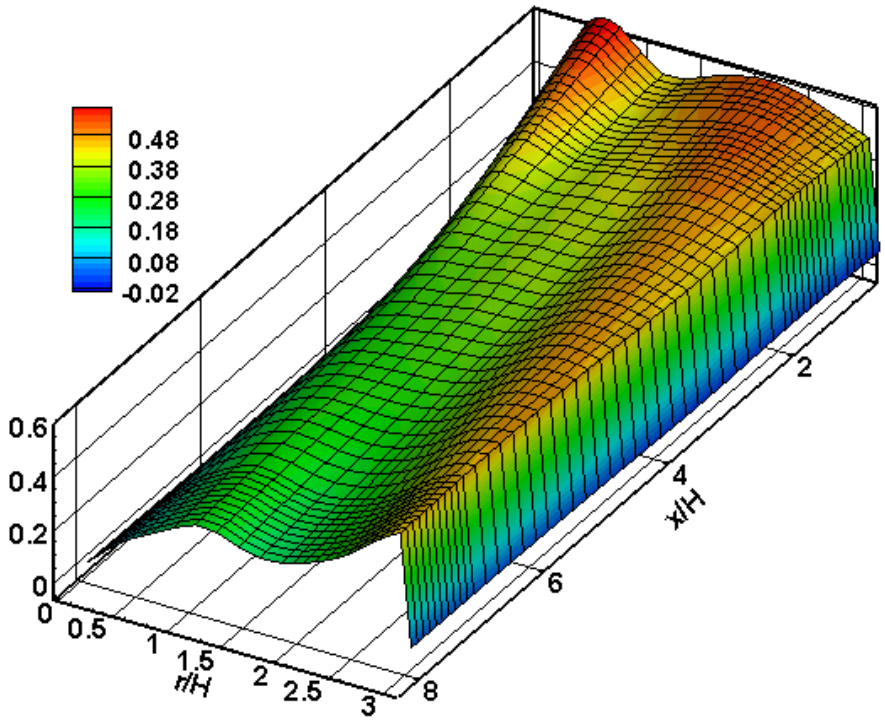

Figure 7.3 Distribution of W/U_o at 0.35 swirler

The tangential velocity component at 0.35 swirler is illustrated in figure 7.3, which is similar to the distribution of the experimental tangential velocity component in figure 5.24 (Chapter 5).

The peaks as expected are located at the entrance of the combustor, near the centerline and the shear layer. The value of the peak located at x/H=0.75 decreases shortly before reaching x/H=2, while the other peak preserve its value as moving downstream.

ANN also generated the profiles at the centerline and the shear layer correctly, since zero speed values obtained there. Note the sudden change of the speed near the wall.

ANN also shows the fact that the tangential velocity becomes uniformly distributed and covers the whole combustion zone as moving downstream towards the exhaust, which is the same case as in 0.3 and 0.4 swirl numbers.

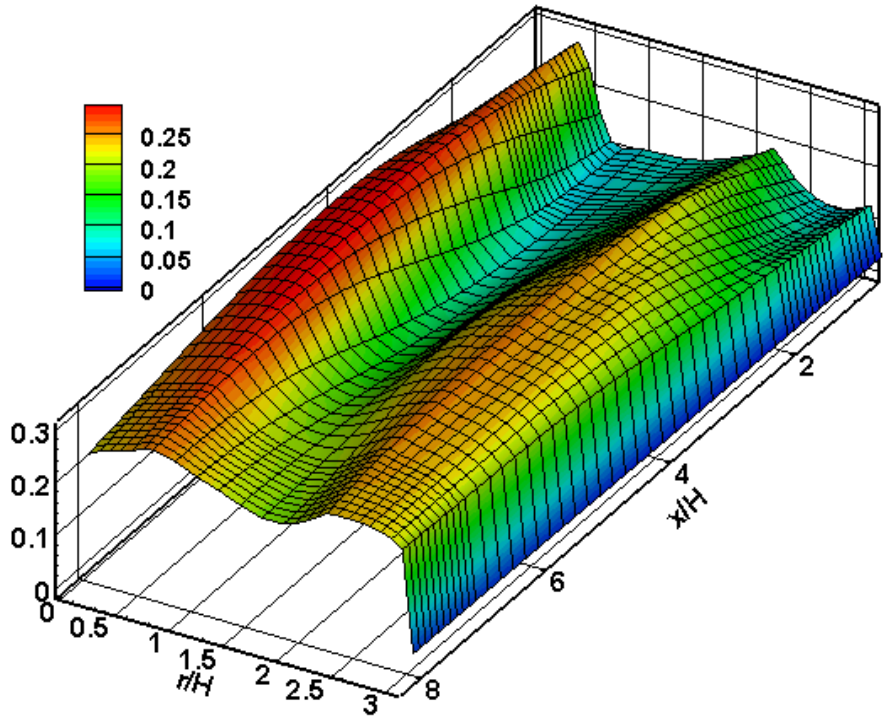

Figure 7.4 Distribution of u'_{RMS}/U_o at 0.35 swirler

The structure of GFF network that is used to generate the fluctuating axial velocity component consists of the same number of neurons that is used to build all fluctuating components, which is 18 neurons. The distribution of the normal Reynolds stress in the axial plane for 0.35 swirler is shown in figure 7.4. The properties of the axial fluctuating velocity generated by ANN are similar to the experimental distribution at 0.3 and 0.4 swirlers.

A thin film peak is generated due to the existence of CTRZ just after the inlet and covers the whole centerline, however, the peak moves a little towards

the wall as going downstream until it reaches r/H=0.6 at x/H=8. The other peak is bounded between x/H=3 and 7.6, approximately, and between r/H=2.3 and 2.7. Note that no negative values exist in the plot, which shows the success of utilizing ANN to predict the flow field characteristics of the axial fluctuating component.

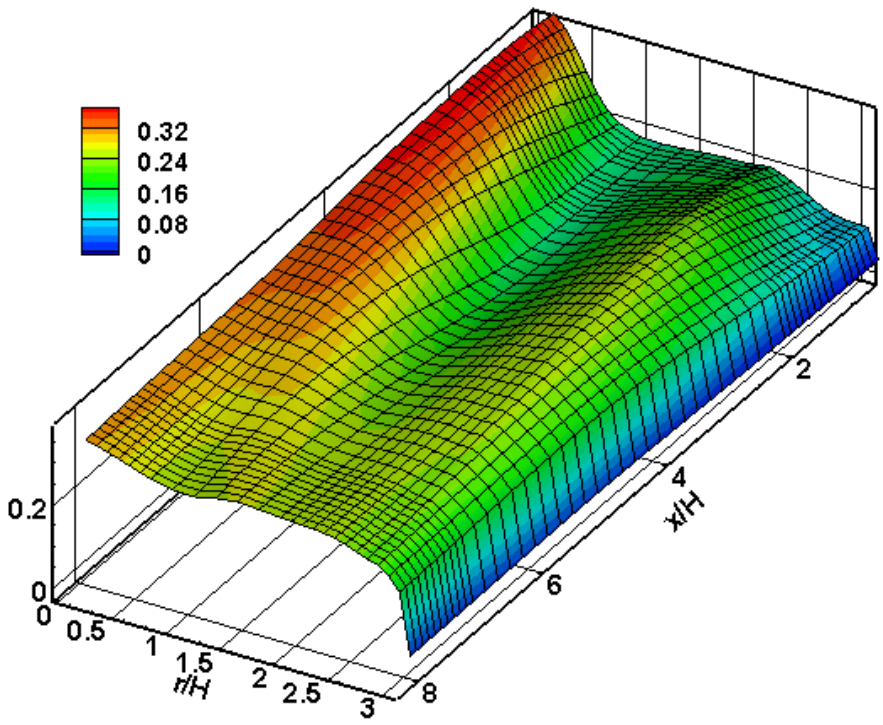

Figure 7.5 Distribution of v'_{RMS}/U_o at 0.35 swirler

The distribution of the radial fluctuating velocity, which is presented in figure 7.5, is constructed using GFF network with 18 neurons; this is the same as all fluctuating components. The correlation coefficient value of testing the network with all 0.4 swirler profiles is 0.85, which gives a very good indication of the ability to generate the radial fluctuating component at new swirl number.

It is known that the peak of the radial fluctuating components is initiated at the inlet and expands around the centerline, this is correctly generated by ANN since the peak is generated at the inlet and increase in size till it reaches r/H=0.75, and starts to decrease after x/H=5.

Also the values at the shear layer are generated accurately, since all values at the wall are very close to zero, while the flow characteristics of the radial fluctuating component are uniform between the centerline and the middle shear layer.

In similar manner, the tangential fluctuating component is built with the same ANN structure. The correlation coefficient value obtained of testing 0.4 data is 0.78, which is acceptable since a huge number of data is tested and the general shape of the distribution is correct.

As expected in figure 7.6, which illustrates the tangential fluctuating velocity component for 0.35 swirl number, a very thin film peak is formed around the centerline and vanishes approximately at x/H=5, also zero values are predicted at the shear layer, while the flow characteristics of the tangential fluctuating velocity become stable and uniform after x/H=5.

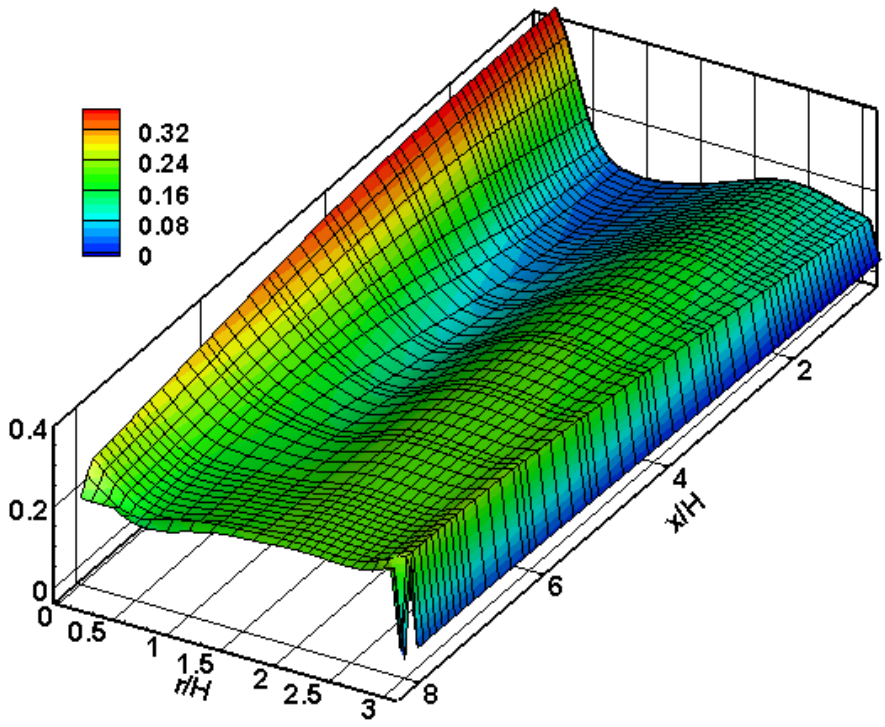

Figure 7.6 Distribution of w'_{RMS}/U_o at 0.35 swirler

The results acquired from the distribution of turbulence statistics at 0.35 swirler are similar to the ones at 0.3 and 0.4 swirlers, therefore, ANN shows potential production of flowfield characteristics in an axisymmetric sudden-expansion dump combustor model, it encourages advancing the utility of ANN in ornamental experimental results in analogous systems. Also predictions can be accomplished for all swirlers between 0-0.5 swirl numbers.

These results show the ANN interest which transforms the discrete flowfield characteristics measured experimentally into a continuous distribution defined on the whole domain. Despite the complex behavior of the swirling flow, ANN handled to fine-mesh the distribution of turbulence statistics with very diminutive detachments.

CHAPTER 8

CONCLUSIONS AND RECOMMENDATIONS

8.1 Conclusions

ANN is exploited to predict flow field turbulence characteristics of an axisymmetric sudden-expansion dump combustor model measured using a two component laser Doppler velocimeter. ANN is employed to prognosticate experimental measurements of mean velocities, Reynolds normal and shear stresses, and triple products.

Three networks are elected to accomplish this task, which are generalized feedforward, radial basis function, and CANFIS networks. These networks are configured and structured for several parameters in order to acquire the most efficient network. Then they are compared with each other to find the most suitable network structure to be used for predicting the behavior of the desired components. For most turbulence statistics, generalized feedforward manages to implement the turbulence statistics successfully with correlation coefficient values higher than 0.8 for all profiles.

ANN is then used to reconstruct the turbulence statistics as well as producing extra profiles to diminish the mesh size of the distributions of the flow field parameters, in addition to augment the comprehension of the flowfield characteristics of a swirl flow. ANN appears to be an efficient tool to accurately represent any flow field characteristics of a swirling flow.

Moreover, ANN is applied to calculate the stream function and turbulent kinetic energy terms; the outcome is promising in view of the fact that ANN managed to improve the visualization of these functions by reducing the amount of noise and uniformly attaching the peaks between experimental profiles as well as getting rid of voids whether they are located at the boundaries or at the centerlines.

One crucial profit gained from ANN, is its ability to generate an entire set of data for any swirl number between the provided experimental ones. A complete set of data is generated for velocity products and their fluctuating components at 0.35 swirler. The obtained results encourages utilizing ANN to generate data for all velocities and Reynolds normal stress at any swirl number in the range between 0 and 0.5

8.2 Recommendations

Though the proposed method resulted in very good accuracy rate, the technique has been validated using relatively small testing set. Increasing the testing data set will result in more general and accurate results. The proposed technique was implemented on three networks. To increase confidence in these results, similar simulations should be performed using different networks. Besides the numerical prediction can be employed to solve different equations that still remain without decisive solution.

One immense achievement can be approached in such field by combining the obtained results with simulated models done by computational fluid dynamics to completely identify the problem over a wide range of conditions and data sets.

REFERENCE LIST

[1] A. Gupta, D. Lilley, and N. Syred, *Swirl flows*. Tunbridge Wells, UK: Abacus Press, 1984.

[2] G. Batchelor, *An Introduction to Fluid Dynamics*. Cambridge, UK: Cambridge University Press, 1967.

[3] P. Dellenback, D. Metzger, and G. Neitzel, "Measurement in Turbulent Swirling Flow Through an Abrupt Axisymmetric Expansion," *AIAA Journal*, vol. 26, no. 6, pp. 669–681, 1988.

[4] W. Hallett and R. Günther, "Flow and Mixing in Swirling Flow in a Sudden Expansion," *Canadian Journal of Chemical Engineering*, vol. 62, pp. 149-155, 1984.

[5] E. Fernandes, M. Heitor, and S. Shtork, "An Analysis of Unsteady Highly Turbulent Swirling Flow in a Model Vortex Combustor," *Experiments in Fluids*, vol. 40, no. 2, pp. 177-187, 2006.

[6] S. Ahmed and A. Nejad, "Velocity Measurements in a Research Combustor," *Experimental Thermal and Fluid Science Journal Part I. Isothermal Swirling Flow*, vol. 5, pp. 162-174, 1992.

[7] S. Chowdhury and M. Mayeed, "Effect of Expansion Angle on Turbulent Swirling Flow," *Indian Journal of Engineering and Materials Sciences*, vol. 6, pp. 323-329, 1993.

[8] W. Hallett and D. Toews, "The Effect of Inlet Conditions and Expansion-Ratio on The Onset of Flow Reversal in Swirling Flow in a Sudden Expansion," *Experiments in Fluids*, vol. 5, no. 2, pp. 129-133, 1987.

[9] M. Escudier and J. Keller, "Recirculation in Swirling Flow: a Manifestation of Vortex Breakdown," *AIAA Journal*, vol. 23, no. 1, pp. 111-116, 1985.

[10] M. Escudier, A. Nickson, and R. Poole, "Influence of Outlet Geometry on Strongly Swirling Turbulent Flow Through a Circular Tube," *Physics of Fliuids*, vol. 18, no. 125103, 2006.

[11] M. Breuer, "A Challenging Test Case For Large Eddy Simulation: High Reynolds Number Circular Cylinder Flow," *International Journal of Heat Fluid Flow*, vol. 21, no. 5, pp. 648-654, 2000.

[12] S. Lakshmipathy and S. Girimaji, "Partially Averaged Navier–Stokes (PANS) Method for Turbulence Simulations: Flow Past a Circular

Cylinder," *Journal of Fluids Engineering*, vol. 132, no. 12, pp. 1-11, December 2010.

[13] A. Spentzos, G. Barakos, K. Badcock, and B. Richards, "Modeling 3D Dynamic Stall using CFD and Neural Networks," vol. 44, no. 1071, 2006.

[14] W. McCulloch and W. Pitts, "A Logical Calculus of the Ideas Immanent in Nervous Activity," in *Bulletin of Mathematical Biophysics.*, 1943, ch. 5, pp. 115-133.

[15] P. Panigrahi, M. Dwivedi, V. Handelwal, and M. Sen, "Prediction of Turbulence Statistics Behind a Square Cylinder Using Neural Netowrks and Fuzzy Logic," *Fluid Engineering*, vol. 125, March 2003.

[16] J. Pruvost, J. Legrand, and P. Legentilhomme, "Three-Dimensional Swirl Flow Velocity-Field Reconstruction Using Neural Network with Radial Basis Functions," vol. 123, December 2001.

[17] S. Ahmed and H. El Kadi, "Dump Combustor Swirling Flow Reconstruction Using Neural Network," in *AM-PT 1 038*, vol. 14, 2010.

[18] B. Ayhan-Sarac, B. Karlik, T. Bali, and T. Ayhan, "Neural Network Methodology for Heat Transfer Enhancement Data," *International Journal of Numerical Methods for Heat and Fluid flow*, vol. 17, no. 8, 2007.

[19] F. Grinstein et al., "Flow Dynamics in a Swirl Combustor," *Journal of Turbulence*, vol. 3, pp. 1-19, 2002.

[20] P. Wang, X. Bai, M. Wessman, and J. Klingmann, "Large Eddy Simulation and Experimental Studies of a Confined Turbulent Swirling Flow," *Physics of Fluids*, vol. 16, no. 9, pp. 3306-3324, 2004.

[21] W. Hallett and R. Günther, "Flow and Mixing in Swirling Flow Expansion Ratio on the Onset of Flow Reversal in Swirling Flow in a Sudden Expansion," in *Experiments in Fluids*, vol. 5, 1984, pp. 129–133.

[22] J. Beer and N. Chigier, *Combustion Aerodynamics*. US: Applied Science Publishers Ltd., 1972.

[23] A. Lefebvre, *Gas Turbine Combustion*. US: Hemisphere Publishing Corporation, 1983.

[24] M. Gupta, B. Linck, and K. Shwani, "Twin-Fluid Atomization and Novel Lifted Swirl-Stabilized Spray Flames," vol. 25, no. 2, March–April 2009.

[25] L. Khezzar, J. Whitelaw, and M. Yianneskis, "Round sudden-expansion flows," in *IMechE 200*, 1986, pp. 447–455.

[26] D. Cole and M. Glauser, "Flying Hot-wire Measurements in Axisymmetric Sudden Expansion," in *Experimental Thermal and Fluid Science 18*, 1998, pp. 150–167.

[27] A. Pereira and F. Pinho, "The Effect of the Expansion Ratio on a Turbulentnon-Newtonian Recirculating Flow," in *Experiments in Fluids 32*, 2002, pp. 458–471.

[28] Z. Husain and A. Hussain, "Axisymmetric Mixing Layer: influence of initial and boundary conditions," *AIAA*, vol. 17, pp. 48–55, 1979.

[29] B. Yang and M. Yu, "The Flow Field in a Suddenly Enlarged Combustion Chamber," *AIAA*, vol. 21, pp. 92–97, 1983.

[30] S. Ahmed, "Velocity Measurements and Turbulence Statistics of a Confined Isothermal Swirling Flow," *Experimental Thermal and Fluid Science*, vol. 17, pp. 256-264, 1998.

[31] M. Ihme, C. Schmitt, and H. Pitsch, "Optimal Artificial Neural Networks and Tabulation Methods for Chemistry Representation in LES of a Bluff-Body Swirl-Stabilized Flame," in *Proceedings of the Combustion Institute*, vol. 32, Michigan, 2009, pp. 1527-1535.

[32] A. Abdel Gawad, "Numerical and Neural Study of the Turbulent Flow around Sharp-Edged Bodies," in *Fluids Engineering Division Summer Meeting*, Quebec, 2002, pp. 1-13.

[33] D. Zhao, S. Qiu, G. Su, and W. Tian, "Prediction of Post-Dryout Heat Transfer in Vertical Annular Channels Using Artificial Neural Network Method," in *International Conference on Nuclear Engineering*, Orlando, 2008, pp. 1-7.

[34] M. Duranton, "Image Processing by Neural Networks," *IEEE Micro*, vol. 16, no. 5, October 1996.

[35] H. Malmgren, M. Borga, and L. Niklasson, *Artificial Neural Networks in Medicine and Biology*. Goteborg, Sweden: Springer, 2000.

[36] A. Barros, A. Mansour, and N. Ohnishi, "Removing Artifacts from Electrocardiographic Signals Using Independent Components Analysis," *Neurocomputing*, vol. 2, no. 1-3, pp. 173-186, November 1998.

[37] B. Kosko, *Neural Networks and Fuzzy Systems*. US: Prentice Hall, 1992.

[38] J. Schalkoff, *Artificial Neural Networks*, 2nd ed. US: Robert McGraw-Hill Inc, 1997.

[39] P. Haley and D. Soloway, "Extrapolation Limitations of Multilayer Feedforward Neural Networks," in *International Joint Conference on Neural Networks*, vol. 4, Baltimore, 1992, pp. 25-30.

[40] H. Vinod and A. Ullah, *Recent Advances in Regression Methods*. US: Marcel Dekker Inc, 1981.

[41] M. Powell, "Radial Basis Functions for Multivariate Interpolation: a Review.," in *Algorithms for Approximation*. Oxford: Clarendon Press, 1987.

[42] Y. Gao, J. Fang, Z. Zhao, and L. Yang, "Application of RBF Network for Forecasting Characteristics of In-Flight Particles by Plasma Spraying," *Advanced Materials Research*, vol. 25, no. 28, pp. 985-988, 2007.

[43] G Camps-Valls et al., "Robust Support Vector Method for Hyperspectral Data Classification and Knowledge Discovery," *Trans. Geosci. Rem. Sens.*, vol. 42, no. 7, pp. 1530–1542, July 2004.

[44] G. Cybenko, "Approximation by Superpositions of a Sigmoidal Function," *Math Control Signal Systems*, vol. 2, pp. 303-314, 1989.

[45] N. Kasagi and A. Matsunaga, "Three-dimensional Particle Tracking Velocimetry Measurement of Turbulence Statistics and Energy Budget in a Backward-facing Step Flow," *International Journal Heat and Fluid Flow*, vol. 16, pp. 477-485, 1995.

[46] A. Abraham, "Artificial Neural Networkds," in *Handbook of Measuring System Design*. US: John Willey & sons, Ltd, 2005, pp. 901-908.

[47] Wikipedia. [Online]. http://en.wikipedia.org/wiki/Combustor

[48] E. Ekstedt, "Triple annular combustor for gas turbine engine," 5323604, 1994.

[49] R. Henderson and W. Blazowski, "Turbopropulsion Combustion Technology," in *Aircraft Propulsion Systems Technology and Design*. Washington DC: AIAA Education Series, American Institute of Aeronautics and As, 1989, ch. 2.

[50] Schilling and C. Jan, "Dome Assembly for a Multiple AnnularCombustor,"

5630319, 1997.

[51] M. Dong and D. Lilley, "Inlet Velocity Profile Effects on Turbulent Swirling Flow Predictions," *J Propul. Power*, pp. 155-160, 1994.

[52] J. Mattingly, W. Heiser, and D. Pratt, "Engine Component Design: Combustion Systems," in *Aircraft Engine Design*, 2nd ed.: AIAA Education Series Reston, 2002, ch. 9.

[53] R. Flack, *Fundementals of Jet Propulsion with Applications*, Cambridge University Press, Ed. New York: Cambridge Aerospace Series, 2005.

[54] S. Pope, *Turbulent Flows*. Cambridge, UK: Cambridge University Press, 2003.

[55] B. Massey and J. Ward-Smith, *Mechanics of Fluids*, 7th ed. UK: Nelson Thornes, 1998.

[56] R. Durrett, W. Stevenson, and H. Thompson, "Radial and Axial Turbulent Flow Measurements with an LDV in an Axisymmetric Sudden Expansion Air Flow," *Transactions of the ASME—Journal of Fluids Engineering*, vol. 110, pp. 367–372, 1998.

[57] M. Sommerfeld and H. Qiu, "Detailed Measurements in a Swirling Particulate Two-Phase Flow by a Phase-Doppler Anemometer," *International Journal of Heat and Fluid Flow*, vol. 12, no. 1, pp. 20-28, 1991.

[58] W. Devenport and E. Sutton, "An Experimental Study of Two Flows through an Axisymmetric Sudden Expansion," *Experiments in Fluids*, vol. 14, pp. 423–432, 1993.

[59] L. Khezzar, "Velocity Measurements in the Near Field of a Radial Swirler," *Experimental Thermal and Fluid Science*, vol. 16, pp. 230–236, 1998.

[60] L.X. Zhou, Y. Li, T. Chen, and Y. Xu, "Studies on the Effect of Swirl Numbers on Strongly Swirling Turbulent Gas–Particle Flows Using a Phase-Doppler Particle Anemometer," *Powder Technology*, vol. 112, pp. 79-86, 2000.

[61] N. Furuichi, Y. Takeda, and M. Kumada, "Spatial Structure of the Flow through an Axisymmetric Sudden Expansion," *Experiments in Fluids*, vol. 34, pp. 643–650, 2003.

[62] C. Tinney, M. Glauser, E Eaton, and J. Taylor, "Low Dimensional

Azimuthal Characteristics of Suddenly Expanding Axisymmetric Flows," *Journal of Fluid Mechanics*, vol. 567, pp. 141–155, 2006.

[63] K. Hammad, M. Ötügen, and E. Arik, "A PIV study of the laminar axisymmetric sudden expansion flow," *Experiments in Fluids*, vol. 26, no. 3, pp. 266-272, 1999.

[64] C. Lefebvre and J. Principe, NeuroSolutions, 2005, NeuroDimension Inc., Copyright 1994-2005.

[65] Y. Cengel and M. Boles, *Thermodynamics: An Engineering Approach*, 7th ed. US: McGraw-Hill Science, Engineering Math, 2005.

[66] A. Bejan, *Advanced Engineering Thermodynamics*, 3rd ed. US: Wiley, 2006.

[67] C. Lee, *Fuzzy Logic in Control Systems: Fuzzy Logic Controller*. US: IEEE Transacts, 1990.

[68] L. Zadeh, "Fuzzy sets," in *Information and Control*. US: Elsevier Inc, 1965, ch. 8, pp. 338-353.

[69] L. Zadeh, *The Concept of a Linguistic Variable And its Application to Approximate Reasoning*. US: Information Sciences, 1975, vol. 8 & 9.

[70] H. Zimmermann, *Fuzzy set theory and its applications*. Boston: Kluwer Academic Publishers, 2001.

[71] E. Mamdani, *Applications of Fuzzy Algorithms For Simple Dynamic Plant*. US: Proc. IEEE, 1974, vol. 21.

[72] S. Haykin, *Neural Networks: A Comprehensive Foundatoin*. New York, US: Macmillan, 1994.

[73] J. Hertz, A. Krogh, and R. Palmer, *Introduction to the Theory of Neural Computation*. Reading, MA: Addison-Wesley, 1991.

[74] M. Zurada, *Inroduction to Artificial Neural Systems*. Boston, MA: PWS Publishing, 1992.

APPENDIX A: ARTIFICIAL NEURAL NETWORKS

Neural Network Learning Algorithms

After this brief introduction on some ANN, it is elementary to be familiar with learning rules in order to model any system using ANNs **[**46**]**.

Learning is the process of modifying network parameters to improve the performance of the network, there are many algorithms that can be utilized to train the network and obtain results, such as step rule, momentum rule, Hebbian learning algorithm, Levenberg–Marquardt algorithm (LM), perceptron learning rule and delta bar delta rule. Before going through learning algorithms review, it is essential to identify two learning modes:

1. Online mode: in this mode, the weights for each input data sample are updated and modified after each sample
2. Batch mode: here the weight update is computed for each input sample passing through all training data, this is called an epoch. At the end of each epoch, all contributions are added, and then weights are modified with the contributed value.

Since weights modifying comes after each epoch in batch mode, all weights will follow the same trend, hence approaching the desired values more closely.

Generally, what happens in training is calculating errors between guesses of weights at each run, and values obtained from training data, and then adjusting weights values based on the calculated error. The overall error is computed by taking the average of all squared errors E, then the weights are updated by this value, as shown on the following equation:

$$\Delta w_{ij}(n) = -\eta^* \frac{\delta E}{\delta w_{ij}} + \alpha^* \Delta w_{ij}(n-1) \tag{A.1}$$

Where η is the learning rate and α is the momentum.

The momentum term determines the effect of previous weight changes on the current error calculations, a right initial guesses for α and η effect dramatically on the speed of learning. A summarized discussion of some learning algorithms is introduced below:

1. Hebbian Learning

The most famous learning algorithm, it is similar the behavior of human's nervous system. As Hebb stated: "When an axon of cell A is near enough to excite a cell B and repeatedly or persistently take part in firing it, some metabolic change takes place in one or both cells such that A's efficiency, as one of the cells firing B, is increased".

Most learning algorithms are derived from Hebbian learning. The whole idea is based on neurons' activities, so if two connected neurons are active at the same time, the connection between them should strengthen. From there, the weight update can be written in the following formula:

$$w_i(new) = w_i(old) + x_i y \tag{A.2}$$

Where x is the input, y is the desired output and w is the weight.

What should be considered when dealing with Hebbian learning is to normalize the data, so the weights can be strengthened with bonds.

2. Perceptron Learning Rule

A perceptron is defined as a layer that can be trained to produce a correct vector from input vector by adjusting weights and biases correctly. Fig. A.1 shows a flowchart on how to apply this rule. A desired output is denoted by $d(k)$, where $d(k)$ is usually -1 or +1, η is the learning rate.

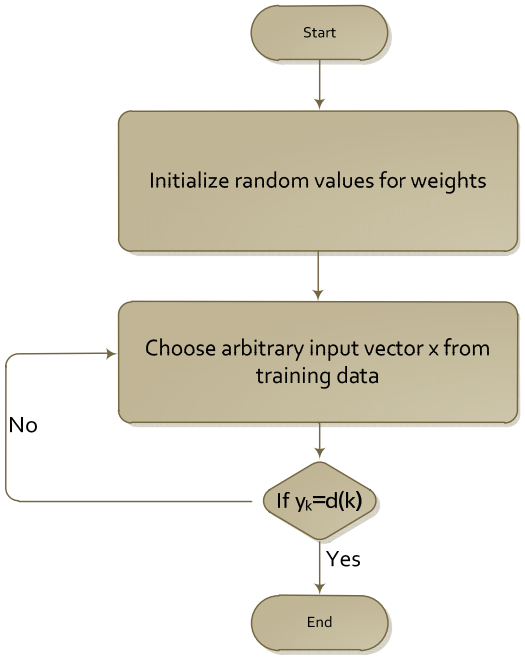

Fig. A.1 Perceptron rule algorithm

3. Backpropagation Learning

This learning algorithm starts from output layer to hidden layer weights, then hidden layer to input layer weights (back direction), by taking the negative of the partial derivative for the error of the network for each weight $\frac{\delta E}{\delta w_{ij}}$, and then add it to its corresponding weight, this will reduce the error until it reaches a local minima. This is the reason behind calling it backpropagation, since the error propagates backwards. However, this algorithm has proved its capability of giving a good estimation for any linear and nonlinear system.

On the other hand, mostly backpropagation cannot maintain to reach low error values less than local minima, the main reason is because it depends on choosing an initial guess of weights that is able to approach a global minimum. This opened the horizon to find a higher order learning algorithms, such as Levenberg-Marquardt learning algorithm

4. Levenberg-Marquardt Learning Algorithm

The Levenberg-Marquardt (LM) algorithm is one of the most appropriate higher-order adaptive algorithms known for minimizing the mean square error (MSE) of ANN. It is a member of a class of learning algorithms called "pseudo second order methods".

The problem that LM algorithm provides a solution for is called nonlinear least squares minimization as in the following form:

$$f(x) = \frac{1}{2} \sum_{i=1}^{n} r_i^2(x) \quad \text{(A.3)}$$

Standard gradient descent algorithms, such as backpropagation algorithm, use only the local approximation of the slope of the performance surface (error versus weights) to determine the best direction to move the weights in order to lower the error. Second order methods use the Hessian or the matrix of second derivatives (the curvature instead of just the slope) of the performance surface to determine the weight update, while pseudo-second order methods approximate the Hessian. In particular the LM utilizes the so called Gauss-Newton approximation that keeps the Jacobian matrix and discards second order derivatives of the error. If the performance surface is quadratic (which is only true in general for linear systems) then using a second order method can find the exact minimum in one step. In nonlinear systems like ANN, the big issue is that the performance surface may be non-convex, and so quadratic approximations may require several steps for convergence, or more importantly they may diverge. A key advantage of the LM approach is that it defaults to the gradient search when the local curvature of the performance surface deviates from a parabola, which may happen often in neural computing.

TRANSFER FUNCTIONS AND ACTIVATION AXONS

ANN is constructed by interconnecting processing elements (PEs) or neuron. ANN divides the functionality of a neuron into two disjoint operations: a nonlinear instantaneous map, which mimics the neuron’s threshold

characteristics; and a linear map applied across an arbitrary discrete time delay, which mimics the neuron's synaptic interconnections. The Axon family implements common variations on the nonlinear instantaneous maps employed by neural models. Each axon represents a layer, or vector, of PEs. All axons will also be equipped with a summing junction at their input and a splitting node at their output. This allows multiple components to feed an axon, which then processes their accumulated activity. It is important to notice the difference between this sum of activity vectors, and the weighted sum of products depicted by the McCulloch-Pitts neuron model. The latter is implemented as a linear map by the other functional division of the neuron, the Synapse family.

For generality, an axon's map may actually be either linear or nonlinear. However, components in the Axon family typically apply a nonlinear instantaneous map, as given by:

$$y_i(t) = f(x_i(t), w_i) \tag{A.4}$$

Where $y_i(t)$ is the axon's output, $x_i(t)$ is an accumulation of input activity from other components, w_i is an internal weight or coefficient and represents an arbitrary functional map.

All members of the Axon family accumulate input from, and provide output to, an arbitrary number of activation components. In other words, each axon has a summing junction at its input and a splitting node at its output. This functionality is illustrated by the following block diagram:

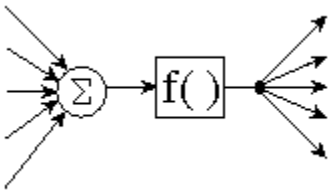

Fig. A.2 The mapping for the PE of the axon class [47]

Axons can receive input from, and provide output to both axons and synapse within the network. There are many types of transfer functions, here six types are introduced: Tanh Axon, Sigmoid Axon, Linear Tanh Axon, Soft Max Axon, Bias Axon, and Axon.

It is important to define first LinearAxon, since all Axons are derived from it; the LinearAxon implements a linear axon with slope and offset control. It is therefore more powerful than the BiasAxon (because it implements an affine transform). The bias is inherited from the BiasAxon and can be adapted, but the slope is controlled by an additional parameter b, which is not adaptive. The activation function is defined as:

$$f(x_i, w_i) = \beta x_i + w_i \tag{A.5}$$

The TanhAxon applies a bias and tanh function to each neuron in the layer. This will squash the range of each neuron in the layer to between -1 and 1. Such nonlinear elements provide a network with the ability to make soft decisions. Its activation function can be defined as:

$$f(x_i, w_i) = tanh\left(x_i^{lin}\right) \tag{A.6}$$

Where $x_i^{lin} = \beta x_i$ is the scaled and offset activity inherited from the LinearAxon.

The SigmoidAxon applies a scaled and biased sigmoid function to each neuron in the layer. The scaling factor and bias are inherited from the LinearAxon. The range of values for each neuron in the layer is between 0 and 1. Such nonlinear elements provide a network with the ability to make soft decisions. The activation function is written as:

$$f(x_i, w_i) = \frac{1}{1+e^{-x_i^{lin}}} \tag{A.7}$$

Where $x_i^{lin} = \beta x_i$ is the scaled and offset activity inherited from the LinearAxon.

The LinearTanhAxon substitutes the intermediate portion of the tanh by a line of slope b, making it a piecewise linear approximation of the tanh. This PE has an input-output map that is discontinuous, so it is not recommended for learning. However, when used with the BackTanhAxon it can learn. This component is more computationally efficient that the TanhAxon (it is much easier to compute the map). The activation function is:

$$f(x_i, w_i) = \begin{cases} -1 & x_i^{lin} < -1 \\ 1 & x_i^{lin} > 1 \\ x_i^{lin} & -1 < x_i^{lin} < 1 \end{cases} \tag{A.8}$$

The SoftMaxAxon is a component used to interpret the output of the neural net as a probability. In order for a set of numbers to constitute a probability density function, their sum must equal one.

Often the output of ANN produces a similarity measure. In order to convert this similarity measure to a probability, the SoftMaxAxon is used at the output of the network. The activation function is:

$$f(x_i, w_i) = \frac{e^{x_i^{lin}}}{\sum_j e^{x_i^{lin}}} \tag{A.9}$$

The BiasAxon simply provides a bias term, which may be adapted. Most nonlinear axons are subclasses of this component in order to inherit this bias characteristic. Its function is:

$$f(x_i, w_i) = x_i + w_i \tag{A.10}$$

Finally, The Axon simply performs an identity map between its input and output activity. The Axon is the first member of the Axon family, and all subsequent members will subclass its functionality. Furthermore, each subclass

will use the above icon with a graph of their activation function superimposed on top. The activation function of Axon is simply written as:

$$f(x_i, w_i) = x_i \tag{A.11}$$

APPENDIX B: ADDITIONAL RESULTS USING ANN

B.1 CC and NMSE Values for Turbulence Statistics as a function of x/H at 0.5 Swirler

Table B.1 U/U_o

x/H	1	2	3	4	5	6
NMSE	0.004296	0.007686	0.006572	0.011189	0.019862	0.027102
CC	0.99802	0.996201	0.997164	0.9952	0.995246	0.995841

Table B.2 V/U_o

x/H	1	2	3	4	5	6
NMSE	0.1754931	0.51269435	0.141166	0.231215	0.200785	0.766467
CC	0.95391044	0.90916944	0.96747	0.958203	0.929208	0.981133

Table B.3 W/U_o

x/H	1	2	3	4	5	6
NMSE	0.03482	0.11202	0.02368	0.0569	0.00803	0.00627
CC	0.9828	0.9843	0.9967	0.9861	0.9961	0.9971

Table B.4 u'/U_o

x/H	1	2	3	4	5	6
NMSE	0.02567	0.03568	0.0271	0.03313	0.09951	0.11424
CC	0.9891	0.9867	0.9904	0.9841	0.9591	0.9573

Table B.5 v'/U_o

x/H	1	2	3	4	5	6
NMSE	0.070478	0.06579	0.102538	0.095666	0.026654782	0.019288
CC	0.966596	0.975929	0.969211	0.98463	0.988616987	0.992505

Table B.6 w'/U_o

x/H	*1*	*2*	*3*	*4*	*5*	*6*
NMSE	0.004296	0.007686	0.006572	0.011189	0.019861678	0.027102
CC	0.99802	0.996201	0.997164	0.9952	0.995245602	0.995841

Table B.7 $u'v'/U_o^2$

x/H	*1*	*2*	*3*	*4*	*5*	*6*
NMSE	0.09821	0.061392	0.064286	0.04683	0.044971901	0.029929
CC	0.967227	0.971464	0.970906	0.977197	0.981558007	0.987104

Table B.8 $u'w'/U_o^2$

x/H	*1*	*2*	*3*	*4*	*5*	*6*
NMSE	0.109756	0.255219	0.404373	0.355753	0.273324449	0.35206
CC	0.94516	0.954969	0.862731	0.914767	0.866744944	0.910396

Table B.9 u'^3/U_o^3

x/H	*1*	*2*	*3*	*4*	*5*	*6*
NMSE	0.09878278	0.12674288	0.128885	0.098384	0.457855	0.374243
CC	0.95511783	0.94066516	0.935332	0.972288	0.92532	0.930494

Table B.10 v'^3/U_o^3

x/H	*1*	*2*	*3*	*4*	*5*	*6*
NMSE	0.69011773	0.50762093	0.493573	0.43802	1.381035	0.789763
CC	0.87401767	0.82006536	0.722365	0.814636	0.84184	0.834668

Table B.11 w'^3/U_o^3

x/H	*1*	*2*	*3*	*4*	*5*	*6*
NMSE	0.152384	0.21810779	0.524761	0.359143	1.10109	0.611617
CC	0.95985242	0.88806586	0.85551	0.818087	0.81588	0.850757

Table B.12 u'^2v'/U_0^3

x/H	*1*	*2*	*3*	*4*	*5*	*6*
NMSE	0.3117435	0.59050525	0.873597	0.872143	0.552619	0.802446
CC	0.85171739	0.71936659	0.459378	0.562007	0.726987	0.714227

Table B.13 $u'v'^2/U_0^3$

x/H	*1*	*2*	*3*	*4*	*5*	*6*
NMSE	0.221342	0.262616	0.282571	0.491515	0.318636	0.202736
CC	0.906873	0.955362	0.945761	0.847325	0.918118	0.930666

Table B.14 u'^2w'/U_0^3

x/H	*1*	*2*	*3*	*4*	*5*	*6*
NMSE	0.5607478	0.74566216	0.767491	1.044913	0.815157	1.819621
CC	0.69096406	0.60246004	0.493369	0.185477	0.456523	0.611352

Table B.15 $u'w'^2/U_0^3$

x/H	*1*	*2*	*3*	*4*	*5*	*6*
NMSE	0.09627057	0.13874659	0.401678	0.235399	0.259724	0.577781
CC	0.97394803	0.95871034	0.937432	0.894443	0.931866	0.816574

VITA

Amin Moh'd AlSharif was born on August 22, 1985, in Amman, Jordan. He was raised in Saudi Arabia. In 1991 he moved with his family to Jordan, where he got his education in local private schools. He graduated from Faisal Military collage holding the second rank in June 2003. In September 2003, he joined the Mechanical program at Jordan University of Science and Technology and graduated in 2008, with a concentration of Mechatronics Engineering, and ranked third among his batch. Later on, Mr. AlSharif joined the work field for a year before he was awarded a scholarship from the American University of Sharjah to continue his master's degree in Mechanical Engineering.